Document No. 81SDR2111

PROCESSING RESEARCH ON CHEMICALLY VAPOR DEPOSITED SILICON NITRIDE– PHASE 3

December 1981

Final Technical Report

1 June 1980 - 31 October 81

Prepared under Contract No. N00014-80-C-0575, NR-032-603

for the

OFFICE OF NAVAL RESEARCH
800 N. Quincy Street
Arlington, Va. 22217

(12) 129

GENERAL ELECTRIC COMPANY
Re-Entry Systems Division
P.O. Box 8555
Philadelphia, Pa. 19101

UNCLASSIFIED

SECURITY CLASSIFICATION OF THIS PAGE (When Data Entered)

REPORT DOCUMENTATION PAGE	READ INSTRUCTIONS BEFORE COMPLETING FORM
1. REPORT NUMBER: 81SDR2111	2. GOVT ACCESSION NO.: AD A109 204
	3. RECIPIENT'S CATALOG NUMBER:
4. TITLE (and Subtitle): PROCESSING RESEARCH ON CHEMICALLY VAPOR DEPOSITED SILICON NITRIDE - PHASE 3	5. TYPE OF REPORT & PERIOD COVERED: Final Report 1 June 1980 - 31 October 1981
	6. PERFORMING ORG. REPORT NUMBER: Doc. No. 81SDR2111
7. AUTHOR(s): R.A. Tanzilli, J.J. Gebhardt, J. D'Andrea	8. CONTRACT OR GRANT NUMBER(s): N00014-80-C-0575
9. PERFORMING ORGANIZATION NAME AND ADDRESS: GENERAL ELECTRIC CO., RSD, P.O. Box 8555, Philadelphia, PA 19101	10. PROGRAM ELEMENT, PROJECT, TASK AREA & WORK UNIT NUMBERS: NR032-603/4-8-80(471)
11. CONTROLLING OFFICE NAME AND ADDRESS: Office of Naval Research, 800 N. Quincy Street, Arlington, VA 22217	12. REPORT DATE: December 1981
	13. NUMBER OF PAGES: 126
14. MONITORING AGENCY NAME & ADDRESS (if different from Controlling Office): Dr. R.C. Pohanka, Office of Naval Research, 800 N. Quincy Street, Arlington, VA 22217	15. SECURITY CLASS. (of this report): Unclassified
	15a. DECLASSIFICATION/DOWNGRADING SCHEDULE

16. DISTRIBUTION STATEMENT (of this Report)

Approved for Public Release; Distribution Unlimited

17. DISTRIBUTION STATEMENT (of the abstract entered in Block 20, if different from Report)

18. SUPPLEMENTARY NOTES

19. KEY WORDS (Continue on reverse side if necessary and identify by block number)

Silicon nitride, chemical vapor deposition (CVD), electromagnetic properties, mechanical properties, chemical properties, microstructure and deposition morphology

20. ABSTRACT (Continue on reverse side if necessary and identify by block number)

The feasibility of preparing free standing plate and hemispherical domes of crystalline silicon nitride by the chemical vapor deposition (CVD) technique has been established as a result of processing research conducted on this program. Physical property characterizations of a wide range of deposits have established the CVD form of silicon nitride as a candidate electromagnetic (EM) window material for advanced, high-performance tactical missile systems. The EM absorption coefficients of CVD silicon nitride in the UV-IR

DD FORM 1 JAN 73 1473 EDITION OF 1 NOV 65 IS OBSOLETE

SECURITY CLASSIFICATION OF THIS PAGE (When Data Entered)

317 MN/m

and radar transmittance passbands are far superior to the more conventional silicon nitride modifications (i.e. HPSN and RSSN). At the current stage of process development, the flexure strength is comparable to RSSN exhibiting similar strength retention properties at elevated temperatures. Average room temperature flexure strength levels of ~~.617 MNm^{-2}~~ (46,000 psi) were achieved by codeposition with minor amounts of ~~AlCl$_3$~~ aluminum chloride during this program (Phase 3); this level represents a 150 percent increase in strength compared to levels achieved during the initial Phase 1 program.

With a better understood deposition model now in hand, as a result of the Phase 3 program, a high probability exists in future process optimization studies for achieving additional improvements in the mechanical and optical properties of CVD ~~α-Si$_3$N$_4$~~ alpha-silicon nitride.

FOREWORD

This exploratory development program (consisting of three phases) was sponsored by the Office of Naval Research (ONR) under the following contracts:

PHASE	CONTRACT NO.	PERIOD OF PERFORMANCE	REPORT NO.	ISSUE DATE
1	N00014-76-C-0547	1 Apr '76 - 31 Aug '77	77SDR2257	Sept '77
2	N00014-78-C-0107	1 Feb '78 - 1 Oct '79	79SDR2324	Dec '79
3	N00014-80-C-0575	1 Jun '80 - 31 Oct '81	81SDR2111	Dec '81

This final report, in addition to documenting processing research under Phase 3, summarizes previous work under earlier phases. This research program was administered originally under the direction of Dr. A.M. Diness and subsequently under the direction of Dr. R.C. Pohanka of the Office of Naval Research.

The authors also acknowledge the experimental support of the following members of the technical staff of the General Electric Co.:

CVD Process Development	R. Pridgen J. Hanson R. Garrison
Specimen Preparation	W. Staley H. Reiss
XRD Analysis	Dr. E. Feingold
Optical Properties	K. Bleiler
Mechanical Properties	F. Rouse

TABLE OF CONTENTS

LIST OF TABLES

LIST OF ILLUSTRATIONS

LIST OF ILLUSTRATIONS (Continued)

SECTION 1.0
INTRODUCTION AND SUMMARY

SECTION 1.0

INTRODUCTION AND SUMMARY

The feasibility of preparing free standing plate and hemispherical domes of silicon nitride by the chemical vapor deposition (CVD) technique has been established as a result of processing research conducted on this program. During the course of this research a deposition model has evolved which explains many of the unusual deposition phenomena associated with the synthesis of CVD silicon nitride. Physical property characterizations of a wide range of deposits have established the CVD form of silicon nitride as a candidate electromagnetic window material for advanced, high-performance tactical missile systems. Over the range of conditions studied, crystalline deposits are always of the alpha form (i.e., CVD α-Si_3N_4) and exhibit two major transmittance pass bands in the electromagnetic spectrum: the ultraviolet-infrared band and the radar-RF wavelength band. The absorption coefficients of CVD α-Si_3N_4 in these pass bands are far superior to the more conventional silicon nitride modifications, viz., hot pressed silicon nitride (HPSN) and reaction sintered silicon nitride (RSSN). These superior electro-optical properties are not unexpected since the CVD deposits (when not intentionally doped) represent the highest purity of silicon nitride synthesized to date in monolithic form.

At the current state of process development (which is by no means final), the strength of CVD α-Si_3N_4 has been found to be comparable to RSSN exhibiting similar strength retention properties at elevated temperatures. Fractographic analyses when coupled with the brittle fracture theory of Griffith have identified extrinsic flaw morphologies which are responsible for the current strength plateau associated with CVD α-Si_3N_4. It is this area of processing research which was emphasized in the Phase 3 program culminating in the evolution of a better understood deposition model for CVD α-Si_3N_4. This model will provide guidelines for conducting future process and property optimization studies.

The remainder of this report is concerned with the results of the Phase 3 program. Also included in this report (Section 4.0) is an overview of the total program (including the results of two previous programs) and recommendations for continued research and development.

SECTION 2.0
PROCESSING RESEARCH

SECTION 2.0

PROCESSING RESEARCH

2.1 EXPERIMENTAL PLAN

Process studies were continued based on results obtained in Phase 2 (Ref 1), centering around conditions which had yielded the highest strength material, viz., 1475°C, Si/N ratio of about 0.66 and total feed rate of 1 liter/min. at 5.3 KPa (40 torr). The overall goal was to increase strength levels above the maximum MOR achieved in Phase 2 (297 MPa) by improving the grain structure of the deposits, either by achieving a finer columnar habit, or preferably by developing methods for eliminating the columnar growth entirely in favor of a fine, orthotropic grain structure.

For practical reasons, however, strength improvement was not to be attained at the expense of other critical properties such as optical and electromagnetic characteristics, or by techniques which could not readily be transferred into the equipment suitable for practical device fabrication. Thus introduction of charged carrier species or high levels of excess silicon were to be avoided.

A principal difficulty with the columnar growth habit (not unusual for CVD processes) is the network of microcracks that is formed by intersecting and adjoining crystallites. With thicker deposits, increasing column breadth (greater cone angle) toward the last deposited surface results in more severe crack-generating and propagating paths. Consequently, after establishing baseline conditions and investigating the relative effects of hydrogen and nitrogen as carriers, the experimental plan focused on the use of additives to influence both gas phase chemistry and nucleation and growth phenomena. These studies were performed using a cold wall reactor and selected processes were transferred to a one inch hot wall resistance-furnace reactor as a first scaling step.

A number of additives were considered as likely prospects at the end of Phase 2 of this program. Certain of these were investigated during Phase 3 process studies in the deposition systems appropriate to their physical properties. These included the following:

(a) Two carbon sources were used - propane (C_3H_8) and carbon tetrachloride. Earlier report (Refs. 2, 3), had indicated that microstructural alterations in the form of finer, almost needle-like columnar structures, had resulted from inclusion of significant amounts of propane relative to silicon

tetrachloride content. Carbon tetrachloride was also used as a carbon source, free of the polymeric chain and intermediate gas phase reactions typical of hydrocarbons, such as propane. Evidence of formation of free silicon in a number of earlier cold wall deposits led to its inclusion as a method of forming silicon carbide to reduce free silicon content.

(b) Boron and aluminum were selected as two single-valence elements with small atomic radii which form stable nitrides and which could be included in the silicon nitride deposits as solid solutions (i.e. substitutionally, or interstitially). An indication of structrual modification has been reported as having occurred in the case of aluminum (Ref. 3).

(c) Hydrogen sulfide was used in an effort to form transiently stable (at deposit temperature) SiS_2 and SiS species to reduce formation of excess free silicon (Ref. 4).

(d) Methyltrichlorosilane (CH_3SiCl_3) was chosen to introduce silicon carbide predeposition polymers in the gas phase as well as to provide a carbon source for possible formation of a disperse SiC phase (Ref. 5).

(e) Nitrous oxide (N_2O), used in concurrent programs, has been found to produce mixed amorphous and crystalline deposits in appropriate amounts for applications specific to those programs. It was used in this program to a limited extent to evaluate the relationship between the mechanical and electromagnetic properties of such materials.

(f) Both hydrogen and nitrogen have been used as carriers in the past. They were compared under similar circumstances in both cold wall and hot wall depositions, to examine the possible influence of silicon tetrachloride reduction occurring simultaneously with the ammonia complex formation and decomposition normally associated with silicon nitride deposition.

In addition to these process studies, fabrication of larger area, thicker material for characterization as well as deposition of contoured specimens representative of practical hardware were carried out using a four-inch diameter, resistance-heated hot wall furnace.

2.2 EXPERIMENTAL PROCEDURES

The furnace systems used are described in Reference 1 and are shown in Figures 2-1 and 2-2 while Figure 2-3 illustrates hot wall deposition geometries which have been developed over several years effort on this and other programs.

Graphite served as the deposition surface in most instances; the grade selected depending on the geometry or the purpose of the deposition experiment. Union Carbide Grades ATJ and CS as well as Grafoil® and Great Lakes Grade HLM have been used for various substreates.

Modifications were made to the gas feed lines of both cold and hot wall systems to enable inclusion of additives by vaporization or entrainment as appropriate, or by direct addition through a volumetric flowmeter where possible. Prior to each run, the systems were evacuated and closed off from the vacuum pump for 30-60 minutes as a crude leak test inasmuch as prior work had shown that oxygen (from air and moisture) has a profound effect on the structure and color of the deposits. Any detectable movement of the mercury level in the control manometer during that period was considered to be indicative of a leak sufficiently large to warrant its repair prior to proceeding with the experiment.

Deposits obtained in cold wall (CW-3) runs were sliced into small flexure bars (19.1x3.2xt(mm) where t = thickness) if they appeared to be of suitable quality. One such bar was taken from each side of the centerline of the substrate beneath the gas inlet nozzle. The graphite substrate was then burned away in a muffle furnace at 975-1000 K. The hot wall furnace (HW-1) yielded somewhat more material which was freed from the Grafoil® substrate prior to selecting and cutting specimens for test.

The four-inch diameter hot wall furnace (HW-4), designed along the same lines as HW-1, was used for deposition of thicker material of larger area and for formation of a number of dome-shaped contoured specimens. The latter were deposited in a graphite female mandrel mounted perpendicular to the gas flow. Plate material was deposited on graphite substrates mounted parallel as well as perpendicular to the gas flow.

Three point flexure testing was the primary method of gaging changes in strength resulting from modifications in CVD process parameters. Conservative estimates of flexure strength were obtained by having the unground[(1)] last deposited surface[(2)] under tensile loading during testing.

---

(1) Because of the likelihood of specimen loss during grinding (due to the limited specimen areas and thicknesses available), it was decided to test specimens in the as-deposited condition.

(2) Previous measurements during Phase 2 (Ref. 1) had shown that a strength gradient exists in CVD $-Si_3N_4$ with strength decreasing with distance from the first depcsited surface.

2.3 EXPERIMENTAL RESULTS

2.3.1 Cold Wall Reactor (CW)

Experimental conditions and results of cold wall reactor experiments are tabulated in Tables 2-1 and 2-2. Figure 2-4 shows the general appearance of last deposited surfaces after typical 30 minute runs without additives. Appendix A contains scanning electron microscope (SEM) photomicrographs of last deposited and fracture surfaces of numerous cold wall reactor specimens selected for flexure strength determination.

Under the conditions used, all deposits were columnar crystalline and faceted, particularly in the central region beneath the gas inlet line. The first series of deposits (1-32) was made to study the effects of a) hydrogen versus nitrogen as a carrier, and b) high versus low silicon to nitrogen ratios (typically 3.3 and 0.66 respectively). Some variations in temperature and pressure were also made to study kinetic effects. In addition to the general observations regarding the crystalline columnar nature of the materials, the following more specific points can be made:

a) Si/N Ratio, H_2 Carrier: These deposits showed high concentrations of shiny blocky, irregular crystals, voids and overgrowths. Formation of globules of silicon metal was observed on the crystalline surfaces in some instances, and in other cases of a blue surface shadow which became gray on exposure to air. Lower densities may be the result of closed trapped voids between adjacent columns, and/or excess silicon (ρ_{Si} = 2.33 g/cm^3, ρSi_3N_4=3.19 gm/cm^3). Varying temperature between 1650 K and 1750 K did not produce a noticeable variation in mass deposition rate suggesting that under these conditions the rate was mass flow limited. These results are listed in Table 2-3.

Deposits on the back face of the substrate tended to be dark, showing globules of silicon. The amount of white cracked and presumably amorphous silicon nitride around the periphery of the central region was less than it was when nitrogen was used as a carrier.

b) Si/N Ratio, N_2 Carrier: With nitrogen as a carrier, the deposits were considerably more uniform, although still faceted and columnar. The periphery of the deposits was nearly always amorphous with a cracked "bubble raft" appearance typical of such deposits. Backface deposits tended to be lighter in color, more crystalline and homogeneous than when hydrogen was used as the carrier. Formation

of elemental silicon was not noted to occur as a separate phase. Variation of temperature led to a noticeable correlation of mass deposition rate with temperature as is also shown in Table 2-3. The increase in rate with temperature was greater at higher ammonia concentrations.

Table 2-4 lists flexure strengths of a number of these deposits together with deposition conditions. The trend indicates clearly that the use of a nitrogen carrier at lower Si/N ratios produced the strongest material.

Achievement of uniform fine grain structures using the cold wall reactor, at rates reasonable with respect to obtaining thick deposits, is very sensitive to gas flow patterns when deposition occurs via boundary layer diffusion. For example, most of the deposits displayed a significant variation in structure at the edges of the substrate, as shown in Figure 2-5. This is evidently due to boundary layer separation and establishment of fluctuations below the separation line. Material deposited above the separation line was usually crystalline and columnar, while below the line, discontinuous laminar structures prevail. Figure 2-5 illustrates this shift in structure. While the surface appearance of the deposit suggests that it could be a continuously nucleated, fine grain material similar to what can be formed in CVD silicon carbide, pyrolytic graphite and other systems; in actuality it is a series of discontinuous columnar layers, separated by lower density, possibly amorphous layers. Both the upper and lower regions of the edge deposits are, in general, crystalline, judging from the infrared reflectance spectrum obtained from the two types of deposit. Such discontinuous flow conditions are probably part of the explanation of banded and layered structures frequently encountered in deposition of silicon nitride from $SiCl_4$-NH_3 mixtures.

c) Additives: The design of the cold wall feed system permitted introduction of additives from gas and liquid containers only. Consequently additive studies were limited to propane, carbon tetrachloride and boron trichloride. The deposition conditions and results of these depositions are summarized in Table 2-2.

2.3.2 Hot Wall Furnace Run (HW-1)

Basic deposition conditions selected for hot wall reactor studies were essentially those which gave maximum strength in cold wall studies, i.e., temperature ~ 1750K, Si/N ~ 0.66. Pressure, however, was reduced to the minimum value achievable after observing that grain size was smaller and more uniform and deposition thickness more uniform.

Table 2-5 summarizes the deposition conditions and results, of these experiments. Appendix B contains SEM photomicrographs of last deposited and fracture surface morphologies on specimens from selected experiments listed in Table 2-5. Table 2-6 provides detailed flexure strength data on selected depositions.

Somewhat surprisingly, higher strengths and a finer grain structure were obtained with a hydrogen carrier than with nitrogen, (Runs 12 versus 15) in contrast to cold wall results. This is probably related to boundary layer concentrations of silicon, intermediate composition and rates of deammination or nitriding. Thus, results of the series of runs made with the N_2 carrier listed in Table 2-5 may have beer significantly altered with hydrogen as a carrier, particularly with additives such as methylchlorosilane as will be discussed later.

Addition of boron trichloride in small amounts (Run 8) caused formation of a light blue translucent deposit which contained at least one delamination, possibly due to flow fluctuation. Its surface crystal habit was somewhat distinctive compared to most of the deposits (Fig. B-1). The x-ray diffraction pattern showed a shifting of Si_3N_4 lines indicating some solubility, while emission spectrographic analysis showed a boron content of 0.25 w/o.

Addition of a larger quantity of boron trichloride (Run 6) led to formation of clear transparent boron nitride as determined from its infrared spectrum, with no silicon nitride evident. Still larger quantities (Run 9) produced a broken, amorphous structure not suitable for characterization.

Evidently more than a small amount of boron trichloride tends to favor development of a borazine or chloroborozole intermediate chemistry, either reversing silyl complex formation or preventing it. A similar indication was seen in cold wall runs, where feeding a mixture of BCl_3 and $SiCl_4$ vapor caused clogging of the feed line with a white powdery deposit that did not occur in the absence of BCl_3.

Addition of aluminum chloride also produced some changes in structure as well as the highest strength value (Rune 18 U). The fracture and upper surface of this specimen are shown in Figure B-12 while Figure B-13 shows the elemental aluminum scan. Aluminum content was estimated by emission spectroscopy to be 0.2 w/o. As with Runs 17 and 19, the lower position of the deposit, i.e. near the gas inlet showed a much higher aluminum content (approx. 0.7-1.2 w/o) as well as a significantly modified structure (Figure B-10). Here there appears to be a severe structural incompatibility, with breaking up of the customary columnar silicon

nitride form. Strength levels were lower as would be anticipated. Figure B-11 shows a corresponding elemental Al scan of the fracture surface for this portion of the deposit.

2.3.3 Hot Wall Furnace (HW-4)

Conditions used in fabricating larger area, thicker and contoured silicon nitride using the four inch diameter furnace (HW-4) are listed in Table 2-7. In all of these runs silicon tetrafluoride was used instead of the chloride. In the flat plate experiments (exclusive of Runs 391 thru 394) oxygen was added as a dopant to explore its role in altering deposition kinetics as well as its effect on flexure strength. Table 2-8 summarizes the flexure strength measurements on these deposits. Appendix C contains SEM photomicrographs of last deposited and fracture surface morphologies for selected specimens from each dopant run listed in Table 2-7.

For flow conditions normal to the deposit (Runs 328 versus 329), doubling the flow rate resulted in a finer grained material (LDS) but with comparable strength since specimens were tested with the first deposited surface (FDS) in tension. For flow conditions parallel to the deposit (Runs 378, 379, 382, 383), a wide range of strengths were observed for basically identical flow conditions. These variations reflect a grain-size gradient along the lengths of respective plates. Strengths increased with decreasing grain size of the LDS and a transition grain size of about 40 microns was observed between fracture modes with the lower strength material exhibiting an intergranular fracture mode as one would expect.

Dome shaped deposits were obtained on contoured female graphite mandrels suspended perpendicular to the gas flow, and were freed from the graphite by combustion. Thickness limitations were experienced mainly due to the build up of reaction by-products (principally ammonium fluosilicate - $(NH_4)_2\ SiF_6$) in the furnace exhaust lines. Figure 2-6 shows the post-deposition condition of one of four domes fabricated on this program. After sectioning and removal of the graphite mandrel by oxidation, the domes were lapped and polished at Penn Optics Inc. (Reading, Pa.) using diamond tooling exclusively. Figure 2-7 shows the as-finished condition of a dome after lapping and polishing.

2.4 PROCESS STUDY DISCUSSION

2.4.1 Chemical Aspects of Deposition Kinetics

A number of studies have been published about the chemical vapor deposition of silicon nitride by the reaction silicon halides and ammonia (Refs. 1 and 6 through 10). The chemistry involved has not been explored in detail but in the case of $SiCl_4$, reaction mechanisms similar to those presented by Billy (Ref. 11) and Glemser and Naumann (Ref. 12), have been assumed to occur. For example, formation of intermediates and polymers such as the following has been identified as occurring on reaction and pyrolysis of $SiCl_4$ and NH_3:

$$6\left[Si(NH)_2\right]_x \xrightarrow[-2NH_3]{400^oC} 2\left[Si_3(NH)_3N_2\right]_x \xrightarrow[-NH_3]{650^oC} 3\left[Si_2(NH)N_2\right]_x \xrightarrow[-NH_3]{1250^oC} 2\alpha\, Si_3N_4.$$

Formation of high polymers consisting of non-periodic and unsymmetrical networks of $Si(NH)_4$ and SiN_4 tetrahedra are also postulated as part of the mechanism. The results have shown that α-Si_3N_4 is formed exclusively, in crystalline form above about 1300-1350°C and in so-called 'amorphous' form below that temperature range. The crystalline deposits tend to be columnar with faceted surfaces and various crystal axes oriented preferentially to the substrate. The amorphous deposits tend to be more laminar and of lower density. Color has been associated with oxygen content and lattice parameter, with high oxygen levels (ca. 1-2 w/o) being typical of white amorphous deposits and lower oxygen contents characteristic of dark brown (ca.0.3 w/o) and green (0.5 w/o) crystalline deposits. The c direction lattice parameter decreases as oxygen content increases (Refs. 1, 6 and 7). The lowest oxygen content reported (0.05 w/o) (Ref. 13), appears to rule out the necessity of oxygen contents around 1.0 w/o to stabilize the alpha form as postulated by Wild, et. al. who described α-Si_3N_4 as an oxynitride with the molecular formula $Si_{11}N_{15}O_{0.3}$ (Ref. 14).

During the course of the present program as well as in concurrent programs in this laboratory, the chemical vapor deposition of silicon nitride has been carried out under a variety of conditions, with little significant deviation from the general results summarized above except with certain additives. Experimental variations have included:

a. Hot wall (graphite) and cold wall (steel) furnaces with different reaction volumes,

b. Hydrogen vs nitrogen carriers,

c. SiF_4 vs $SiCl_4$ as well as $SiHCl_3$, SiH_2Cl_2 and SiH_4 precursors,

d. High (3.3) to low (0.66) Si/NH_3 ratios,

e. Parametric variations (temperature, pressure, flow rate, dilution, substrate effect), and

f. Use of reactive additives (CCl_4, propane, BCl_3, $AlCl_3$, H_2S and CH_3SiCl_3 and N_2O).

It must also be assumed that a certain background of oxygen contamination, as O_2, H_2O or CO_2, was present as a result of leaks in the gas feed lines, gaskets, absorbed moisture and complexes, etc. Wild, et al (Ref. 14) estimate that oxygen potentials lower than about 10^{-24} atm. are necessary to avoid formation of α-Si_3N_4 or Si_2ON_2 in preference to β-Si_3N_4. Most practical systems do not meet this requirement. The background in these studies was probably higher in the cold wall system than in hot wall furnaces although no measurements were made of oxygen content per se. In hot wall experiments, reproducible results were obtained only with a low and constant leak rate, determined by experiment to mean a pressure rise of less than about 0.5 torr in one hour in the static, evacuated furnace and associated feed lines.

Aspects of the deposition process and the product obtained can be explained by such factors as:

a. The difference in reactivity of SiF_4 versus $SiCl_4$ toward NH_3 and H_2O as well as H_2,

b. The strength of Si-O bonds vs. Si-N bonds (184 versus 105 kcal/mol) (Table 2-9),

c. The possible formation of polymeric silazanes, analogous to polycarbosilanes, containing some level of Si-O bonding,

d. The high surface energy of α-Si_3N_4 crystal surfaces and consequent low atomic mobility (Ref. 15).

e. Kinetic and temperature factors involved in the formation and decomposition of intermediate species, as well as the effects of oxygen content on these factors.

Deposits made with SiF_4 were generally more uniform and free of nodules and gas flow effects than those made with $SiCl_4$. This is due to the higher Si-F bond strength which makes it less susceptible to hydrolysis as well as more stable toward formation of amine complexes, and reduction by hydrogen. For example SiF_4 forms only one adduct, $SiF_4.2NH_3$ which dissociates at relatively low

temperature (Ref. 16) instead of splitting off HCl and forming more complex polymers such as Billy had described (Ref. 17). Solid by-products of deposits made from SiF_4 and NH_3 consisted almost entirely of ammonium fluosilicate, $(NH_4)_2\ SiF_6$. Formation of free silicon occurs more readily from $SiCl_4$ (as well as from SiH_4, $SiHCl_3$ and SiH_2Cl_2). This greater reactivity of $SiCl_4$ led to frequent nodular overgrowths and banded structures (mixed amorphous and crystalline) as a result of rapid polymer growth. At high oxygen levels, i.e. in cold wall experiments, a glassy polymeric deposit was obtained on an unheated substrate (Ref. 1) with $SiCl_4$ and NH_3 while white spherical byproduct deposits were observed to form on the electrodes during high temperature depositions. At relatively high temperature (1475°C) and low nitrogen pressure (1 torr), the $SiCl_4$-NH_3 deposition byproducts tended to yield free silicon and gaseous products in both cold wall and hot wall experiments. Nevertheless, in the presence of moisture and/or air contamination, amorphous Si_3N_4 was formed from the SiF_4-NH_3 system as well as from $SiCl_4$-NH_3 reactants, although to a lesser extent owing to greater stability of the adduct toward hydrolysis (Refs. 18-20).

In view of the ease of replacing a chlorine atom with oxygen on $SiCl_4$, as well as forming Si-O bonds with free silicon, the probability is high that the Si-O intermediate complex molecules would contain oxygen atoms to a varying degree depending on composition of the gas phase and temperature. Such intermediates particularly at high ammonia levels, could constitute the deposition species in a mechanism similar to the liquid drop mechanism postulated by Koizlik et. al. (Ref 21) for the deposition of pyrolytic carbon. Such mechanisms may also operate, under appropriate circumstances, in the case of deposition of boron nitride and silicon carbide in which high molecular weight species can be formed thermally (Refs. 22, 23). At relatively high oxygen contents, the Si-O-N intermediates can react further with ammonia to form α -Si_3N_4(Ref. 24) possibly with release of Si-O which could remain in the unreacted region of the surface layer, perpetuating the Si-O-N sequence even in the absence of additionaly oxygen from the gas phase. At lower temperatures, ca. 1300°C, sufficient thermal energy would not be available to complete a sluggish reaction and permit surface diffusion to occur rapidly enough to allow crystal formation. With a sufficiently low O content in the polymer and more thermal energy, α -Si_3N_4 containing some residual bonded oxygen results. It has been observed in concurrent experiments in this laboratory that crystallization of α -Si_3N_4 can be prevented up to 1475°C by addition of excess oxygen.

The growth of bulky, elongated crystals by a probable liquid drop mechanism was observed to be frequent in the cold wall reactor experiments at high Si-N ratios and with a hydrogen carrier. This is shown in Figure 2-8, where the elongated crystals had evidently grown out of the hot-zone and the droplets solidified. Initiation of crystallite formation from other droplets can be seen, as well as droplet formation on the sides of crystals. This would account for some of the complex overgrowths, interpenetrating crystals and voids seen in deposits made at high deposition rates even with a relatively low oxygen background. The high wetting angle combined with high crystallite surface energy, suggests that continued reaction and growth may be restricted to the surface beneath the droplet, explaining the columnar habit (Ref. 25). It also tends to support the existence of some degree of oxygen content since pure liquid silicon would be expected to wet silicon nitride (Ref. 26) and thus lead to a more integral, less columnar growth and perhaps formation of β -Si_3N_4(Ref. 4). In hot wall experiments, the finest grain structures and highest strengths were obtained at high flow rates and with low oxygen background, i.e. using a hydrogen carrier. This suggests a low oxygen content in the droplet, small droplet size or perhaps a thin film and a somewhat lower growth rate. The columnar nature persisted however (Figure 2-9).

With a nitrogen carrier, the liquid droplet phenomenon was not observed as in the cold wall reactor, suggesting that the reduction of silicon by hydrogen plays an important part in drop formation even in the short times provided by the cold wall reactor, whereas in hot wall deposition, longer residence time enables gas phase reaction sequences to occur to a greater extent, leading to a more homogeneous nucleation mixture in the boundary layer. Cold wall reactor deposits made with a nitrogen carrier invariably displayed a white ring of amorphous material (Figure 2-4) and more laminar banding, than when hydrogen was used. This suggests that the high level of silicon activity obtained with a hydrogen carrier contributes to formation of polymers with a lower oxygen content (i.e., low O/Si ratio) that form crystalline α -Si_3N_4 more rapidly and at lower temperatures.

Except for amorphous deposits at the cooler inlet and exit ends of the furnace, little evidence remained of liquid intermediates in hot wall experiments. Exceptions were noted for example when oxygen was added to a SiF_4-NH_3 feed mixture as N_2O where lace-like structures remained at crystal surfaces as shown in Figure C-6. Other examples were observed when the furnace was less vacuum tight.

The hot wall reaction environment, with lower mass flow rates per unit volume of reaction zone, offers a more stable environment for control of intermediate species formation. There, deposition of intermediates may occur as thin film formation within or under which crystal growth occurs by epitaxial mechanisms with migration at the interface to sites of lower potential energy.

2.4.2 Hypothesized Deposition Mechanism

2.4.2.1 Chemical Model

Using the above speculation, based partly on observations made during this and other programs, a deposition mechanism can be hypothesized to explain many of the phenomena noted in the vapor deposition of silicon nitride including:

a. The amorphous - crystalline phase boundary and its movement to higher and lower temperatures with respect to deposition parameters

b. The lower deposition rates and more uniform structures obtained with SiF_4

c. The occasional appearance of β-Si_3N_4 when unstable precursors such as SiH_2Cl_2 are used (Ref. 5) or when oxygen levels are low enough to permit free silicon to form and be nitrided directly

d. The invariant columnar grain structure, intergrown crystallites and voids noted in most deposits

e. The presence of oxygen in α-Si_3N_4

f. The inability of most additives to alter the structure and properties of the deposits, at least within the narrow limits explored in this program.

It depends not only on the formation of reactive polymeric intermediate species from the controlled feed gases, but also on the inclusion of oxygen as Si-O and possibly excess silicon. The composition of the intermediates, which may vary within a given deposition area, determines their physical and chemical properties, their rates of deposition as droplets or thin, adsorbed films as well as rates of solidification or crystallization through continued reaction with the gas phase components (ammonia, nitrogen, hydrogen, silicon, reactive intermediates, hydrogen halides, etc). Oxygen released by such reactions at the deposition surface can continue to be within collision distance to react with incoming species and perpetuate the sequence or alter it in the direction of higher oxygen content to form bands of amorphous material in crystalline deposits. Gas dynamic effects can also perturb the boundary layer composition and the nature of the deposit at edges, corners and where boundary layer separation occurs. Thermal, kinetic,

compositional and gas dynamic factors thus goven whether the deposit is crystalline, amorphous or mixed, and whether it will contain much or little oxygen. The presence of oxygen in the deposit prevents or delays transformation to the β phase at deposition temperature.

Formation of continuous crystalline layers of silicon nitride of small grain size and non-columnar habit is prevented by surface tension forces characteristic of the crystalline and intermediate species at the growth surface, which prevent wetting and spreading. Morphological details of the model are described below.

2.4.2.2 Topological Model

The deposition morphologies observed for CVD silicon nitride microstructures are consistent with the thermodynamic criterion which constrain processes to proceed in a manner such that minimum energy configurations develop during and after equilibration. Some microstructural features observed during deposition (and subsequently after fracture of flexure specimens) which are manifestations of this criterion include:

a. A columnar grain structure with a high degree of preferred orientation

b. Surface nucleation with subsequent mutually restrained lateral growth

c. Faceted last deposited surface topography indicative of a growth mechanism where the fastest growing orientation tends to grow itself out leaving the crystal with its more slowly growing surfaces

d. Near epitaxial growth conditions where the grain boundaries between neighboring columnar grains exhibit a high degree of coherency

e. Cleavage fracture morphologies indicative of transgranular fracture modes except in a few instances where dopants such as a critical amount of oxygen promote intergranular fracture morphologies

f. Alteration of the columnar growth habit when certain additives such as aluminum and boron tend to promote some degree of continuous nucleation

g. Development of a faceted, soap-bubble surface morphology when a featureless precursor fragment deposits, followed by in-situ surface crystallization to further minimize surface energy.

Examples of these morphologies are contained in the following illustrations provided by scanning electron microscope (SEM) investigation of last deposited surfaces (LDS) and fracture surfaces of pertinent deposits.

Figure 2-9 illustrates a typical "hot wall" last-deposited surface (LDS) morphology and associated fracture surface. Columnar growth with mutually restrained lateral growth is illustrated by the fractograph which also shows a transgranular fracture mode. It is instructive in this instance to express analytically the energy balance associated with brittle fracture as follows (Ref. 27):

$$2\Gamma = 2\gamma_s - \gamma_{gb} \qquad (2\text{-}1)$$

where Γ is the fracture energy

γ_s is the surface energy for single crystal cleavage

γ_{gb} is the interfacial grain boundary energy

Relatively low interfacial grain boundary energy must be associated with the typical columnar growth habit shown in Figure 2-9 since transgranular fracture generally occurs. Thus, these lateral boundaries are similar to low angle grain boundaries with a high degree of coherency preventing intergranular fracture paths from occurring (i.e. γ_{gb} approaches zero). In only one instance has intergranular fracture been observed. This has occurred when a critical amount of oxygen dopant is introduced during deposition. Figure 2-10 illustrates one such intergranular fracture morphology. In this instance, the grain boundary interface energy is now a factor resulting in a reduced brittle fracture energy (Γ) below that associated with single crystal cleavage (γ_s). In general, for a wide range of deposits studied on this program, transgranular fracture associated with the columnar growth habit exhibits higher flexure strengths than comparable intergranular fracture morphologies associated with a critical degree of oxygen doping.

Examples of how a fastest growing orientation tends to grow itself out leaving the LDS crystal surface with its more slowly growing surfaces are shown in Figure 2-11. It is implied that this cycle must repeat itself in time and that a varying growth rate is associated with this growth habit.

It was only in the case of boron and aluminum doping that growth habits were significantly altered from the typical columnar growth habit previously described.

Figure 2-12 is a fractograph of an aluminum doped deposit showing evidence of a continuously nucleated growth habit. Another example of the possible initiation of a non-columnar growth habit occurred with boron doping where, as shown in Figure 2-13, lateral growth was initiated in the last deposited surface.

Additional evidence for the criterion of minimization of surface energy is shown in Figure 2-14 where an initially hemispherical LDS grain morphology develops crystalline facets in its quest to lower surface energy. This is not unlike the phenomenon of thermal faceting where planar surfaces develop facets when exposed to elevated temperature conditions because of the requirement to minimize surface energy (Ref. 28). In this instance the faceted surface consists of a set of low-index planes and a set of planes of a more complex orientation making a contact angle θ with the low index planes.

2.4.2.3 Effect of Additives

The use of additives to alter the growth structure of CVD materials has been demonstrated in the case of tungsten where mechanical disruption of the nascent surface (Ref. 29) or codeposition of a second phase (Refs. 30, 31) were found to change the usual columnar growth habit significantly. In the experiments performed in this program, efforts to modify the structure were successful with the addition of BCl_3 and $AlCl_3$. In the case of BCl_3, a critical level determined whether an amorphous Si-doped BN structure formed (HW-6) or whether a B-doped crystalline Si_3N_4 was synthesized (HW-8). In the former case, the formation of BCl_3-NH_3 intermediates was evidently rapid enough or extensive enough to eliminate formation of Si_3N_4 complexes even at relatively moderate levels of addition. With $AlCl_3$, evidently a different growth mechanism was established which altered the usual columnar growth habit, as shown in Figure 2-12. The mechanism is not evident but $AlCl_3$-NH_3 polymers (Refs. 32, 33, 34) of sufficient stability may be able to be formed, possibly in a manner analogous to the Si-O-N system to modify the growth habit. As with $SiF_4.2NH_3$, $AlC_3.NH_3$ dissociates (Ref. 34), but maybe stabilized as an Al-O-N complex polymer.

Other additives did not produce changes in structure under the conditions explored which, while not extensive, provided opportunity for effecting changes in the V-L-S mechanism at some point. The stability of the Si-O bond however remained the dominant factor in preserving the growth habit except in the case of aluminum addition, in which case similarity in chemistry and stability allowed some

interaction. Additives such as propane may influence the growth habit by competing with the Si-N intermediates for oxygen through formation of strong C-O bonds. This would tend to limit their size and molecular weight and could lead to a finer grain deposit with narrower cone angles, i.e., almost needle-like, as has been described (Ref. 2). This mechanism may also explain the achievement of fine grain, almost vitreous deposits of β -SiC under certain stoichiometric conditions (Ref. 35). Inasmuch as relatively high molecular weight silazanes have been identified (Ref. 36), deposition from these species in the total absence of oxygen may yield a fine grain material, and might also resolve the question regarding the stability of oxygen-free α -Si_3N_4.

2.4.3 Summary

Formation of columnar, crystalline α -Si_3N_4 by chemical vapor deposition is influenced by the incorporation of residual, low-level oxygen contamination into polymeric intermediate species that decompose or react further to form α -Si_3N_4. The presence of oxygen contributes to continuous columnar growth and inhibits formation of β -Si_3N_4. To modify growth structure, additives must compete successfully with Si for all of the oxygen present, or be incorporated into the intermediate species so as to reduce surface forces at the growth surface.

Future studies may fruitfully investigate the use of additives such as methyl and methylene chloride (to yield active carbon and remove oxygen as CO) as well as expand on the use of aluminum-containing precursors such as trimethyl aluminum. In all cases, the oxygen background of the deposition system should be constant and controlled, and preferably, known more precisely than is the case now with most systems.

The mechanisms suggested for formation of CVD Si_3N_4 may also apply to certain conditions prevailing during the nitriding of silicon where mixtures of α and β phases are obtained in varying ratios. It does not however, resolve the question of the necessity for the presence of oxygen in the lattice to stabilize the α phase (Ref. 14).

TABLE 2-1. SUMMARY OF COLD WALL REACTOR EXPERIMENTS FOR THE $SiCl_4$-H_2-N_2-NH_3 SYSTEM

RUN CW-3	T K	P KPa	FEED RATES cc/min. $SiCl_4$	NH_3	CARRIER	Si/NH_3	RATE mg/min	DENS. g/cm^3	MOR MN/m^2	MOR KSi
1	1750	5.3	230	68	H_2 700	3.3	48.8	3.09	86.5	12.54
								2.97	55.2	8.00
2	1750						52.0			
5	1700						50.7		74.8	10.85
									45.6	6.6
6	1650						34.1			
7	1750				N_2 700		46.2			
8	1800						52.2			
9	1650						30.3			
10	1650						25.4			
11	1650						26.3			
12	1750						15.7			
13	1750						60.4	3.17	66.1	7.59
								3.15	41.4	6.00
14	1650						30.8			
15	1750		216	128	H_2 656	1.7	66.1			
17	1750		177	267	H_2 540	0.66	57.1			
18	1725						49.5			27.50
19	1700						52.0		61.6	8.93
									50.3	7.30
20	1700						30.9			
21	1700						56.2			
22	1700	2.6					64.2			
23	1700	5.3					36.4			
24	1675	7.8					52.2			
25	1725	2.6					71.2			
26	1725	5.3					54.5		73.2	10.62
									65.9	9.56
27	1725				N_2 540		57.7			
28	1750						75.7	3.05	190.0	27.56
									175.1	23.40
29	1725						70.5	3.06	120.7	17.51
									98.3	14.26
30	1700						62.6			
31	1675						32.5			
32	1725	2.6					40.4		122.5	17.77
									57.0	8.27

TABLE 2-2. SUMMARY OF COLD WALL REACTOR EXPERIMENTS FOR THE $SiCl_4$-H_2-N_2-NH_3-ADDITIVE SYSTEM

RUN CW-3	T K	P KPa	FEED RATES cc/min $SiCl_4$	NH_3	H_2	N_2	ADDIT.	FLOW	Si/NH_3	RATE mg/min	DENS. g/cm^3	MOR MN/m^2	MOR KSi
37	1705	5.3	57	57	540	113	-	-	1.00	18.4			
38	↓	↓	↓	↓	540	↓	C_3H_8	113	↓	(a)			
39					540	85	C_3H_8	28		8.2			
40					540	188	C_3H_8	6		30.1			
41					540	57	C_3H_8	57		26.8			
42					540	57	C_3H_8	57		15.7(b)			
43					540	57	C_3H_8	57		(c)			
44	1750		177	267	540	540	-		0.66	35.5		129.0	18.71
46	1800		177	267	-		-			38.9		129.9	18.84
												121.8	17.66
47	1850				-		-			47.2		47.5	6.89
												41.1	5.96
48	1800				-					43.3		124.2	18.0
												92.1	13.36
50					-	625	CCl_4	17		40.9		84.7	12.28
												70.9	10.28
51					-	576	CCl_4	9		43.8	2.89	85.2	12.36
52					-	550	CCl_4	2		42.6	2.91	161.3	23.39
											3.12	158.4	22.97
53					-	540	-	-		41.7			
55	1750				-	540	-	-		40.0			
56	1800				-	540	BCl_3	2		(d)			

(a) Thin, flaky graphitic deposit
(b) Alternating C_3H_8 on, off
(c) Thin, flaky graphitic deposit with globules of silicon metal.
(d) Deposit formed in feed tube

TABLE 2-3. DEPOSITION RATE OF SILICON NITRIDE VERSUS TEMPERATURE - COLD WALL REACTOR

RUN	T(K)	FEED RATE (CC/MIN) $SiCl_4$	NH_3	CARRIER	DEPOSITION RATE MG/MIN
A. HYDROGEN CARRIER Si/N = 3.3, P = 5.3 KPa					
1	1750	230	68	700	48.8
5	1700	230	68	700	50.7
6	1650	230	68	700	34.1
B. HYDROGEN CARRIER Si/N = 0.66, P = 5.3 KPa					
17	1750	177	267	540	57.1
18	1725	177	267	540	49.5
19	1700	177	267	540	52.0
24	1675	177	267	540	52.2
C. NITROGEN CARRIER Si/N = 3.3, P = 5.3 KPa					
8	1800	230	68	700	52.2
13	1750	230	68	700	60.4
14	1650	230	68	700	30.8
D. NITROGEN CARRIER Si/N = 0.66, P = 5.3 KPa					
28	1750	177	267	540	75.5
29	1725	177	267	540	70.5
30	1700	177	267	540	62.6
31	1675	177	267	540	32.5

TABLE 2-4. VARIATION IN FLEXURE STRENGTH WITH PROCESS CONDITIONS - COLD WALL DEPOSITS

FLEXURE STRENGTH (MOR)*				CARRIER	TEMP. (K)	PRESS. (KPa)	Si/NH_3 RATIO	RUN NO.
MN/m^2		KSI						
190.3	175.1	27.6	25.4	N	1750	5.3	0.66	28
189.6	58.6	27.5	8.5	H	1725	5.3	0.66	18
120.7	98.6	17.5	14.3	N	1725	5.3	0.66	29
122.7	57.2	17.8	8.3	N	1725	2.7	0.66	32
86.2	47.5	12.5	8.0	H	1750	5.3	3.3	1
73.1	66.2	10.6	9.6	H	1725	2.7	0.66	26
75.2	45.5	10.9	6.6	H	1700	5.3	3.3	5
61.4	50.3	8.9	7.3	H	1700	5.3	3.3	19
52.4	41.4	7.6	6.0	N	1750	5.3	3.3	13

* Two specimens from each run.

TABLE 2-5. SUMMARY OF ONE INCH HOT WALL (HW-1) REACTOR EXPERIMENTS*

RUN	T	P	Feed Rate (STP) cc/min					DEP. RATE		$SiCl_4$	Dens.	M.O.R. (Average)		Color in Transm. Visible	Fluoresc. U.V. Center/Ends	Comment
	K ± 15	Pa	NH_3	$SiCl_4$	N_2	Additive(%) of $SiCl_4$		mg/min (Avg)	mm/hr (mils/hr) (max)	Conv.	gm/cm^3	MN/m^2	Ksi			
1	1700	400	62	36	460	-	-	40.8	0.14 (3.6)	54.4	n.m.	n.m	n.m.	Brown Cryst	-	2 hr run, too thin for test
2	1700	1330	60	36	460	-	-	55.5	0.21 (5.3)	74.0	3.14	138.8	20.04	Brown Cryst	None/orange	Higher P, High Rate
4	1710	400	262	36	460	-	-	41.2	0.12 (3.1)	54.9	3.11	n.m.	n.m.	Lt. Brn.Cryst	None/orange	Broken in Recovery
6	1710	400	83	36	460	BCl_3	2.4	25.4	0.14 (3.6)	33.9	1.65	188.02	27.13	Clear color	White	I.R. Anal shows Amorp. BN (uncertain BCL_3 feed
8	1710	400-503	62	36	460	BCl_3	1.8	37.2	0.09 (2.3)	49.6	3.13	n.m.	n.m.	Blue, Cryst	None	Two Layer Depos.
9	1710	400	63	36	460	BCl_3	11.4	27.1	0.10 (2.5)	36.1	n.m.	n.m.	n.m.	Milky White Amorph.	White-pink	Cracked, Poss. BN
10	1705	530	60	36	460	H_2S	100 -	30.0	0.11 (2.8)	40.0	3.18	136.45	19.79	Dk. Brn.Cryst	None	
12	1710	400	63	36	-	H_2	415 cc/min	25.8	0.07 (1.8)	40.0	3.17	254.36	36.89	Tan, Brn. Cryst	None/dark red	Low Rate, Fine Grain
13	1710	400-530	62	36	460	C_3H_8	2	31.9	0.13 (3.3)	42.5	3.18	n.m.	n.m.	Brn. Cryst	None/orange	
14	1700	400-530	62	36	460	C_3H_8	8.6	33.8	0.11 (2.8)	45.1	3.17	147.07	21.33	Dk Brn, Cryst	None/orange	
15	1695	400	65	36	460	-	-	22.9	0.12 (3.1)	30.5	3.17	159.83	23.18	Dk Brn, Cryst	None/dark red	
16	1700	400-530	62	36	460	CH_3SiCl_3	13	39.6	0.16 (4.1)	52.8	3.15	165.62	24.02	Dk Brn, Cryst	None/orange	
17	1700	530	62	36	460	$AlCl_3$	1.4	25.0	0.14 (3.6)	33.3	3.12	174.61	27.49	Blue Cryst	None	T_{AlCl_3} = 100°C
18U	1715	530	182	36	460	$AlCl_3$	31	40.4	0.15 (3.8)	53.9	3.13	211.26	30.64	Blue Cryst	None	T_{AlCl_3} = 130°C
18L	1715	530	182	36	460	$AlCl_3$	31		-	-	-	81.22	11.78	Blue Black	None	Botryoidal, Blue-White
19U	1700	530	260	36	460	$AlCl_3$	135	37.9	0.15 (3.8)	50.5	3.20	140.66	20.40	Blue Cryst	None	T_{AlCl_3} = 150°C
19L	1700	530	260	36	460	$AlCl_3$	135		-	-	-	131.7	19.10	Blue Black	None	Nodular

* Deposition Geometry (See Figure 2-3, Type E)

TABLE 2-6. SUMMARY OF FLEXURE STRENGTH (MOR) AND FRACTURE SURFACE APPEARANCE OF ONE INCH HOT WALL REACTOR SPECIMENS

RUN (ADDIT.)	SPEC. NO.	MOR MN/m^2	MOR (Ksi)	FRACTURE SURFACE
2	1	130.47	(18.922)	gl FDL, CX C, Col.
-	2	145.92	(21,163)	thin gl. FDL., CX, C. Col.
	$\bar{X}$	138.18	(20.04)	
	S.D.%	9.92		
6	1	155.96	(22,620)	
(BCl_3)	2	193.88	(28,119)	
	3	189.62	(27,487)	gl, transparent
	4	208.33	(30,215)	Anal. indicates
	5	187.50	(27,193)	Amorph. BN
	$\bar{X}$	188.02	(27,130)	
	S.D.%	10.91		
10	1	144.62	(21,700)	CX, C-f col., uneven break
(H_2S)	2	164.81	(23,903)	thin gl. FDL, CX c-f col.
	3	133.36	(19,342)	thin gl. FDL, CX c-f col.
	4	144.16	(20,908)	thin gl. FDL, CX c-f col.
	5	45.77	(13,089)	C. col., thin
	$\bar{X}$	136.45	(19,790)	
	S.D.%	21.99		
12	1	254.96	(36,978)	fc, no gl. FDL
(Std.,	2	217.62	(31,563)	col. no gl. FDL
with H_2	3	294.43	(42,703)	vf col., no gl. FDL
carrier)	4	250.40	(36,316)	col., no gl. FDL
	$\bar{X}$	254.36	(36,978)	col., no gl. FDL
	S.D.%	13.43		
14	1	132.43	(19,207)	gl. FDL, CX, col.
(C_3H_8)	2	118.86	(17,238)	Nodule, void at break, gl FDL, CX, col.
	3	160.22	(23,237)	gl. FDL, CX, col.
	4	147.91	(21,452)	thin gl FDL, CX, col.
	5	175.91	(25,513)	no gl. FDL, CX, col.
	$\bar{X}$	147.07	(21,330)	
	S.D.%	16.28		
15	1	156.79	(22,740)	gl FDL, col.
(Std.	2	202.61	(29,385)	gl FDL, col.
with N_2	3	152.97	(22,186)	gl FDL, col.
Carrier)	4	126.97	(18,389)	gl FDL, C. col.
	$\bar{X}$	159.83	(23,181)	
	S.D.%	21.41		

gl. = glassy, c = coarse, f = fine, col. = columnar

LDL = last deposited layer, CX = crystalline

FDL = first deposited layer

TABLE 2-6. SUMMARY OF FLEXURE STRENGTH (MOR) AND FRACTURE SURFACE APPEARANCE OF ONE INCH HOT WALL REACTOR SPECIMENS (Cont)

RUN (ADDIT.)	SPEC NO.	MOR MN/m^2	MOR (Ksi)	FRACTURE SURFACE
16 (CH_3SiCl_3)	1	195.96	(28,420)	gl. FDL, col.
	2	208.13	(30,186)	gl. FDL, col.
	3	140.05	(20,312)	2 Sep. layers: gl. + col.
	4	131.75	(19,108)	gl. FDL, col.
	5	152.09	(22,058)	gl. FDL, col.
	$\bar{X}$	165.62	(24,020)	
	S.D.%			
17 ($AlCl_3$) (1000C)	1	220.39	(31,964)	c. col. no gl. FDL
	2	203.06	(29,451)	c. col. thin gl. FDL
	3	151.32	(21,947)	c. col. no gl. FDL
	4	202.04	(29,303)	col. thin fine CX FDL
	5	185.69	(26,931)	c. CX col., no gl. FDL
	6	174.61	(25,324)	c. col. no gl. FDL
	$\bar{X}$	189.52	(27.486)	
	S.D.%	13.55		
18L ($AlCl_3$ 1300C Inlet Depos.)	1	78.75	(11,421)	gl. FDL, broad, white/blue col.
	2	83.70	(12,139)	gl. FDL, broad, white/blue col.
	$\bar{X}$	81.22	(11,780)	
	S.D.%	5.41		
18U ($AlCl_3$ 1300C Center, Upper Deposit)	1	298.49	(43,291)	f CS FDL, f CX, C.
	2	187.49	(27,192)	f CS FDL, f CX, C.
	3	151.10	(21,915)	gl. FDL, C. col. CX
	4	207.99	(30.166)	c col., CX
	$\bar{X}$	211.26	(30,640)	
	S.D.%	32.21		
18U (Polished)	1	314.40	(45,600)	
	2	320.26	(46,450)	
	$\bar{X}$	317.33	(46,025)	
	S.D.%	0.92		
19L ($AlCl_3$ 1500)	1	124.22	(18,016)	fg. FDL, CX col.
	2	146.23	(21,209)	fg. non col. FDL, c. col.
	3	124.72	(18,088)	CX white FDL, blue f.g. non col. + CX col.
	$\bar{X}$	131.69	(19,099)	
	S.D.%	10.77		
19U ($AlCl_3$ 1500)	1	149.61	(21,698)	V fg FDL, not glassy (1/3) + col.(2/3)
	2	199.82	(28,981)	V fg FDL (1/2), col. to LDS
	3	168.69	(24,465)	some fg, remainder col.
	4	90.86	(13,178)	glassy FDL, c. col.
	5	94.41	(13,692)	c. col.
	$\bar{X}$	140.66	(20,400)	
	S.D.%	35.95		

TABLE 2-7. SUMMARY OF FOUR-INCH HOT WALL (HW-4) REACTOR EXPERIMENTS

Run	Depos. Geom.	Code*	Temp (K)	Press. (Pa)	time (hrs)	Flow cc/min					Remarks
						SiF_4	NH_3	H_2	N_2O	N_2	
328	Disc (⊥)	D	1750	1330	8	280	480	580	5	-	
329	Disc (⊥)	D	1750	1330	3	560	960	1164	10	-	
378	Plates (II)	C	1725	998	8	840	1440	1750	18	-	
379	Plates (II)	C	1725	1330	8	840	1440	1750	18	1750	
382	Plates (II)	C	1725	1330	8	840	1440	1750	18	1750	
383	Plates (II)	C	1725	1330	8	840	2880	1750	20	3500	
391	Dome	D	1725	1330	10	840	1440	1750	-	-	Ground/Polished
392	Dome	D	1715	1330	9	420	720	875	-	-	Air Leak/Not Polished
393	Dome	D	1715	1330	14	840	1440	1750	-	-	Ground and Polished
394	Dome	D	1715	440	28	420	720	875	-	-	Ground and Polished

*See Figure 2-3

TABLE 2-8. SUMMARY OF FLEXURE STRENGTH (MOR) DATA ON FOUR-INCH, HOT WALL REACTOR SPECIMENS (FLAT PLATE, OXYGEN DOPING)

RUN NO.	FLEXURE STRENGTH (MOR) (MNm^{-2})	FLEXURE STRENGTH (MOR) (psi)	FRACTURE MODE	GRAIN SIZE (μm)
328** DISC (⊥)	191.88 233.39 $\bar{X}$ = 212.63	27830 33850 30840	INTERGRANULAR	∿150 (FIG. C-1)
329* DISC (⊥)	169.89 200.98 200.02 $\bar{X}$ = 190.85	24640 29150 29010 27680	MIXED (BIMODAL)	∿ 30 (FIG. C-2)
378** PLATE (∥)	55.85 68.95 57.23 53.09 54.47 $\bar{X}$ = 57.92	8100 10000 8300 7700 7900 8400	INTERGRANULAR	∿175 (FIG. C-3)
379** PLATE (∥)	59.29 70.33 80.67 82.05 $\bar{X}$ = 73.08	8600 10200 11700 11900 10600	INTERGRANULAR	∿100 (FIG. C-4)
382** PLATE (∥)	103.42 109.63 97.91 99.28 122.73 124.11 106.18 $\bar{X}$ = 108.94	15000 15900 14200 14400 17800 18000 15400 15800	TRANSGRANULAR	∿ 40 (FIG. C-5)
383** PLATE (∥)	106.87 116.52 137.21 118.59 122.73 119.28 139.27 $\bar{X}$ = 122.73	15500 16900 19900 17200 17800 17300 20200 17800	TRANSGRANULAR	∿ 40 (FIG. C-6)

* FDS IN TENSION, GROUND SURFACES

** LDS IN TENSION, AS DEPOSITED SURFACES

TABLE 2-9. BOND ENERGY VALUES OF INTEREST IN INTERPRETING DEPOSITION KINETICS OF SILICON NITRIDE

Species	Free energy of formation (Kcal(mole) ca 1500K
SiO_2	-138(a)
Si_2ON_2	-110(b)
$1/4(Si_{11}N_{15}O_{0.3})$	-57.4(b)
Si_3N_4	-40(b)
Bond	**Bond Energy (Kcal/mole)(c)**
Si-O	184 ± 3
Si-N	105 ± 9
Si-F	116 ± 12
H-F	139.9 ± 0.3
Si-Cl	105 ± 12
H-Cl	103.1
Si-H	71.4 ± 1.2
Al-N	71 ± 23
Al-O	116 ± 5
B-N	93 ± 12
B-O	192.7 ± 1.2
N-H	75
O-H	102.3 ± 0.3
C-O	257.3 ± 0.77

(a) JANAF Tables

(b) Ref. 14

(c) Handbook of Chem. and Physics, 56th ed. CRC Press, 1976

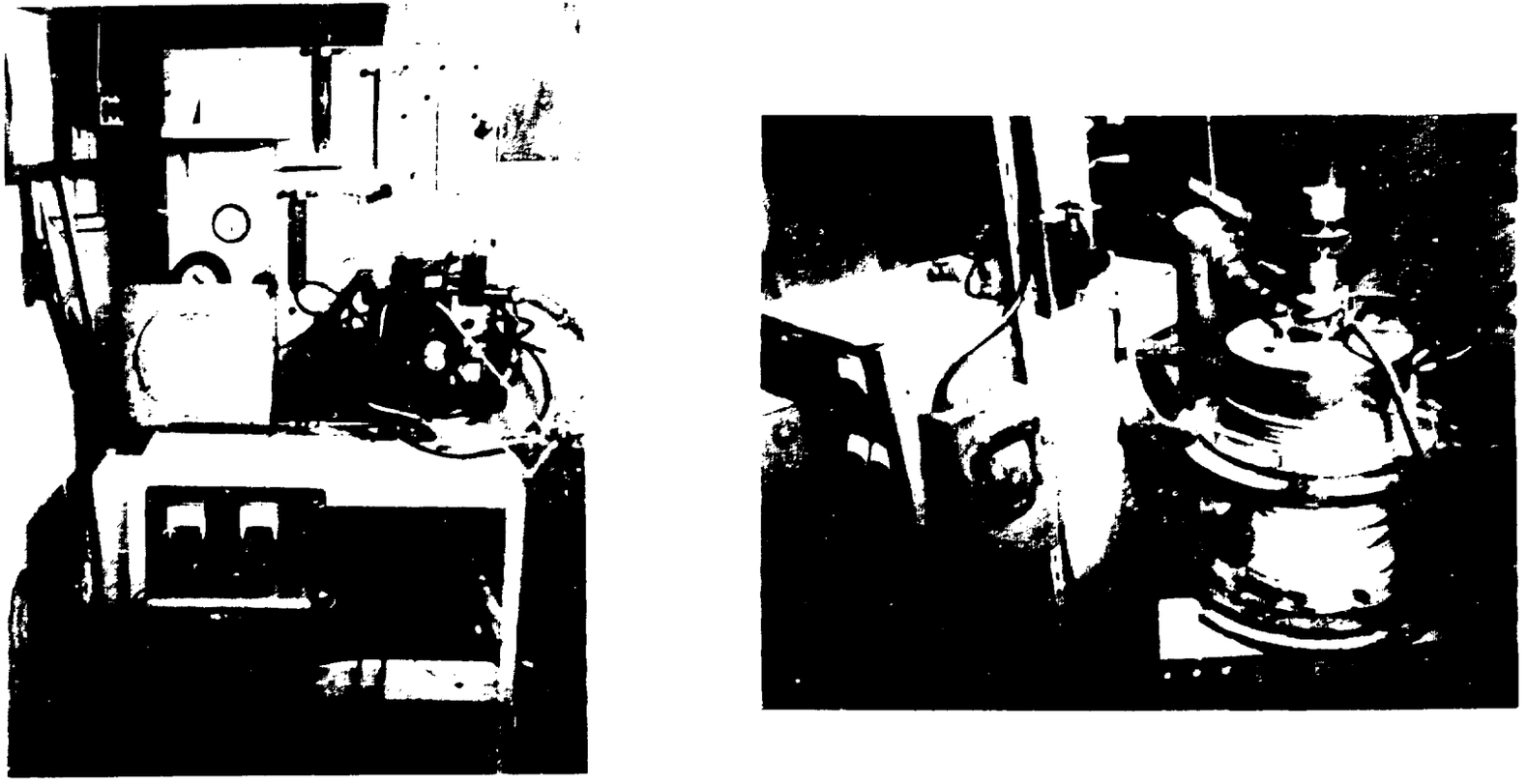

Figure 2-1. Hot Wall Reactors One Inch Diameter Hot Zone (Left). Four-Inch Diameter Hot Zone (Right).

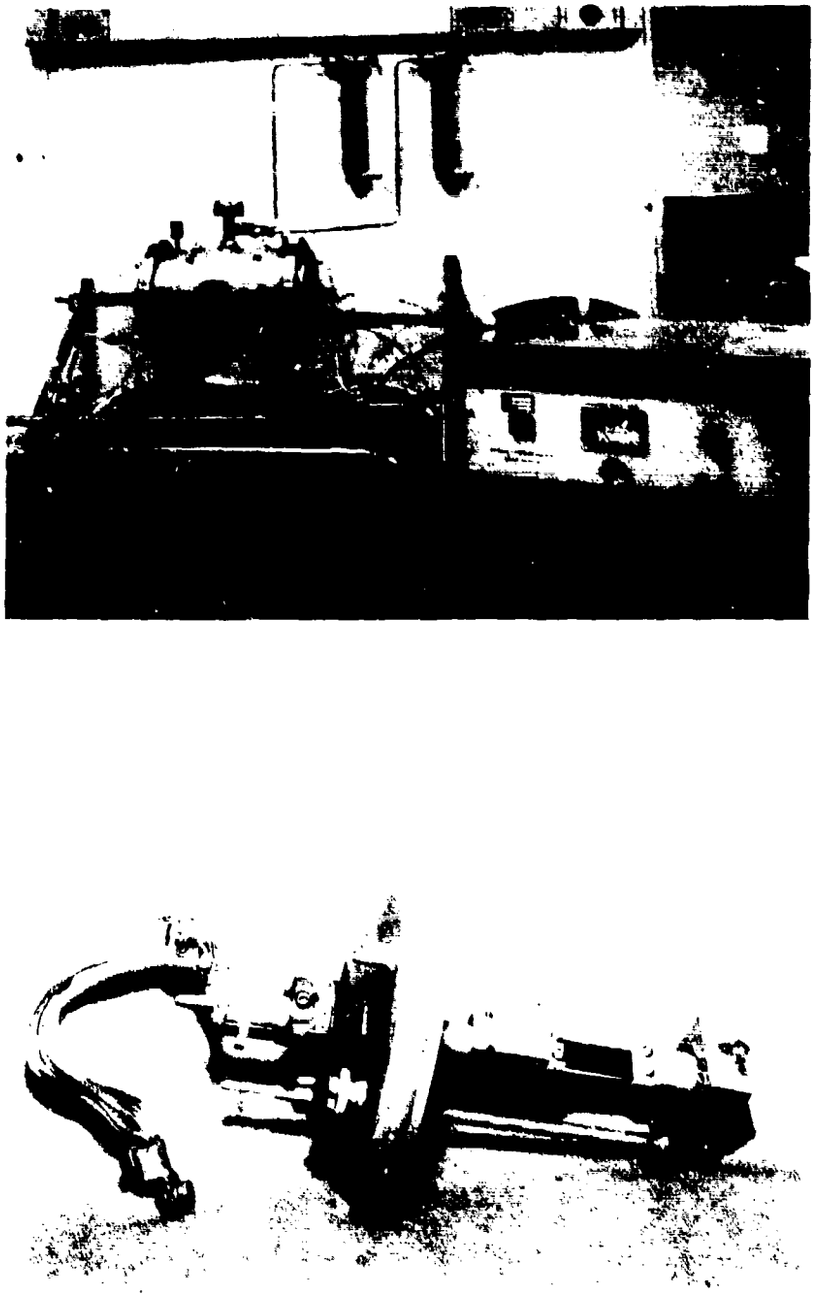

Figure 2-2. Cold Wall Reactor System (Top). Deposition Substrate Mount with Retracting Attachment to Maintain Flatness (Bottom).

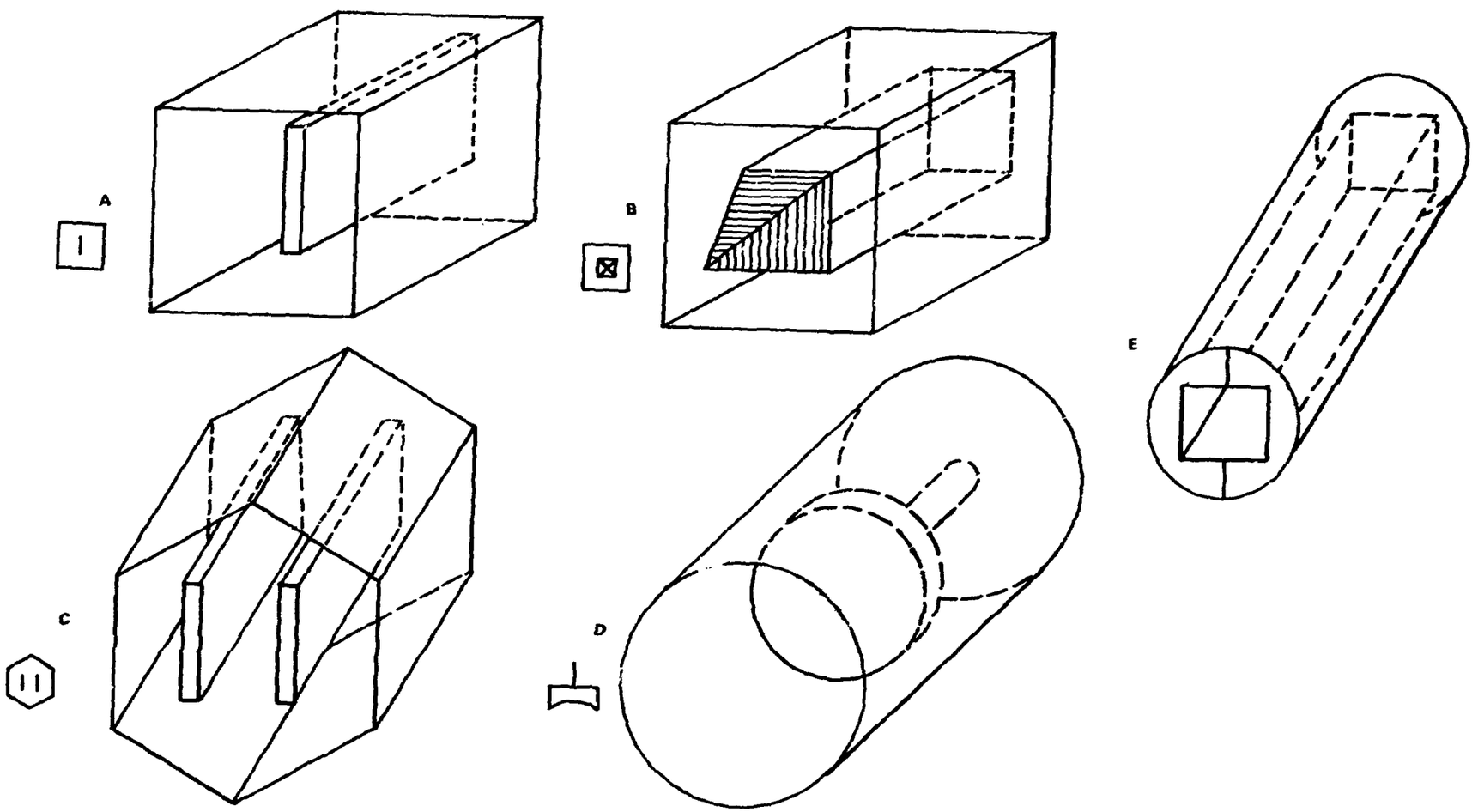

A. SQUARE BOX – PLATE INSERT
B. SQUARE BOX – SQUARE PLUG INSERT, TAPERED TIP
C. HEXAGONAL BOX – TWO PLATES INSERTED
D. PLATE OR DOME, PERPENDICULAR TO FLOW
E. CHANNEL, HW-1 GEOMETRY, GRAFOIL LINER.

Figure 2-3. Schematics of Deposition Geometries Used in Hot Wall Deposition Runs. View from Gas Inlet.

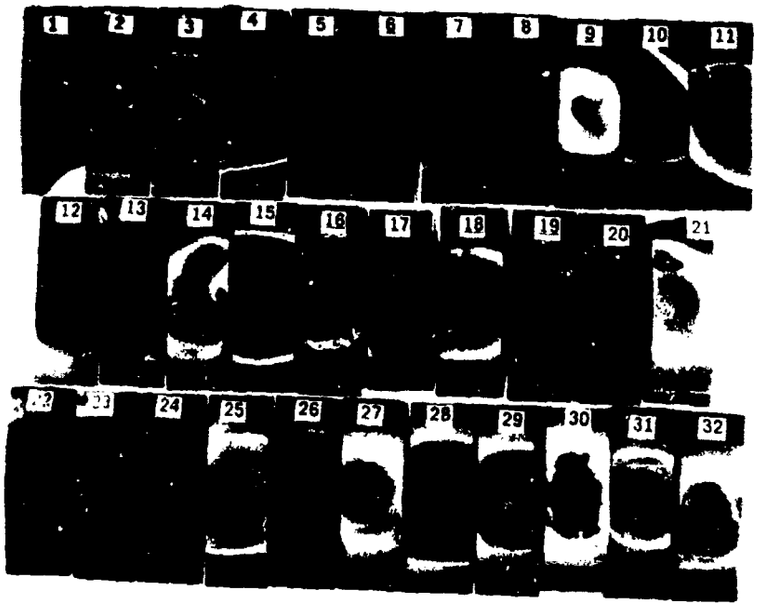

MAG. 0.53X

Figure 2-4. General Appearance of Last Deposited Surfaces of Cold Wall Reactor Runs Using Both H_2 and N_2 Carrier Gases (See Table 2-1). Substrate Dimensions: 50.8 x 19.1 x 0.51 mm.

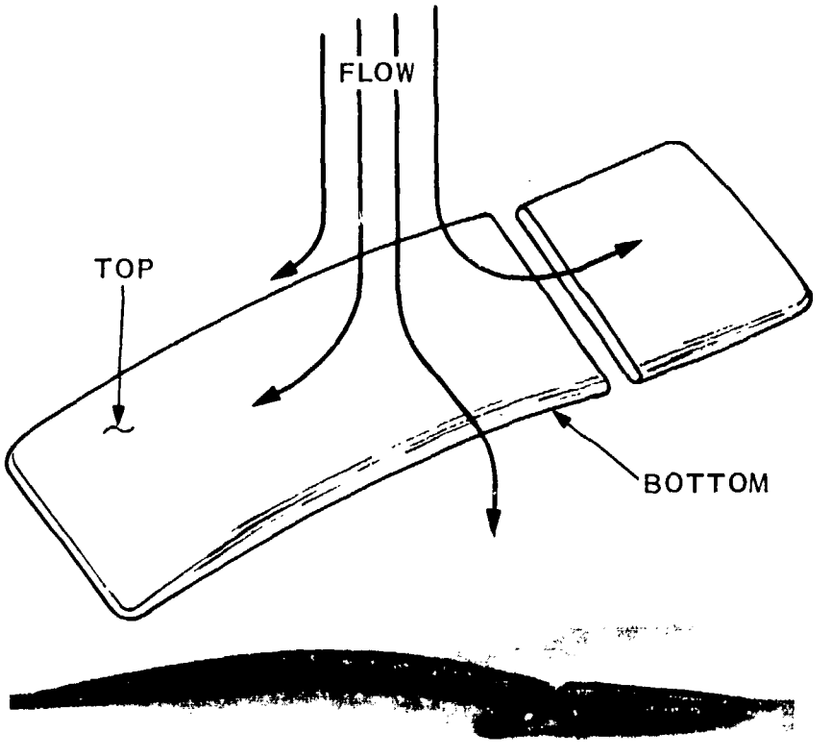

EDGE VIEW OF DEPOSITION PLATE (A)

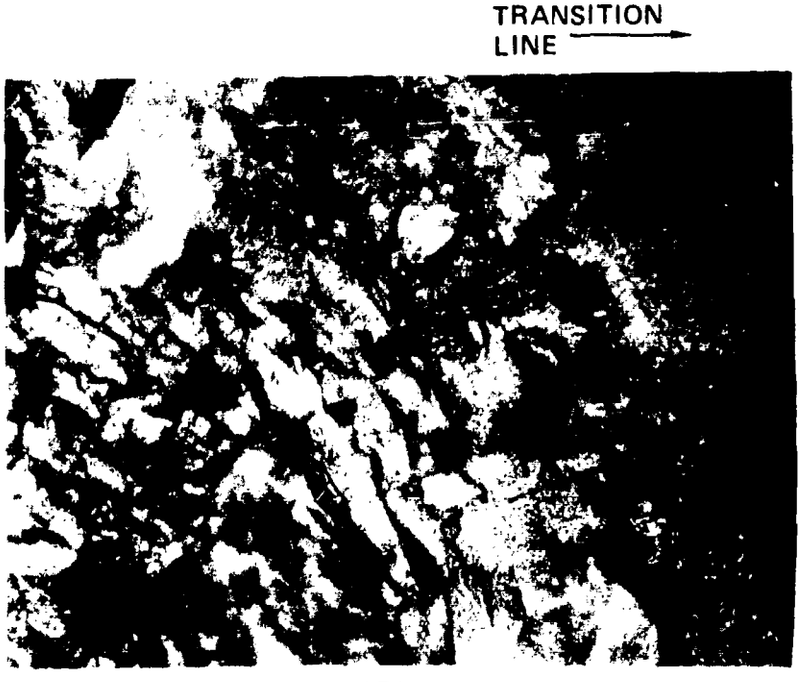

(C) BOTTOM EDGE

Figure 2-5. Typical Edge Deposit from Cold Wall Reactor (A). Cross Sectional View of Edge (B) Shows Change in Structure Due to Flow Separation at Edge of Substrate. Gas Flow is Downward. Upper-Half (near top edge) Shows Typical Columnar Growth. Bottom Half (near bottom edge) Shows Interrupted Columnar Growth (C) below Transition Line.

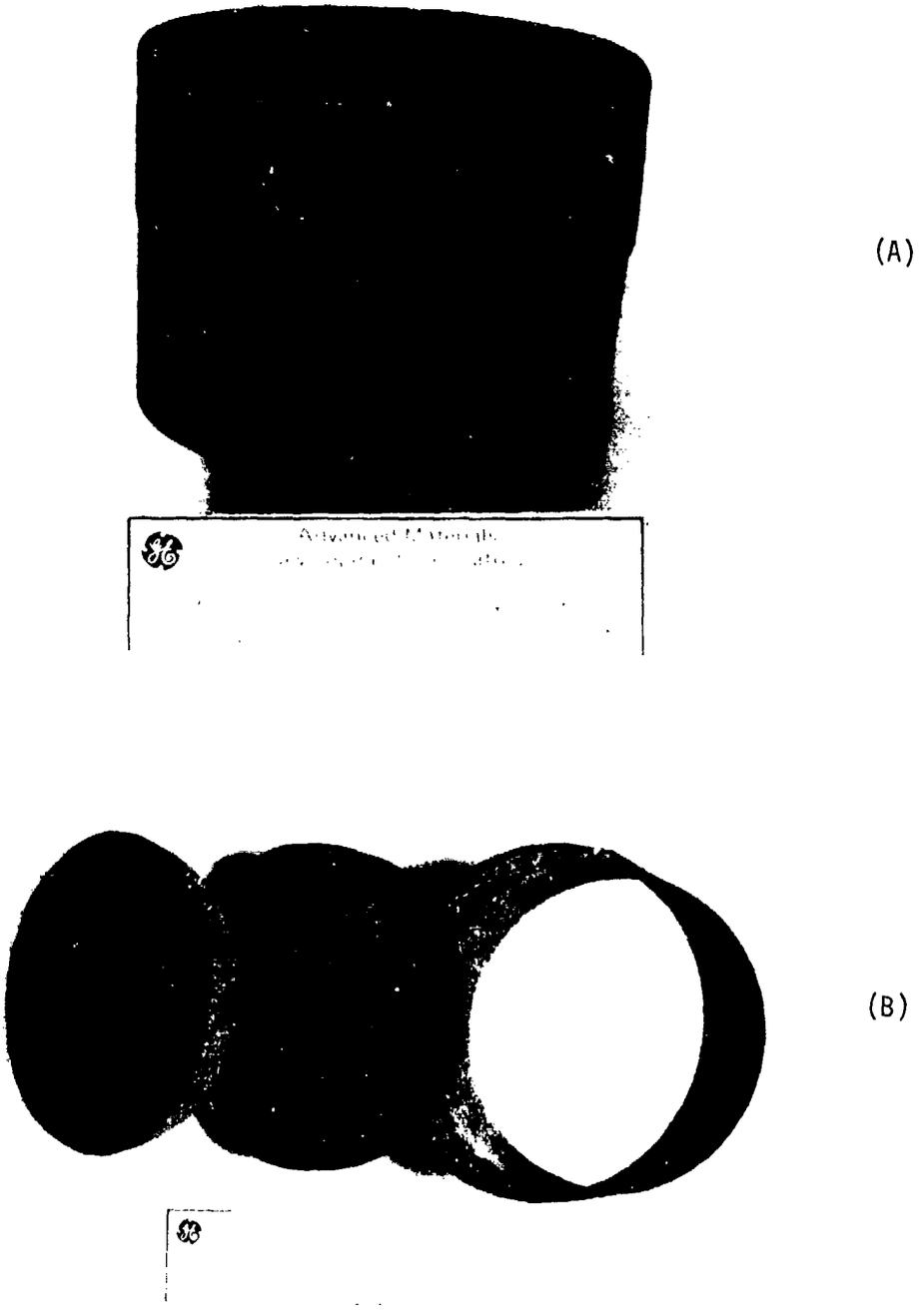

Figure 2-6. As-Deposited CVD α-Si_3N_4 Dome: Mandrel Assembly Before Sectioning (A). As-Deposited CVD α-Si_3N_4 Dome and Sectioned Side and Rear Deposits After Removal of Graphite Mandrel by Oxidation (B). Run No. HW4-394. As Deposited Thickness (Stagnation Point) = 1.58 mm.

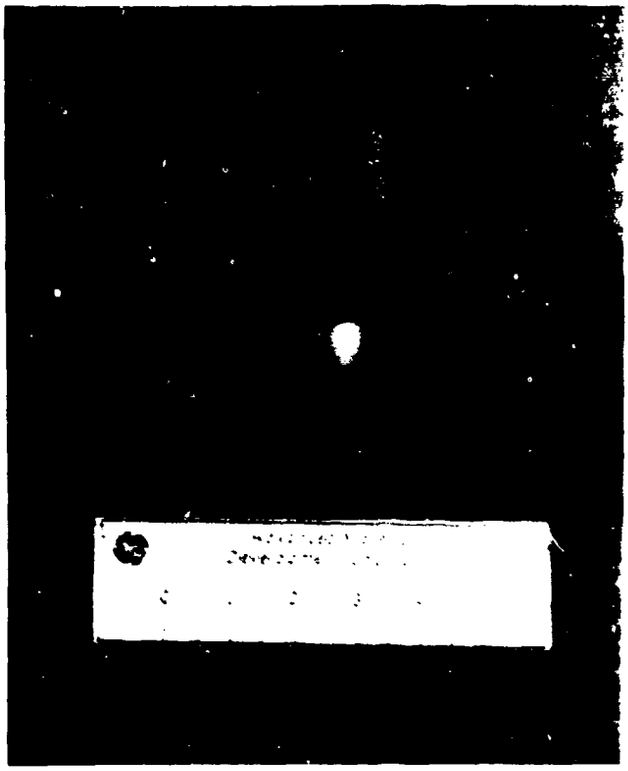

Figure 2-7. Lapped and Polished CVD α-Si_3N_4 Dome. (Run No. HW4-393). Finished Thickness = 1.40 mm.

MAG 75X

MAG 150X

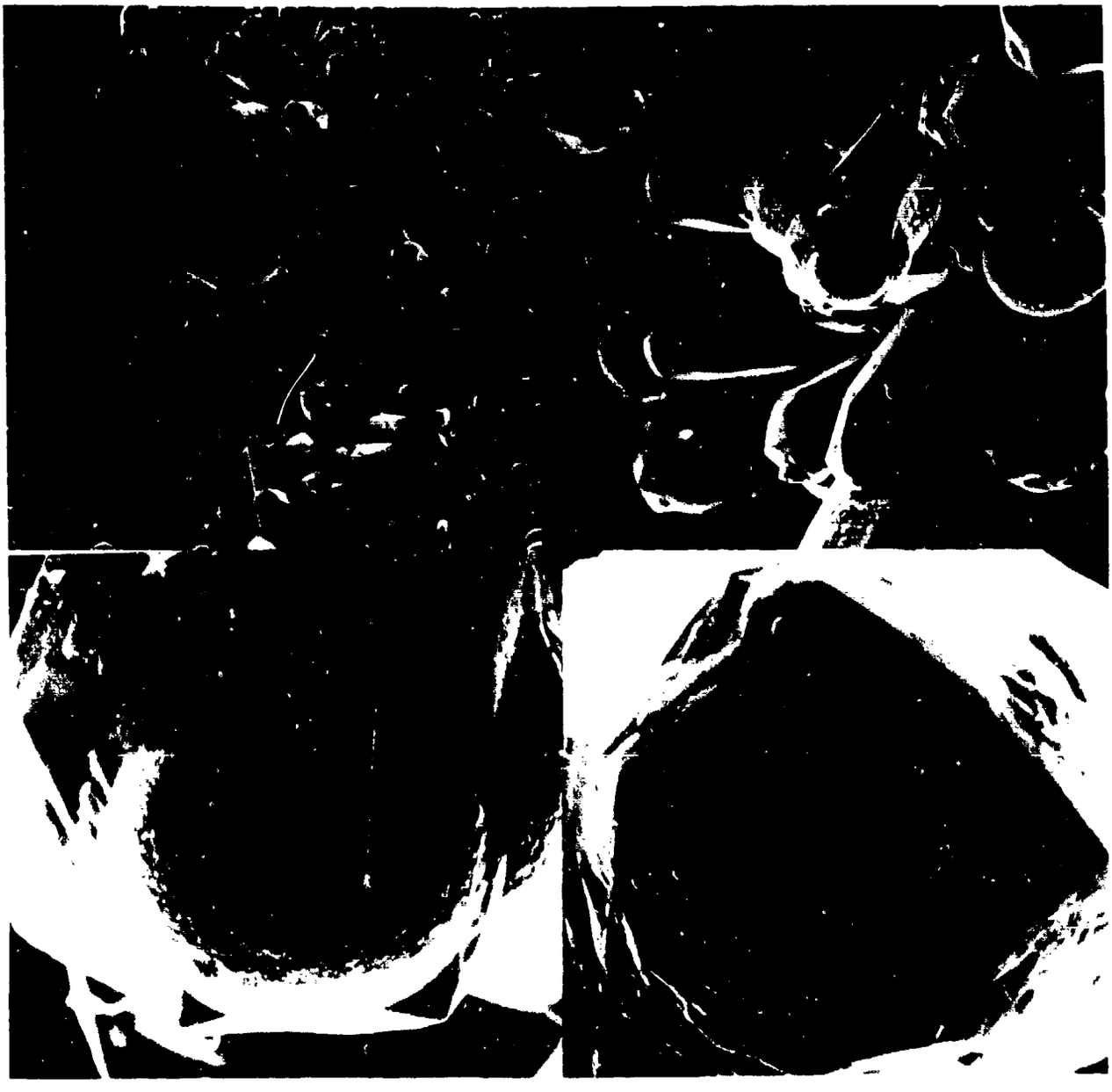

MAG 500X

MAG 500X

Figure 2-8. SEM Views Showing Development of Crystal Structure From Droplets Deposited in Cold Wall Reactor (CW-24), H_2 Carrier. Evidence of Liquid Phase in Hot Wall Runs With Added Oxygen (Figure C-6) Consists of Lace-Like Residue Over Crystallite Surfaces.

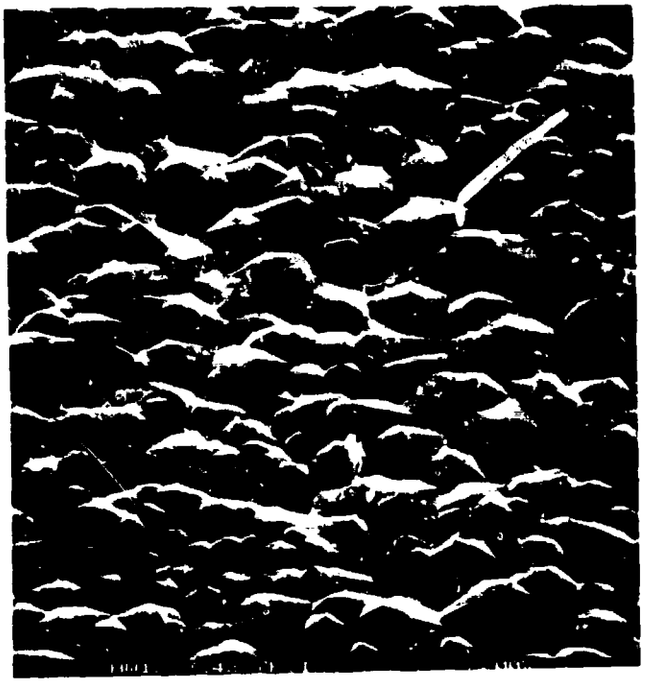

LAST DEPOSITED SURFACE

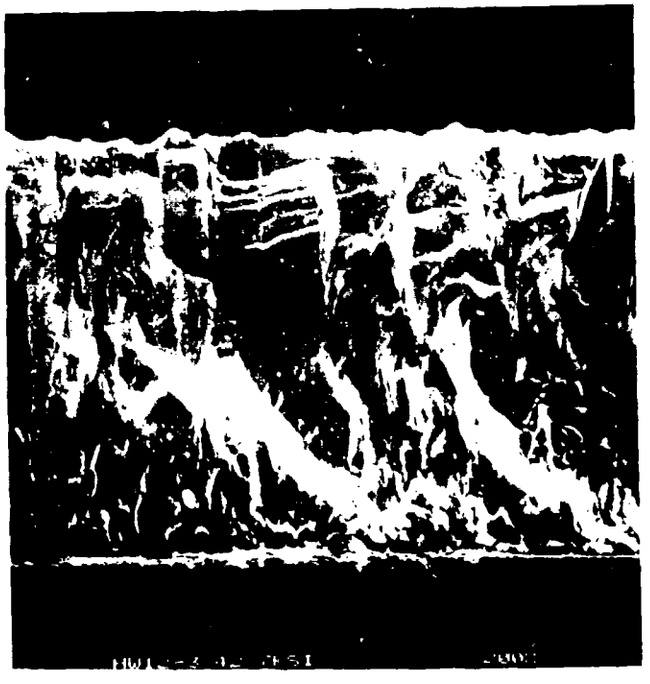

FRACTURE SURFACE

Figure 2-9. SEM Photomicrographs of Typical Hot Wall Deposition Illustrating Columnar Growth Habit With Mutually Restrained Lateral Growth. (See Also Figure B-3).

Figure 2-10. SEM Photomicrograph Illustrating Intergranular Fracture Mode Associated With Oxygen Doped CVD α-Si_3N_4 Deposit. (See Also Figure C-3).

COLD WALL REACTOR

HOT WALL REACTOR

Figure 2-11. SEM Photomicrographs Illustrating "Fastest-Growing-Face" Morphologies in Both Cold Wall and Hot Wall Experiments (See Also Figures A-B and C-4).

Figure 2-12. SEM Photomicrograph Showing Interruped Growth Phenomena Associated With Aluminum Dopant. (See Also Figure B-10).

Figure 2-13. SEM Photomicrograph of LDS of Boron-Doped CVD α-Si_3N_4 Deposit Showing Growth Habit Normal to Deposition Direction. (See Also Figure B-1).

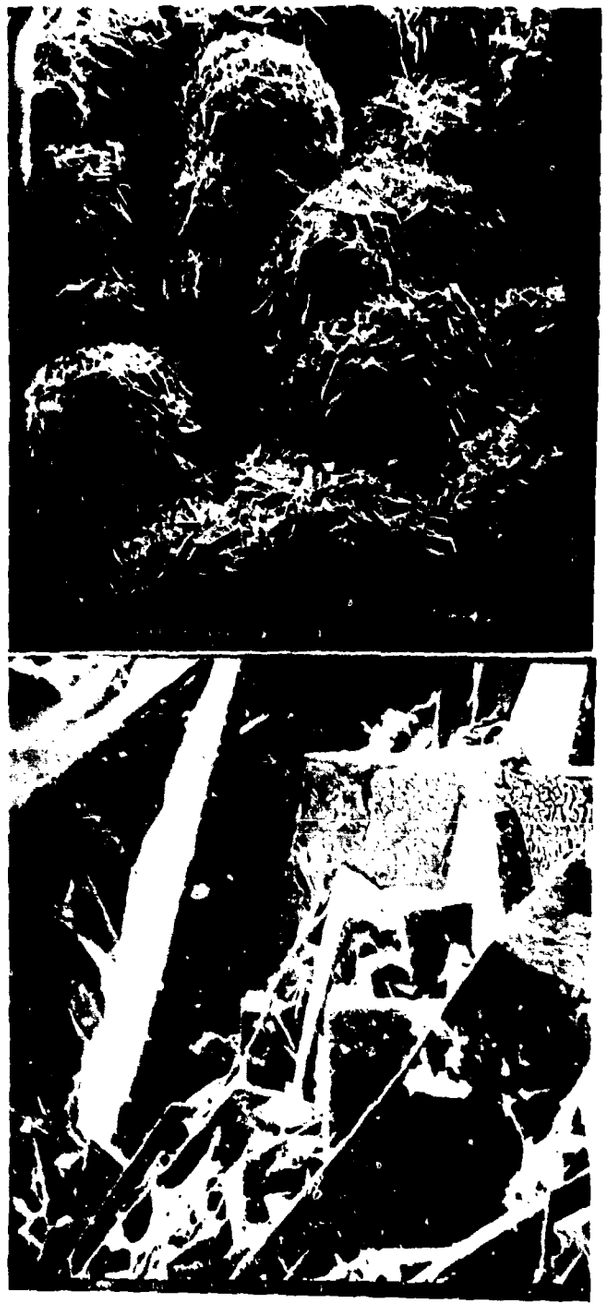

NODULAR GROWTH
HABIT ON LDS

CRYSTALLINE FACETS
ON SURFACE OF
NODULES

Figure 2-14. SEM Photomicrographs Illustrating Nodular Growth Habit and Development of Crystalline Surface Facets (See Also Figure A-1).

SECTION 3.0
PHYSICAL PROPERTY CHARACTERIZATION

SECTION 3.0

PHYSICAL PROPERTY CHARACTERIZATION

3.1 ELECTROMAGNETIC PROPERTIES

3.1.1 Infrared Transmittance of Polished Domes

Specular and discrete-hemispherical transmittance properties of three polished dome segments were measured in the infrared wavelength region. The fabrication and finishing of these domes was described earlier in paragraph 2.3.3. Figures 3-1, 3-2, and 3-3 illustrate the transmittance data. Also shown are the associated microstructures as viewed from the concave side with transmitted light incident on the convex side (stagnation region) of each dome. Domes 400-393 and 400-394 exhibited microstructures with considerably lower defect density than dome 400-391. Correspondingly, dome 400-391 which was somewhat thinner than the others had the lowest specular and hemispherical transmittance levels. In the case of domes 400-393 and 400-394, the 68 percent hemispherical levels at 2.71 microns indicate that near intrinsic transmittance levels are being achieved, however, volume scattering (due to an undesirable microcrack density) is preventing achievement of correspondingly high specular transmittance levels. Each dome exhibited near identical transmittance cut-offs in the 4.6 micron region. Thus, as previously reported, CVD α-Si_3N_4 irdomes would have a high frequency bandpass extending from the near ultraviolet (exact cut-on a function of deposit color) to just beyond the strong CO_2 atmospheric absorption band in the 4.2 to 4.4 micron range. Figures 3-4, 3-5, and 3-6 show the computed absorption coefficients for each dome confirming previous qualitative estimates that dome 400-391 had the poorest optical properties. Figure 3-7 compares the microstructures and tabular absorption coefficient data for the best and poorest domes from an infrared window point of view. Particularly noteworthy is the rather respectable absorption coefficient computed for dome 400-394 based upon its hemispherical transmittance at 2.71 microns. This level is near current state-of-the-art window materials which possess significantly poorer thermal shock resistance.

Thus, further processing studies may be warranted to continue the search for deposition conditions leading to microstructures free of microcrack defects. The achievement of a finer columnar growth habit should minimize the density and size of crystal boundary microcracks since it is already known that a lower microcrack

density of smaller flaw size exists in the finer-grained first deposited layer of current deposits. Also, long-time high-temperature annealing experiments could be fruitful in promoting microcrack healing through the mechanism of self-diffusion via volume, grain boundary, and surface diffusion modes.

3.1.2 Effect of Additives or Infrared Transmittance

X-ray diffraction analyses of Al doped Si_3N_4 specimens (Table 2-5, Runs 17 through 19) indicate retention of the α-Si_3N_4 structure although some solubility may exist as evidenced by the distinct color change observed from the usual amber color to blue. Figure 3-8 shows the specular infrared transmittance of one of these specimens together with a transmitted-light photomicrograph. The grey regions of the photomicrograph correspond to the blue areas of the specimen indicating some degree of inhomogeneity exists in the deposit. A comparison of Figure 3-8 with Figure 3-3 shows that the Al doped Si_3N_4, while having a similar transmittance cut-off, now exhibits distinct absorption bands at 3220 cm^{-1} and a doublet at 3100 and 3120 cm^{-1}. Additional characterization of this new class of Si_3N_4 would be desirable in future studies.

Similar color changes were also noted in the B doped Si_3N_4 material (Table 2-5, Run 8). In this instance, distinct shifting in the x-ray diffraction peaks for α-Si_3N_4 were noted suggesting some degree of solubility of B atoms in the Si_3N_4 lattice.

In this same experimental series a water-clear amorphous boron nitride specimen was synthesized (Table 2-5, Run 6) which also contained more than a trace amount of Si atoms according to emission spectrographic analyses. Figure 3-9 shows the specular infrared transmittance behavior of this specimen together with a transmitted-light photomicrograph. The reduced infrared transmittance cut-off, compared to α-Si_3N_4 (i.e. 3.5μ m versus 4.7μ m) correlates with the lower cation atomic mass of the amorphous "Si doped" BN microstructure. The interference rings and the presence of the black crosses in the polarized photomicrograph indicate that the deposit is birefringent with its optic axis normal to the plane of the figure. Petrographic analyses (Ref. 37) of the specimen show the deposit to be uniaxial negative although x-ray diffraction analyses fail to show distinct (hkl) reflections. A turbostratic BN may have been synthesized analogous to turbostratic carbon, i.e. a two-dimensional layer, of hexaginal rings which are stacked at regular intervals but with a complete lack of orientation from layer to layer (Ref. 38).

A comparison of the infrared reflectance of the amorphous "Si-doped" BN with hot-pressed, hexagonal BN in Figure 3-10 also show evidence of incipient crystallization to the hexagonal BN structure as indicated by the evo ving Reststrahlen reflectance bands at approximately 7 and 12 microns.

3.1.3 Radar Transmittance of Flat Plate Deposits

As reported previously (Refs. 1 and 39 through 43), the dielectric properties of CVD α-Si_3N_4 up to 800°C over the frequency range from 8.5 to 24 GHz are superior to published data on the multitude of hot-pressed and reaction sintered silicon nitride modifications. This trend stems primarily from the ultrahigh chemical and phase purity of CVD α-Si_3N_4. Figure 3-11 shows typical dielectric constant and loss tangent data as a function of temperature and frequency. Of particular interest is the low loss tangent levels and the relative temperature insensitivity of both functions. Figure 3-12 compares the dielectric properties of a commercial hot pressed Si_3N_4 with CVD α-Si_3N_4 at 24 GHz. On the basis of these data serious consideration must be given to the CVD modification for radome applications which are considering silicon nitride generically because of its superior thermal shock and erosion resistance potential.

3.2 MECHANICAL PROPERTIES

3.2.1 Strength Potential

The potential for ultrahigh strength exists for covalently-bonded Si_3N_4. Indeed, Knippenberg and Verspui (Ref. 44) report tensile strengths of more than 14,000 MN m^{-2} (>2 million psi) for α-Si_3N_4 fibers grown by the VLS method. Realization of these ultrahigh strengths in monolithic CVD α-Si_3N_4 deposits have been a major goal of this program.

In particular, the Phase 3 program concentrated upon the development of microstructures which were of finer columnar grain size, or of a continuously-nucleated fine-grained morphology, both being free of debilitating grain boundary separations which have limited the achievement of high strength on earlier programs (Refs. 1, 39).

3.2.2 Experimental Results

As has already been described in paragraphs 2.2 and 2.3, screening for major improvements in strength was accomplished through a combination of flexure strength determinations and fractography using scanning electron microscopy.

Appendices A, B, and C document the results of fractographic analyses conducted on both cold wall (Appendix A) and hot wall (Appendices B and C) deposits.

3.2.2.1 Cold Wall Depositions

In general, for the cold wall depositions (Appendix A), transgranular fracture modes were observed with cleavage occurring on unspecified planes resulting in a multifaceted fracture topography. The higher strength levels correlated with a finer-grained, last deposited surface (LDS) morphology. This finer grained LDS morphology was usually associated with lower Si:N ratio (~0.66) depositions as discussed previously in Section 2.0. The addition of the CCl_4 dopant significantly altered the last deposited surface morphology but strength levels were slightly lower than undoped deposits for the more dilute CCl_4 addition.

3.2.2.2 Hot Wall One Inch Reactor Deposits

In general, hot wall deposits in the one inch diameter reactor (Appendix B) had flexure strenghts consistently higher than cold wall deposits. It was in this series that the highest flexure strength was measured, viz., 320 MN m^{-2} (46,450 psi), on an Al doped α-Si_3N_4 modification. Flexure strength levels nearly comparable were also recorded for undoped, fine grained deposits using either N_2 or H_2 carriers. Unexpectedly high flexure strengths were also measured on the amorphous Si doped BN deposit (i.e. 188 MN m^{-2}). This deposit (HW-6) was also unique in that it was the only deposit in this series free of scattering defects (exhibiting water clarity under visible light.)

3.2.2.3 Hot Wall Four-Inch Reactor Deposits

Hot wall deposits in the four-inch diameter reactor (Appendix C) which were doped intentionally with oxygen had lower flexure strengths than comparable undoped deposits. In most instances intergranular failure modes were observed indicating that oxygen additions lower the fracture energy (compared to the single crystal cleavage energy) probably as the result of increases in the chemical grain boundary interface energy (See Equation 2-1).

3.2.3 DISCUSSION

Processing research on silicon nitride has centered on two consolidation methods, viz., hot pressing or sintering Si_3N_4 powder (amorphous, α- or β- forms) with densification aids, and reaction sintering of elemental Si in nitrogen containing environments. In the former method, the achievement of high strength and density occurs as the result of a liquid phase sintering mechanism. The presence of a

grain boundary glass phase, however adversely effects strength retention at elevated temperatures, and also, adversely effects high temperature dielectric properties. Reaction sintered Si_3N_4 (RSSN) on the other hand, while exhibiting lower strength than hot pressed Si_3N_4 (primarily due to a high volume fraction of porosity), retains its strength at elevated temperatures. The presence, however, of unreacted Si in RSSN, has resulted generally in marginal dielectric properties.

On this program a relatively new method of forming Si_3N_4, viz., chemical vapor deposition has been introduced which overcomes potentially many of the previous problems associated with the HPSN and RSSN consolidation methods (i.e., failure to achieve a high degree of phase purity). The excellent dielectric properties of CVD α-Si_3N_4 as well as its synthesis in an optically transparent form are direct manifestations of its intrinsic phase purity, however, its strength potential has not yet been fully exploited. One must look to the Griffith equation for brittle fracture to rationalize the observed strength plateau currently being encountered:

$$\sigma_f = A \frac{K_{IC}}{\sqrt{c}} \tag{3-1}$$

where K_{IC} is the fracture toughness under Mode I cleavage.

c is the maximum flaw size controlling fracture initiation.

A is a proportionality constant which depends upon the shape, depth, and location of a flaw as well as the type of testing.

Microscopic investigation of deposits on this program continue to reveal areal defects on lateral grain boundaries whose size (largest dimension) varies from 50 to 150 microns. If one substitutes in Equation 3-1 a typical identation fracture toughness of 3.2 MN $m^{-1.5}$, an average flexure strength of around 233 MN m^{-2}, and a proportionality constant of 0.74 (applicable to semicircular surface flaws under a bending mode - Ref. 45), Griffith flaws on the order of ≈100 microns are predicted in good agreement with the results of microscopic investigations conducted on this and earlier programs. It has been also observed that the density and size of these defects increase with distance from the first deposited layer. The origin of these defects has not been resolved but their presence explains the relatively low flexure strengths observed. Also the existence of a gradient in size and density of these defects within a deposit (which in turn is related to the size of the columnar grain . . . being smallest in the first

deposited region) clearly explains the higher strengths observed for flexure specimens oriented such that the tensile surface coincides with the first deposited material. (Ref. 1).

It is clear that future strength improvements rests with elimination of these grain boundary defects possibly through the use of soluble dopants to favorably alter deposition morphologies. It is not insignificant that a 150 percent increase in strength (compared to Phase 1 levels) has already been demonstrated utilizing Al as a dopant (Spec. 18-1-P, $\bar{\sigma}_{AV}$ = 317 MN m^{-2}). Complete elimination of remaining grain boundary defects should result in dramatic increases in CVD α-Si_3N_4 strength.

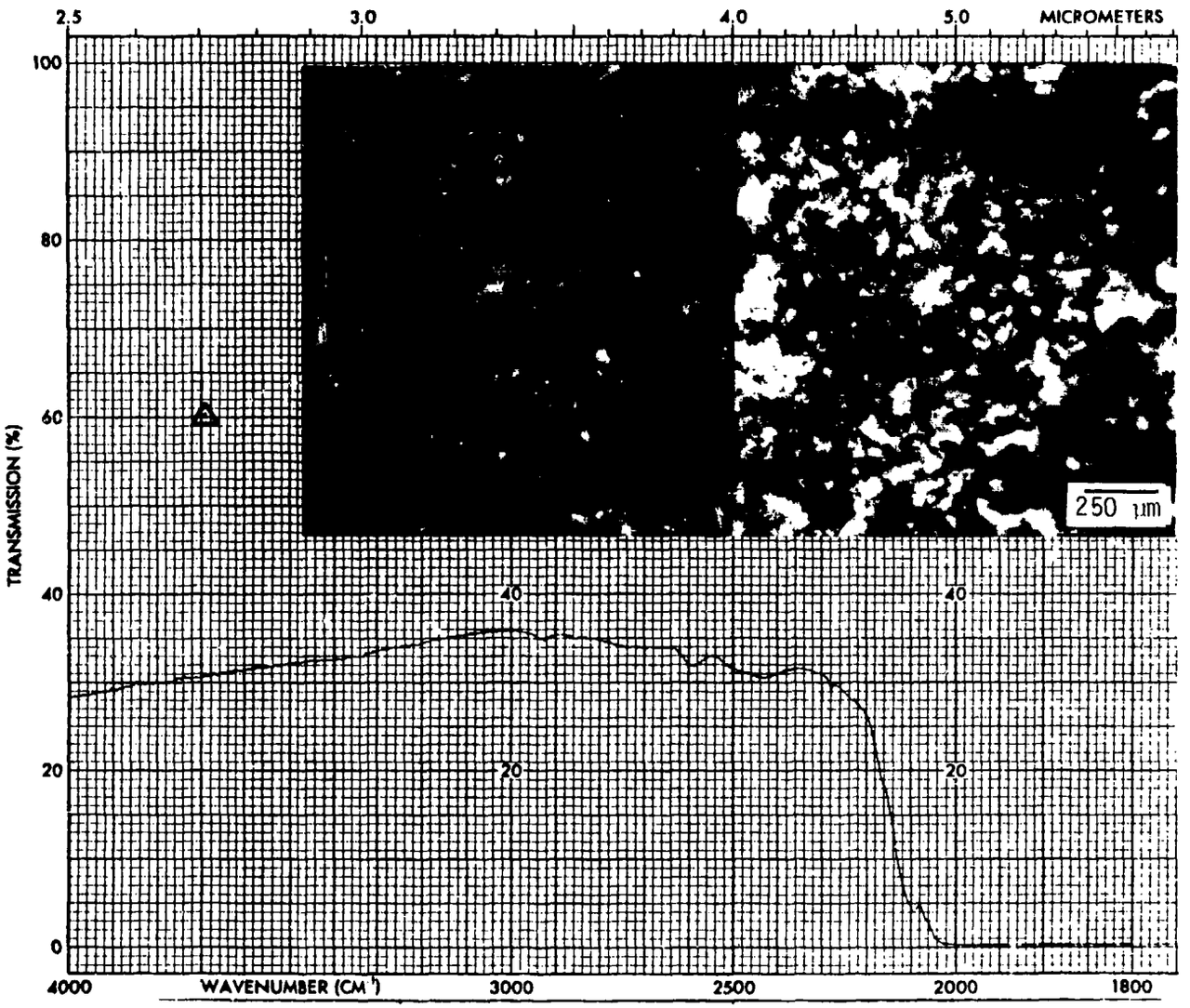

Figure 3-1. Specular and Discrete Hemispherical Transmittance of Lapped and Polished CVD α-Si_3N_4 Dome (Run No. 400-391). Finished Wall Thickness = 1.09 mm. Also Shown Are Stereo Pairs Illustrating Microstructure as Viewed With Light Incident on First Deposited Surface in Stagnation Region of Dome.

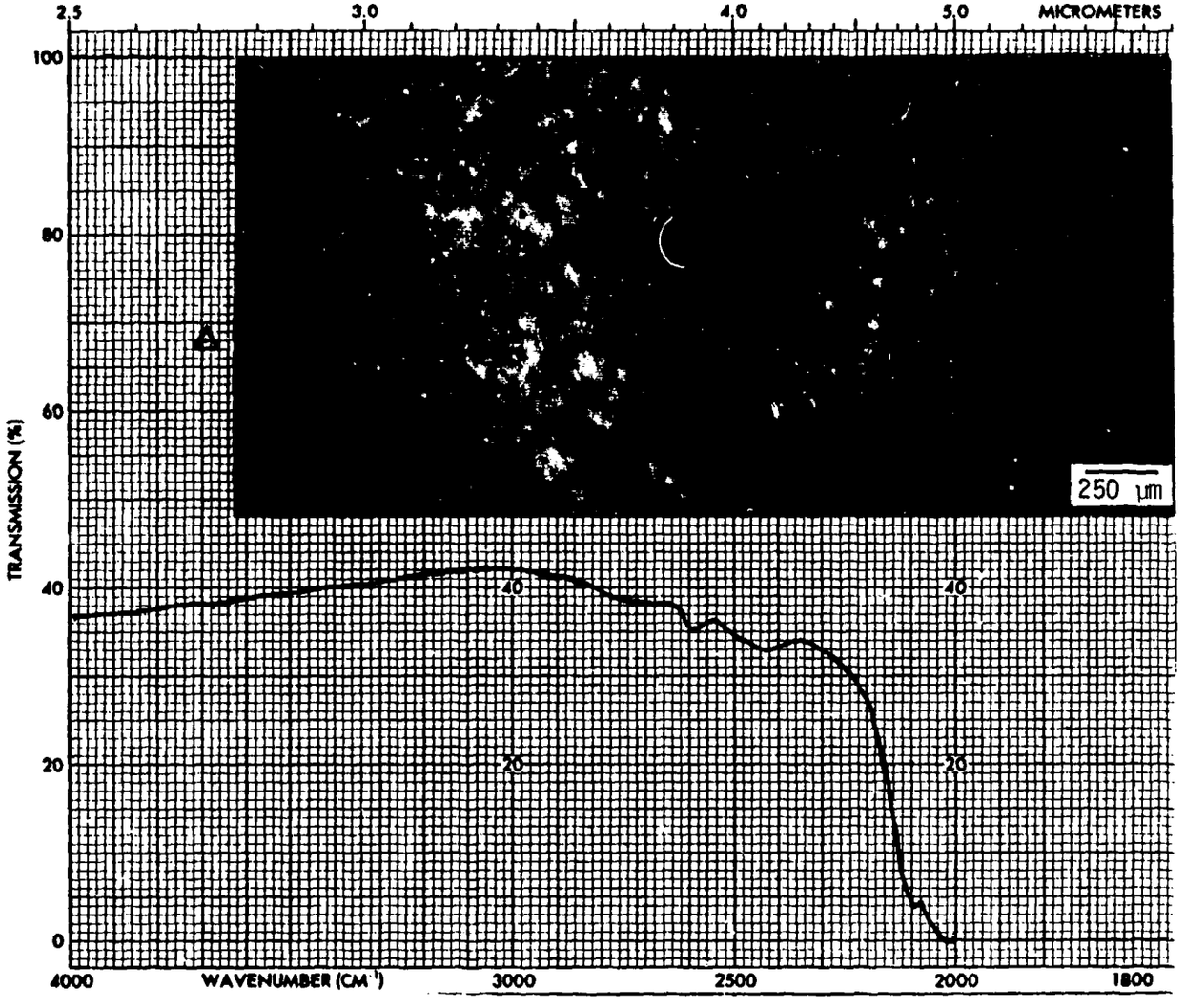

Figure 3-2. Specular and Discrete Hemispherical Transmittance of Lapped and Polished CVD α-Si_3N_4 Dome (Run No. 400-393). Finished Wall Thickness = 1.40 mm. Also Shown Are Stereo Pairs Illustrating Microstructure as Viewed With Light Incident on First Deposited Surface in Stagnation Region of Dome.

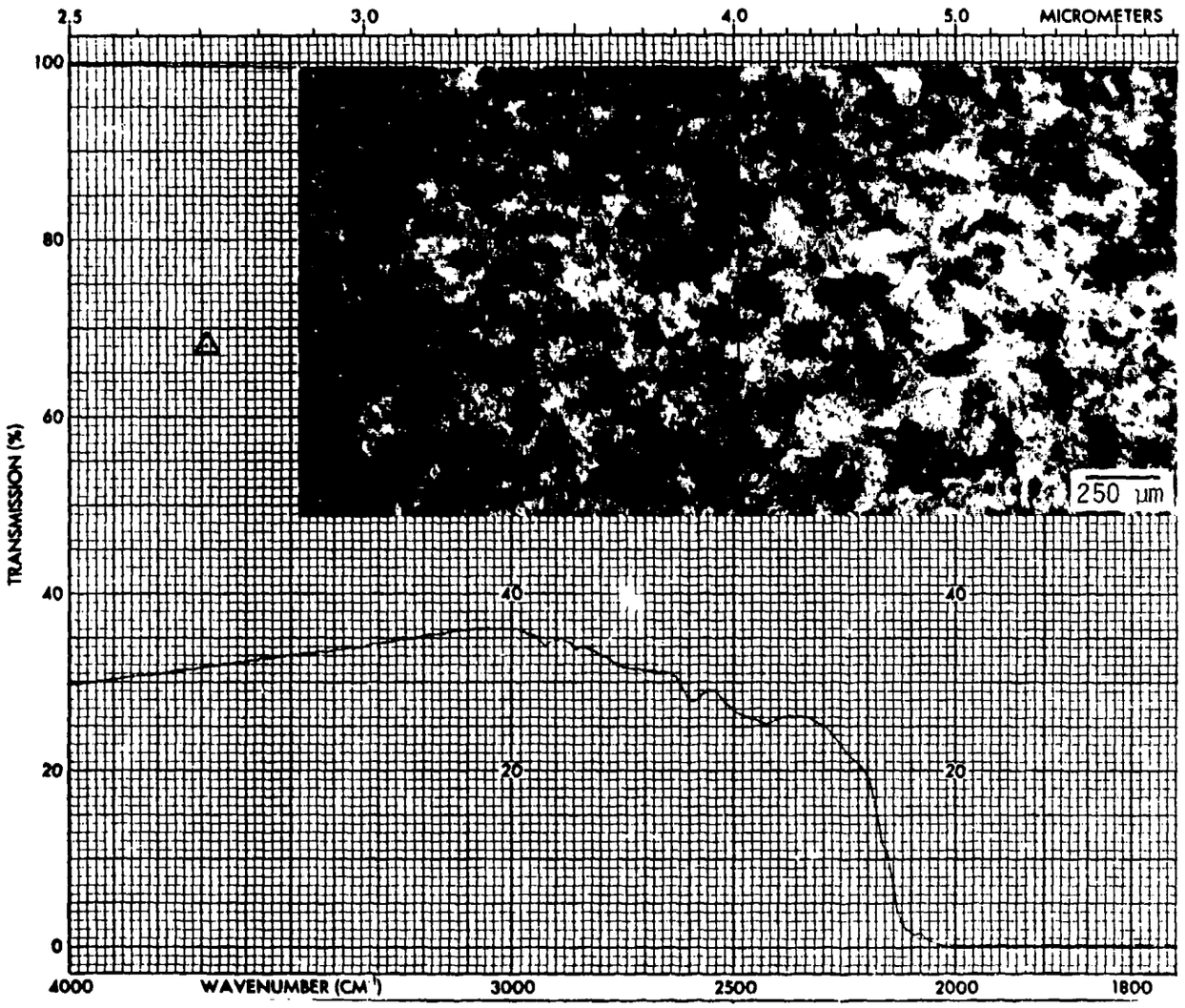

Figure 3-3. Specular and Discrete Hemispherical Transmittance of Lapped and Polished CVD α-Si_3N_4 Dome (Run No. 400-394). Finished Wall Thickness = 1.58 mm. Also Shown Are Stereo Pairs Illustrating Microstructure as Viewed With Light Incident on First Deposited Surface in Stagnation Region of Dome.

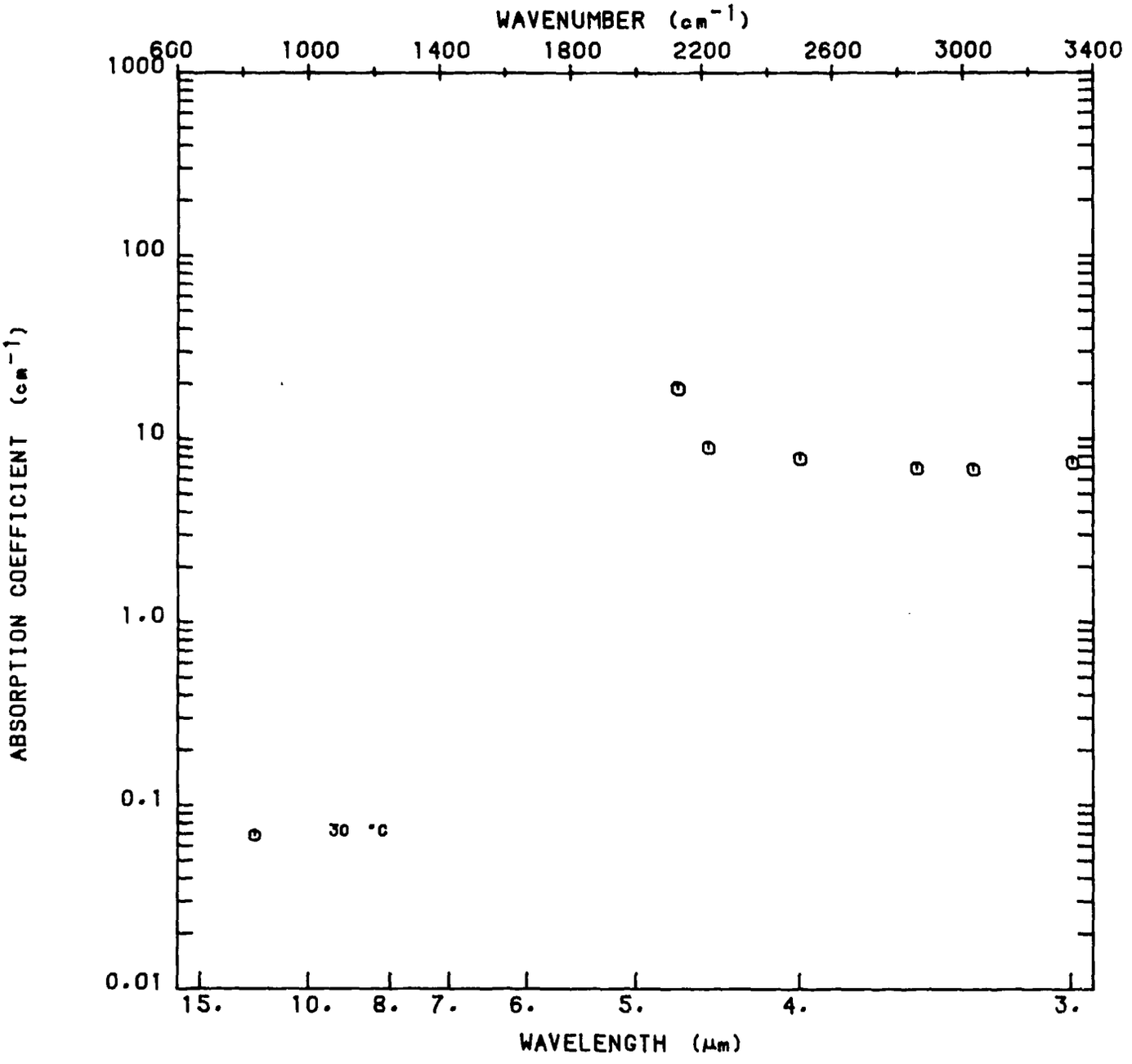

Figure 3-4. Absorption Coefficient of CVD αSi_3N_4 Dome (Run No. 400-391) as Function of Wavelength.

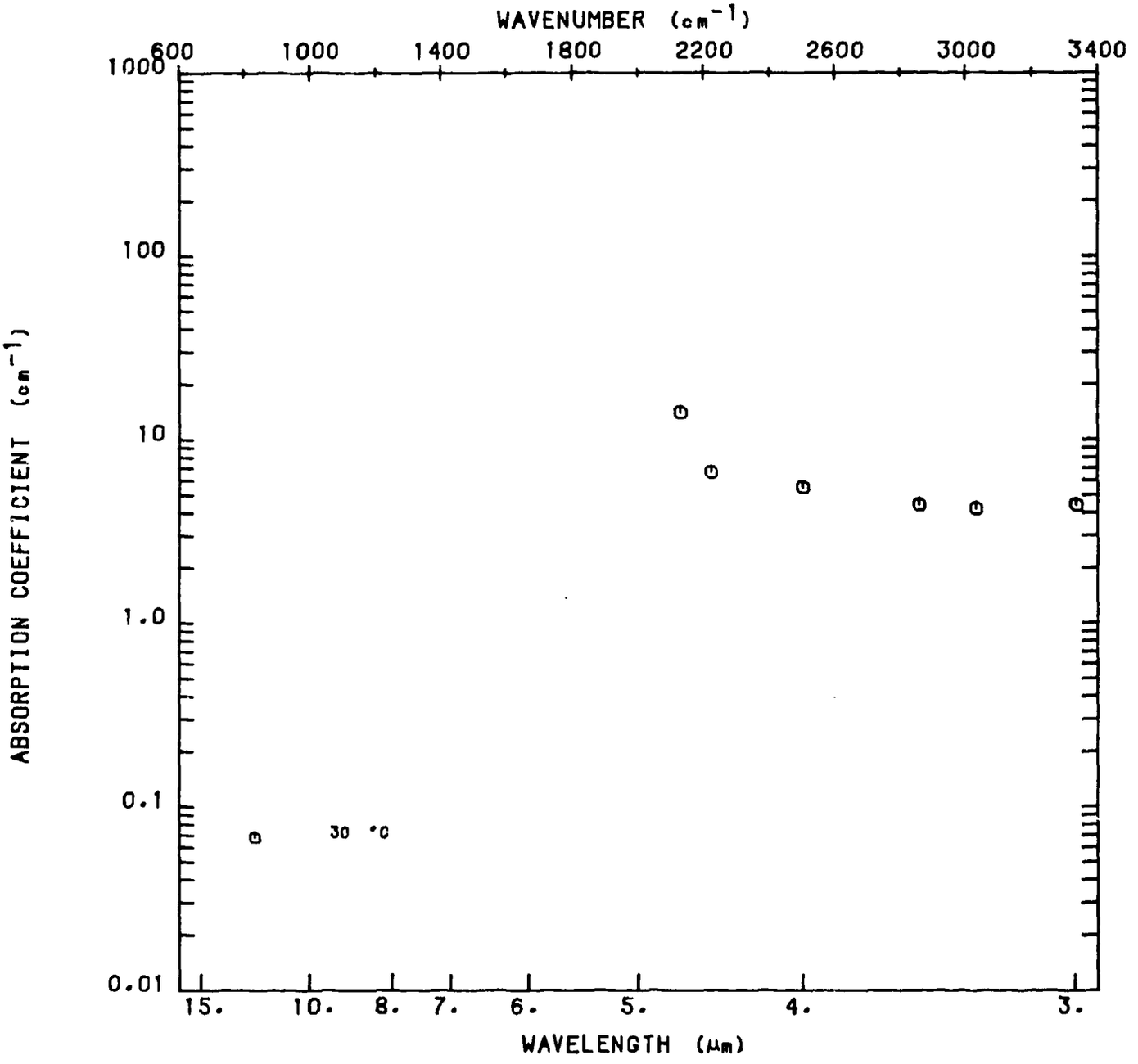

Figure 3-5. Absorption Coefficient of CVD αSi_3N_4 Dome (Run No. 400-393) as Function of Wavelength.

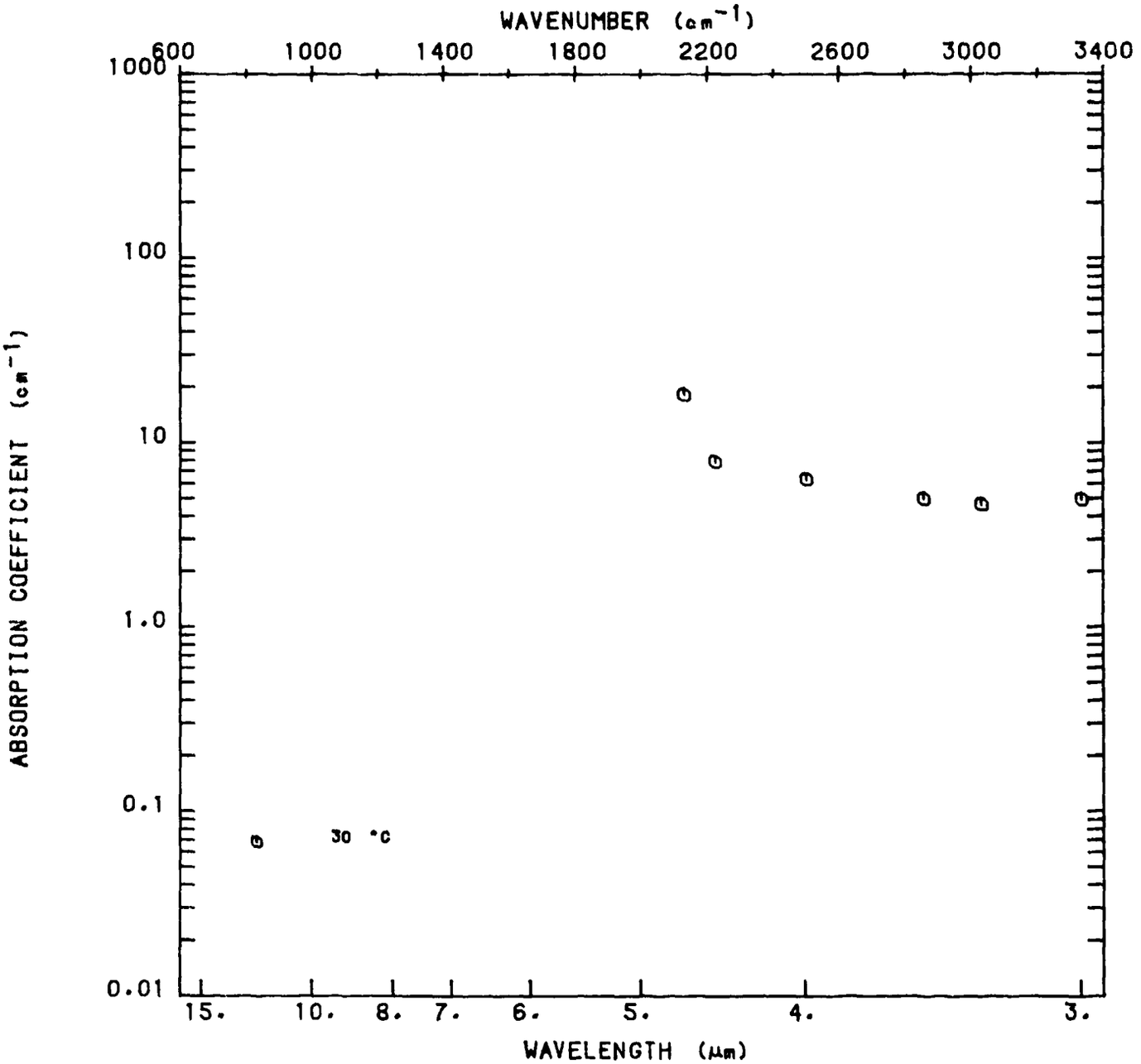

Figure 3-6. Absorption Coefficient of CVD αSi_3N_4 Dome (Run No. 400-394) as Function of Wavelength.

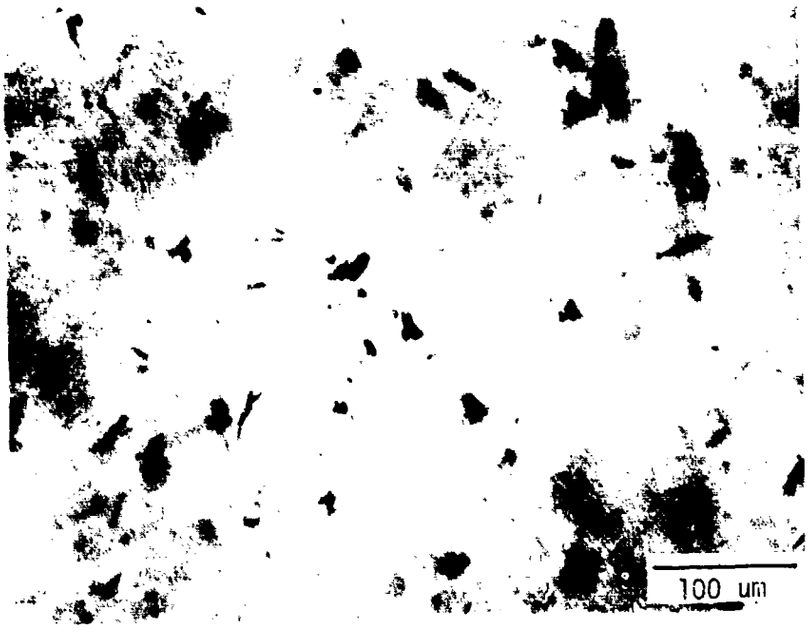

CVD α-Si_3N_4 (Run No. 400-394)

λ	$\alpha(cm^{-1})$	
μm	Specular	Total
2.50	5.71	-
2.71	5.01	1.09
3.00	4.92	-
3.50	4.92	-
4.00	6.32	-
4.50	7.87	-

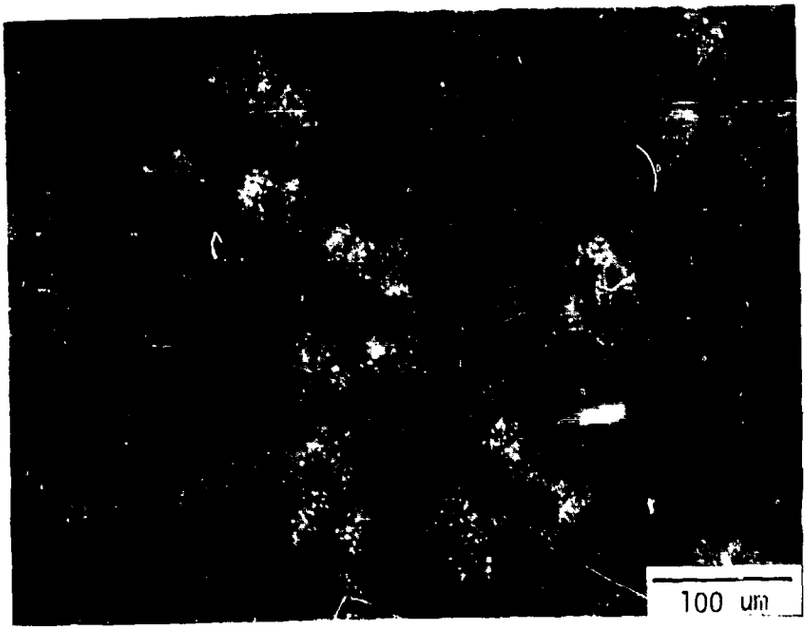

CVD α-Si_3N_4 (Run No. 400-391)

λ	$\alpha(cm^{-1})$	
μm	Specular	Total
2.50	8.74	-
2.71	8.02	2.54
3.00	7.35	-
3.50	6.86	-
4.00	7.75	-
4.50	8.90	-

Figure 3-7. Comparison of Microstructures of CVD α-Si_3N_4 Domes Exhibiting the Largest Differences in Computed Absorption Coefficients in the 2.5 to 4.7 m Wavelength Region.

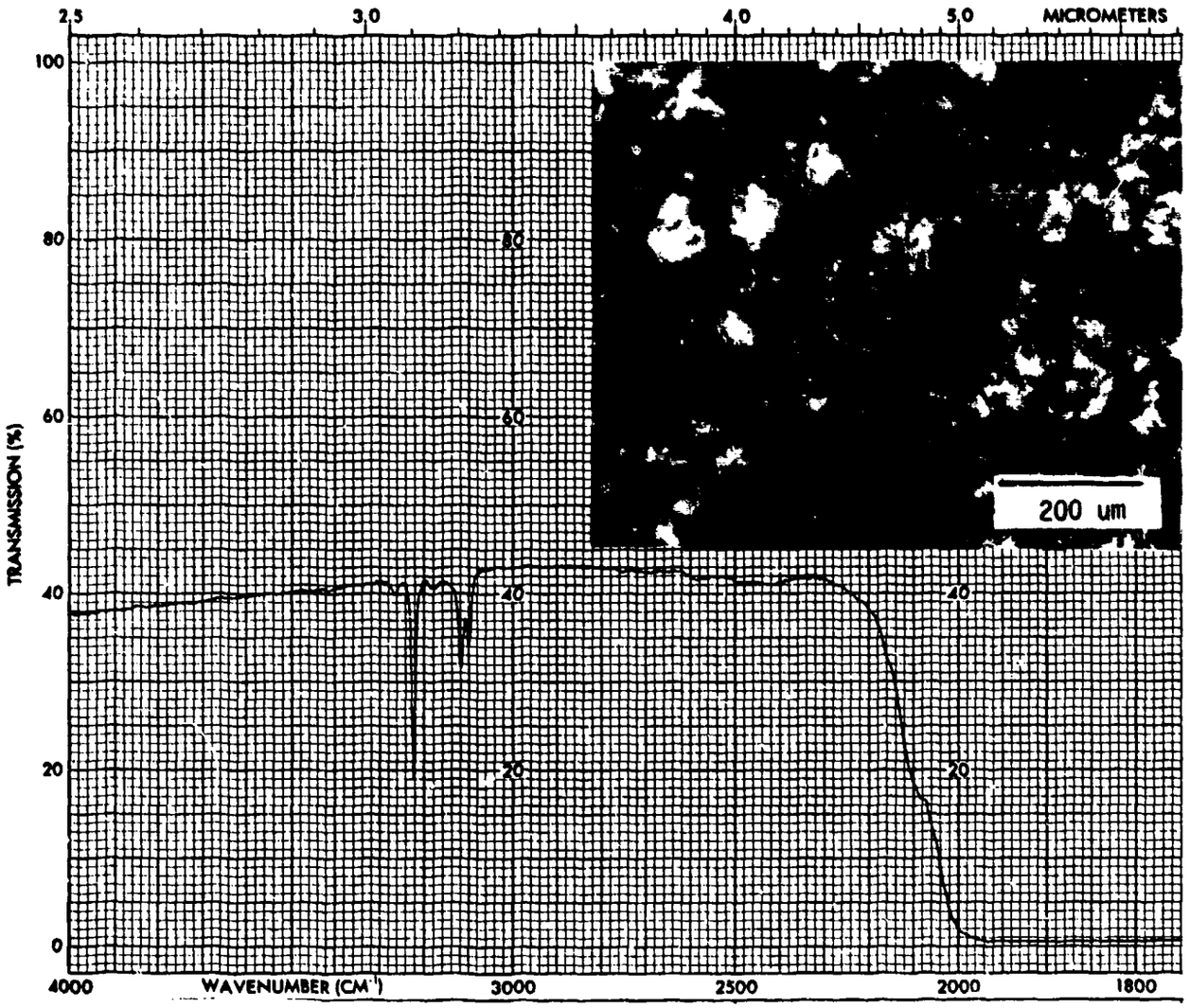

Figure 3-8. Specular Transmittance of Al Doped α-Si_3N_4 as a Function of Wavelength (Spec. No. HW-18U). Specimen Thickness = 0.483 mm.

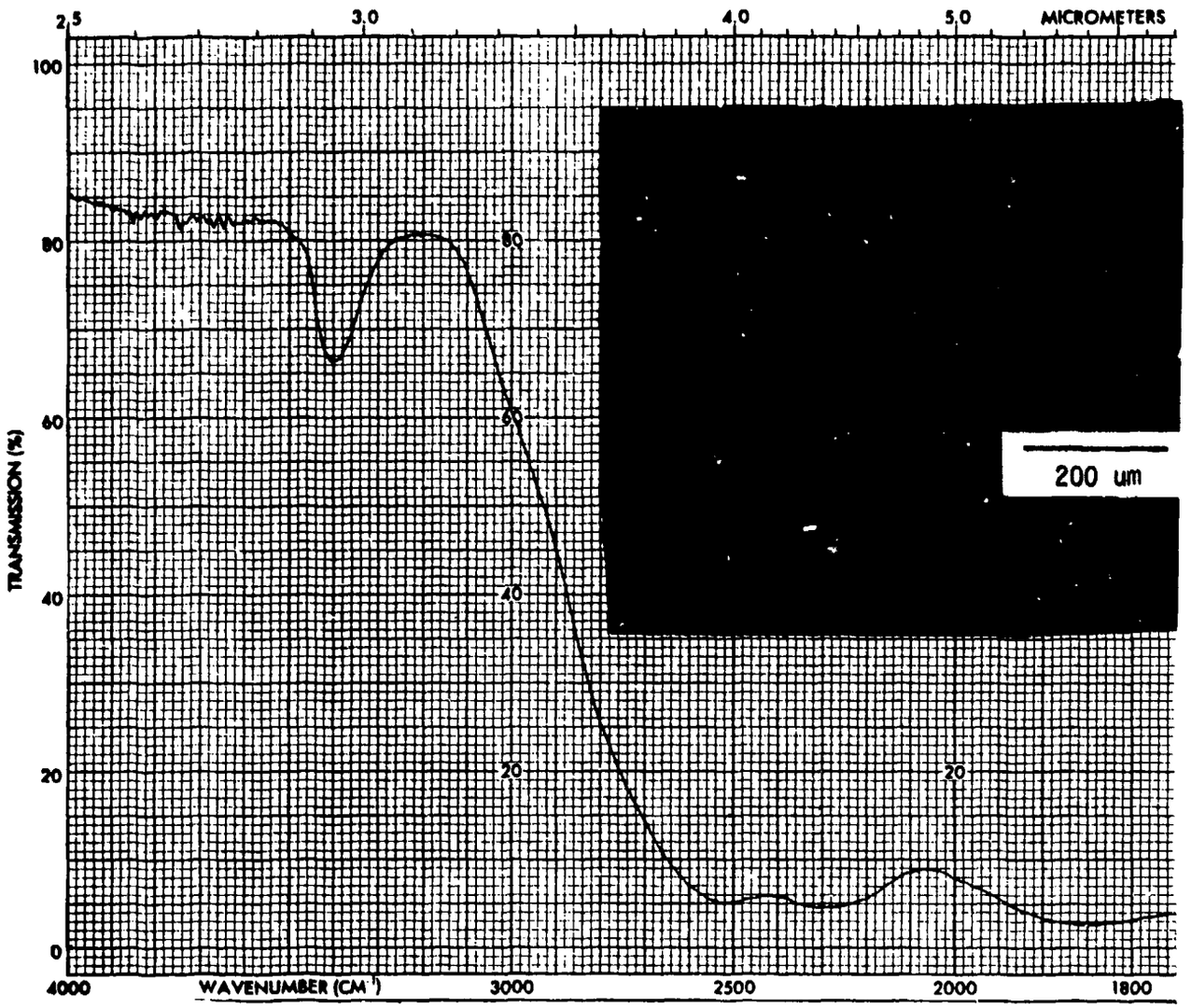

Figure 3-9. Specular Transmittance of Amorphous BN Doped With Si (Spec. No. HW-6). Specimen Thickness = 0.191 mm.

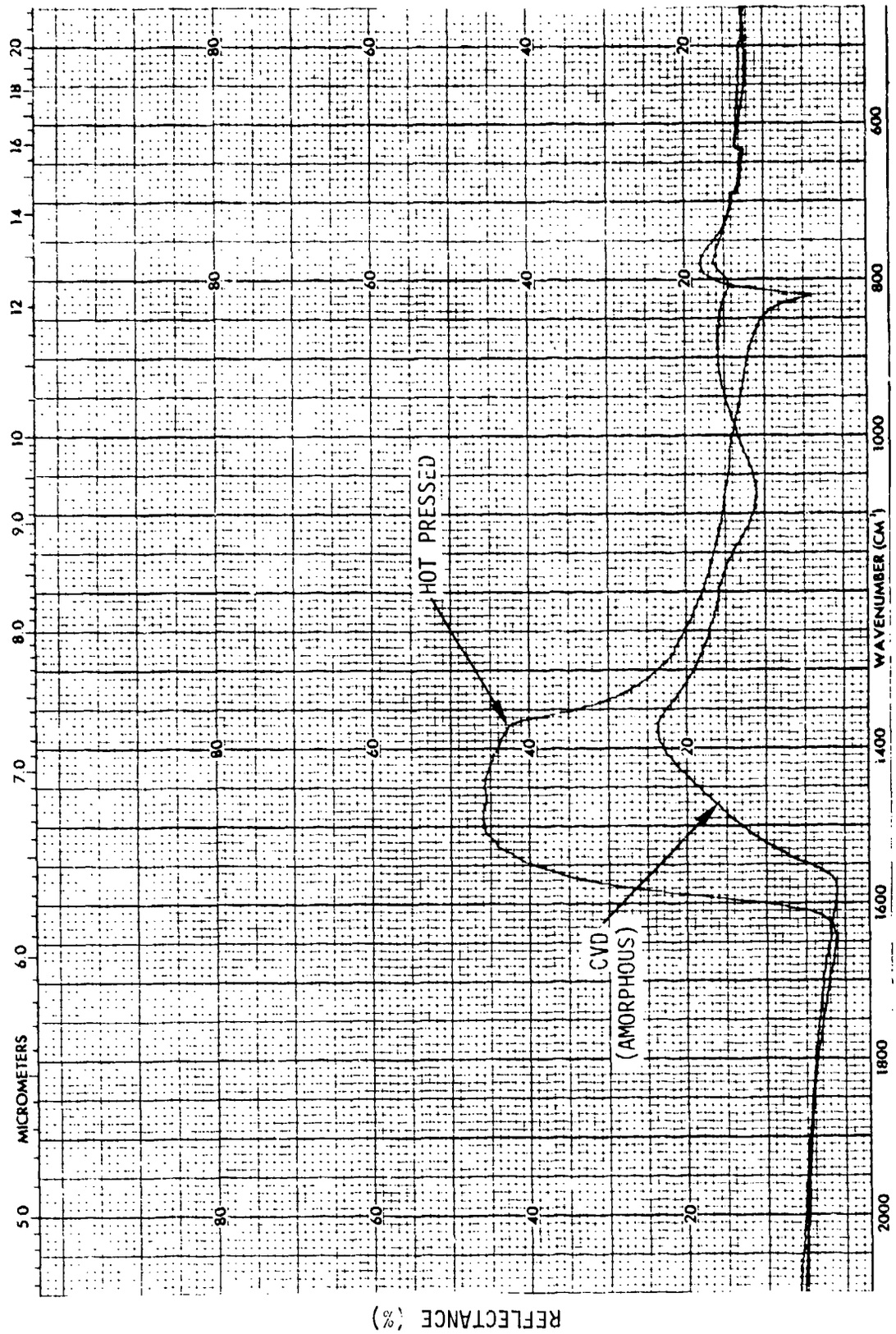

Figure 3-10. Comparison of Specular Reflectance of Hot Pressed, Hexagon BN (Upper Curve) With Amorphous BN Doped With Si (Spec. No. HW-6).

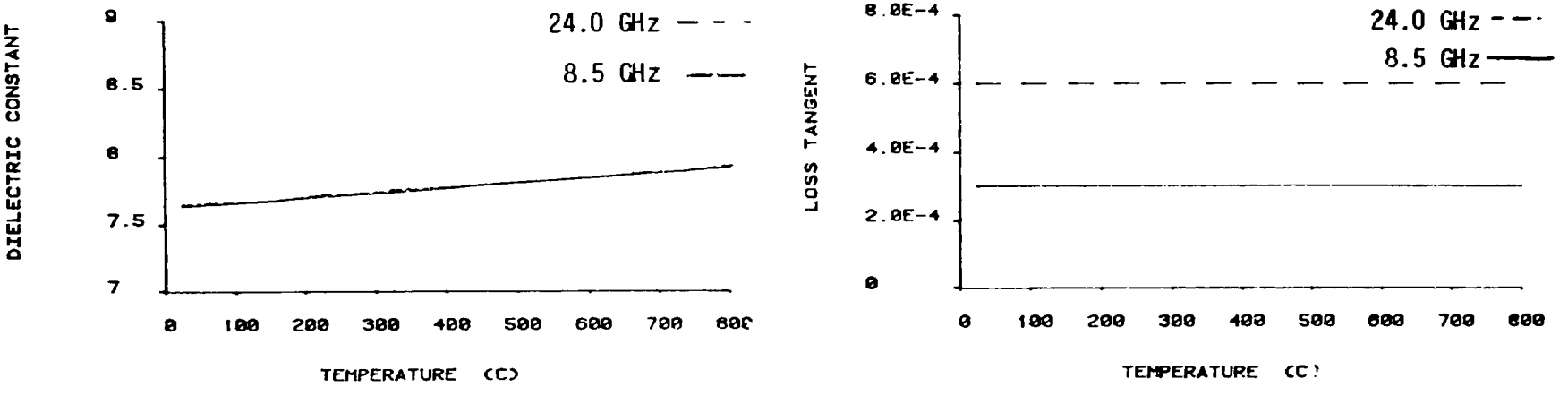

Figure 3-11. Dielectric Properties of CVD α-Si_3N_4 As a Function of Temperature and Frequency (Ref. 42).

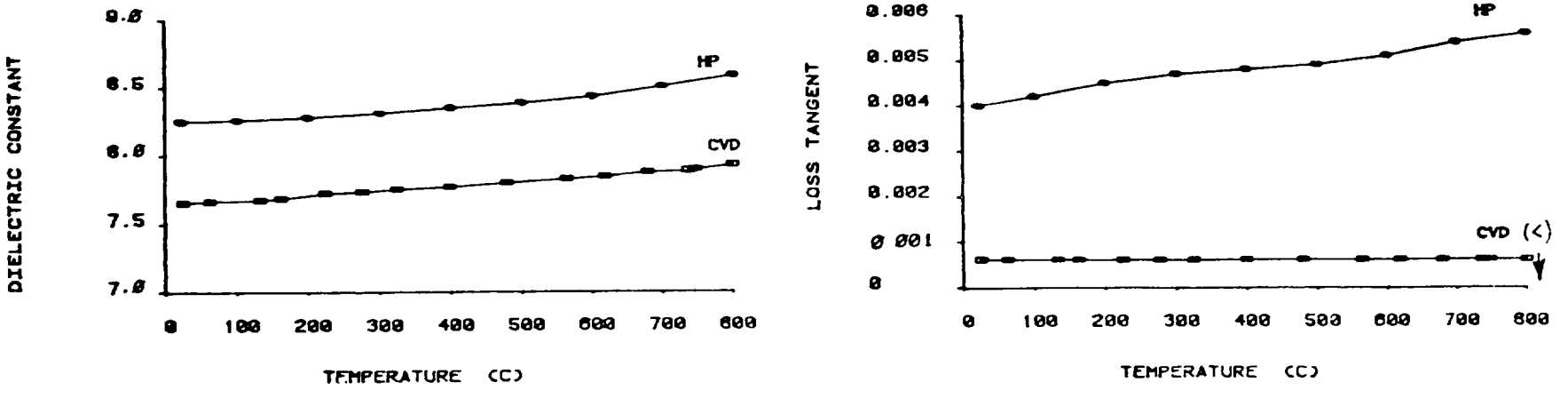

Figure 3-12. Comparison Of Dielectric Properties of CVD Versus HP Silicon Nitride at 24 GHz (Ref. 42).

SECTION 4.0
PROGRAM SUMMARY

SECTION 4.0

PROGRAM SUMMARY

In two previous annual reports (Refs. 1, 38) the results of processing research and property characterization on CVD Si_3N_4 have been documented. In these programs the deposition kinetics of Si_3N_4 were explored with a variety of furnace designs and silicon: nitrogen precursors including variations in the usual thermodynamic variables of pressure, temperature, flow rate and reactant concentrations. The feasibility of preparing free standing plate and hemispherical domes was demonstrated using different sources of Si, viz., $SiCl_4$ or SiF_4 in a hot wall reactor. The former reactant provided the highest deposition rate and conversion, however, there was a tendency to produce nodular last deposited surfaces which were difficult (if not impossible) to finish to required irdome or radome quality. On the other hand, the SiF_4 reactant, while having a significantly lower deposition rate, generally produced relatively-smooth, fine-grained last deposited surfaces requiring minimal material removal to achieve good optical-quality surface finishes.

On the current Phase 3 program processing conditions were further refined for the SiF_4 system enabling hemispherical domes to be prepared with transmittance levels significantly higher than that obtained during the Phase 1 Program. As part of this effort, finishing techniques were developed using conventional diamond tooling to achieve optical-quality surface finishes.

Processing research during Phase 2 and 3 also included the use of a cold wall reactor which produced deposits with unexpected similarities to those obtained in the hot wall reactor. Initial codeposition studies were conducted in the cold wall reactor, however, the limited areal extent of the deposits coupled with the desire to scale-up one process prior to program conclusion resulted in abandonment of this effort about the midpoint of the Phase 3 effort.

During the course of the Phase 3 program a deposition model has evolved which explains many of the deposition phenomena observed during the study. Further testing of the model will be invaluable in any future process and/or property optimization programs.

Physical property characterizations of a wide range of deposits have established the CVD form of silicon nitride as a candidate electromagnetic window material for advanced, high-performance tactical missile systems. While still requiring

optimization, the current CVD modification is projected to ultimately possess the following attributes:

a. Multiple transmittance band passes and minimal temperature sensitivity of associated properties.

b. Increased thresholds for impact damage and erosion.

c. Improved resistance to the development of thermal stress.

d. Increased refractoriness and strength retention at high temperature.

At the current state of process development (which is by no means final), the strength of CVD α-Si_3N_4 has been found to be comparable to RSSN exhibiting similar strength retention properties at elevated temperatures. Fractographic analyses when coupled with the brittle fracture theory of Griffith have identified extrinsic flaw morphologies in grain boundaries which are responsible for the current strength plateau associated with CVD α-Si_3N_4. It is clear that future strength improvements rest with elimination of these grain boundary defects possibly through the use of soluble dopants to favorably alter deposition morphologies. It is not insignificant that a 150 percent increase in strength (compared to Phase 1 levels) was recorded using Al as a dopant. Complete elimination of remaining grain boundary defects should result in dramatic increases in the strength and also in the specular transmittance behavior in the visible and infrared portions of the electromagnetic spectrum. It is noteworthy that improved visible and infrared specular transmittance levels observed during the Phase 3 program correlated with a reduction in the density of grain boundary microcracks. The achievement of a finer columnar growth habit should minimize the density and size of crystal boundary microcracks since it is already known that a lower microcrack density of smaller flaw size exists in the finer-grained first deposited layer of current deposits. Also, long-time high-temperature annealing experiments could be fruitful in promoting microcrack healing through the mechanism of self-diffusion via volume, grain boundary and surface diffusion modes.

The reader is directed to the technical reports, publications and presentations listed in Table 4-1 for more detailed processing and property data on CVD Si_3N_4 generated on this program.

TABLE 4-1. INDEX OF DOCUMENTATION FOR CURRENT PROGRAM

A. INDEX OF TECHNICAL REPORTS

1. R. A. Tanzilli, J. J. Gebhardt, J. O. Hanson, "Chemical Vapor Deposition of Silicon Nitride", GE-RSD Document Number 77SDR2257, September 1977. (ONR Contract No. N00014-76-C-0547).

2. R. A. Tanzilli et. al., "Processing Research on Chemically Vapor Deposited Silicon Nitride - Phase 2", GE-RSD Document Number 79SDR2324, December 1979 (ONR Contract No. N00014-78-C-0107).

3. R. A. Tanzilli, J. J. Gebhardt, J. D'Andrea, "Processing Research on Chemically Vapor Deposited Silicon Nitride - Phase 3", GE-RSD Document Number 81SDR2111, December 1981 (ONR Contract No. N00014-80-C-0575).

B. INDEX OF PUBLICATIONS AND PRESENTATIONS

1. R. A. Tanzilli, J. J. Gebhardt, J. O. Hanson, "Potential for Chemically Vapor Deposited Silicon Nitride as a Multimode Electromagnetic Window (VIS, IR, RF), Proceedings of the 14th Symposium on Electromagnetic Windows, Georgia Institute of Technology, Atlanta, GA, June 21-23, 1978.

2. R. A. Tanzilli and J. J. Gebhardt, "CVD α-Si_3N_4 and CVD β-SiC as Potential Tactical Sensor Window Materials", presented at the February 1981 Review of Advanced Materials for Tactical Missile Window Enclosures, Office of Naval Research, Arlington, VA.

3. R. A. Tanzilli and S. Musikant, "Electromagnetic (Optical, IR and Microwave) and Other Properties of Thermal Shock Resistant Ceramic Window Materials", presented at the 1981 IRIS Symposium, Specialty Group on Infrared Materials, Orlando, FL, May 1981.

4. R. A. Tanzilli and J. J. Gebhardt, "Optical Properties of CVD Silicon Nitride", Proceedings of the 25th Annual Meeting of the Society of Photo-Optical Instrumentation Engineers, San Diego, CA, August 1981.

SECTION 5.0
REFERENCES

SECTION 5.0

REFERENCES

1. R.A. Tanzilli et al., "Processing Research on CVD Silicon Nitride" - Phase 2", GE-RSD Doc. No. 79SDR2324, December 1979.

2. R. A. Holzl, Chemetal Corp., Pacoima, CA 91331, Summary Report, Contract N00019-77-C-0395, July 1979.

3. D. G. Bhat, San Fernando Labs, Pacoima, CA 91331, Summary Report, Contract N00019-78-C-0553, October 1980.

4. P.E.D. Morgan, J. Mat. Science 15 791-793 (1980).

5. F. F. Lange, J. Am Ceram Soc. 56 445-450 (1973).

6. K. Niihara and T. Hirai, J. Mat. Sci. 11 593-603, 604-611, 1233-52.

7. T. Hirai, N. Niihara, S. Hayashi and T. Goto, Sci. Rep. Res. Inst. Tohoku Univ. Ser A. 26 185-201 (1979).

8. A. C. Airey, S. Clarke and P. Popper, Proc. Brit. Ceram Soc. 22 305-320 (1973).

9. Galasso, F. S., Veltri, R. D., and Croft., W. J., Bull. Am. Ceram Soc. 57 453-454 (1978).

10. J. J. Gebhardt, R. A. Tanzilli and T. A. Harris, J. Electrochem Soc. 123 1578-82 (1976).

11. M. Billy, Ann. Chim. 1959 795-851.

12. O. Glemser and P. Naumann, Z. anorg. u. allgem. Chemie 298 134-141 (1958).

13. K. Kijima, K. Kato, Z. Inoue and H. Tanaka, J. Mat. Science, 10 362-3 (1975).

14. S. Wild., P. Grieveson and K. H. Jack, Special Ceramics, Vol. 5 Ed. P. Popper, 271-287, Brit. Ceram. Assn., Stoke-on-Trent (1972).

15. C. Greskovich and J. H. Rosolowski, J. Am. Ceram. Soc. 59 336-43 (1976).

16. D. B. Miller and H. H. Sisler, J. Am. Chem. Soc. 77 4998-5000 (1955).

17. M. Billy, Bull. Soc. Chim. France 1960 1653-54.

18. Lin, S.S. J. Electrochem Soc. 124 1945-1947 (1977).

19. Lin, S.S., ibid. 125 1877-1879 (1978).

20. B. J. Aylett, I. A. Ellis and C. J. Perritt, J. Chem Soc., Dalton Series 1956 pp 1953-1958.

21. K. Koizlik, J. Linke, H. Luhleich and H. Nickel., Thin Sol. Films 40, 115-121 (1977).

22. G. Fritz, J. Grobe and D. Kummer, Adv. Inorg. Chem. and Radiochemistry 7 349 (1965).

23. A. W. Laubengayer and O. T. Beachley, Jr., "Boron-Nitrogen Chemistry" Am. Chem. Soc. Adv. in Chem. Series 42 281-289 (1963).

24. R. Marchand, Rev. Chim. Miner., 1970 87-119.

25. W. P. Minnear, General Electric Co. TIS No. 81CRD069, April 1981, to be published Disc. of the Am. Ceram. Soc, Feb. 1982.

26. T. J. Whalen and A. T. Anderson, J. Am. Ceram. Soc., 58, 396-399 (1975).

27. B. R. Lawn and T. R. Wilshaw, "Fracture of Brittle Solids", Cambridge University Press, 1975, p. 115.

28. A. J. Moore, "Thermal Faceting", in Metal Surfaces, American Society for Metals, 1963, pp. 155-195.

29. W. R. Holman and F. J. Huegel, Proc. Conf. CVD of Refractory Metals. Am. Nucl. Soc., Hinsdale Ill, 1967 p. 127.

30. W. A. Bryant., J. Less Common Metals, 45 37-44 (1976).

31. R. L. Landingham and J. H. Austin, ibid 18 229 (1969).

32. W. Klemme and E. Tanke, Z fur anorg. u. allgem. Chemie 200 343-366 (1931).

33. von Th. Renner, Z fur anorg. u. allgem. Chemie 298 22-33 (1959).

34. W. C. Laughlin and N. W. Gregory, J. Chem. and Eng. Data 20 137-140 (1975).

35. J. R. Weiss and R. J. Diefendorf, Proc. Fourth Int. Conf. on CVD, pp. 488-497, Electrochem. Soc., Princeton, New Jersey, 1973.

36. U. Wannagat, Adv. in Inorg. Chem. and Radiochem., 6 225-279, 1964.

37. C. S. Hurlbut, Jr. and C. Klein, Manual of Mineralogy, J. Wiley & Sons, 1977, pp. 207-210.

38. J. Economy and R.V. Anderson, "Boron Nitride Fibers", J. of Polymer Science: Part C, No. 19, pp. 283-297 (1967).

39. R. A. Tanzilli et.al., "Chemical Vapor Deposition of Silicon Nitride-Phase 1", GE-RSD Doc. No. 77SDR2257, Sept. 1977.

40. R.A. Tanzilli et.al., "Potential for CVD Silicon Nitride as a Multimode EM Window (VIS, IR, RF)", Proceedings of the 14th Symposium on Electromagnetic Windows, Georgia Institute of Technology, Atlanta, Ga., June 1978.

41. J. P. Brazel et.al., "Millimeter Wave Hardened Antenna Window Materials Development", AMMRC TR 79-45, August 1979.

42. R. A. Tanzilli et.al., "Potential for Ultrahigh Purity Nitrides as High Performance Electromagnetic Windows", Proceedings of the 11th National SAMPE Technical Conference, Boston, Mass., Nov. 1979.

43. J. P. Brazel et.al., "Millimeter Wave Hardened Antenna Window Materials Development", AMMRC TR 81-45, Dec. 1981.

44. W.F. Knippenberg and G. Verspui, "The Influence of Impurities on the Growth of Silicon Carbide Crystals Grown by Gas-Phase Reactions", Mat. Res. Bull., Vol. 4, p. 5-43, 1969.

45. G. K. Bansal, "On Fracture Mirror Formation in Glass and Polycrystalline Ceramics", Phil. Mag., Vol. 35 (No. 4), 1977, p. 935.

APPENDIX A
MORPHOLOGY AND FRACTOGRAPHY OF COLD WALL REACTOR DEPOSITS

APPENDIX A

MORPHOLOGY AND FRACTOGRAPHY OF COLD WALL REACTOR DEPOSITS

The following SEM photomicrographs are examples of the range of morphologies and fracture patterns developed in deposits from the cold wall reactor experiments. Each photomicrograph lists the deposition sequence, flexure strength, and magnification. The upper surface of each fractograph represents the last deposited surface (LDS) region which was under tensile loading. Specific deposition parameters are given in Tables 2-1 and 2-2.

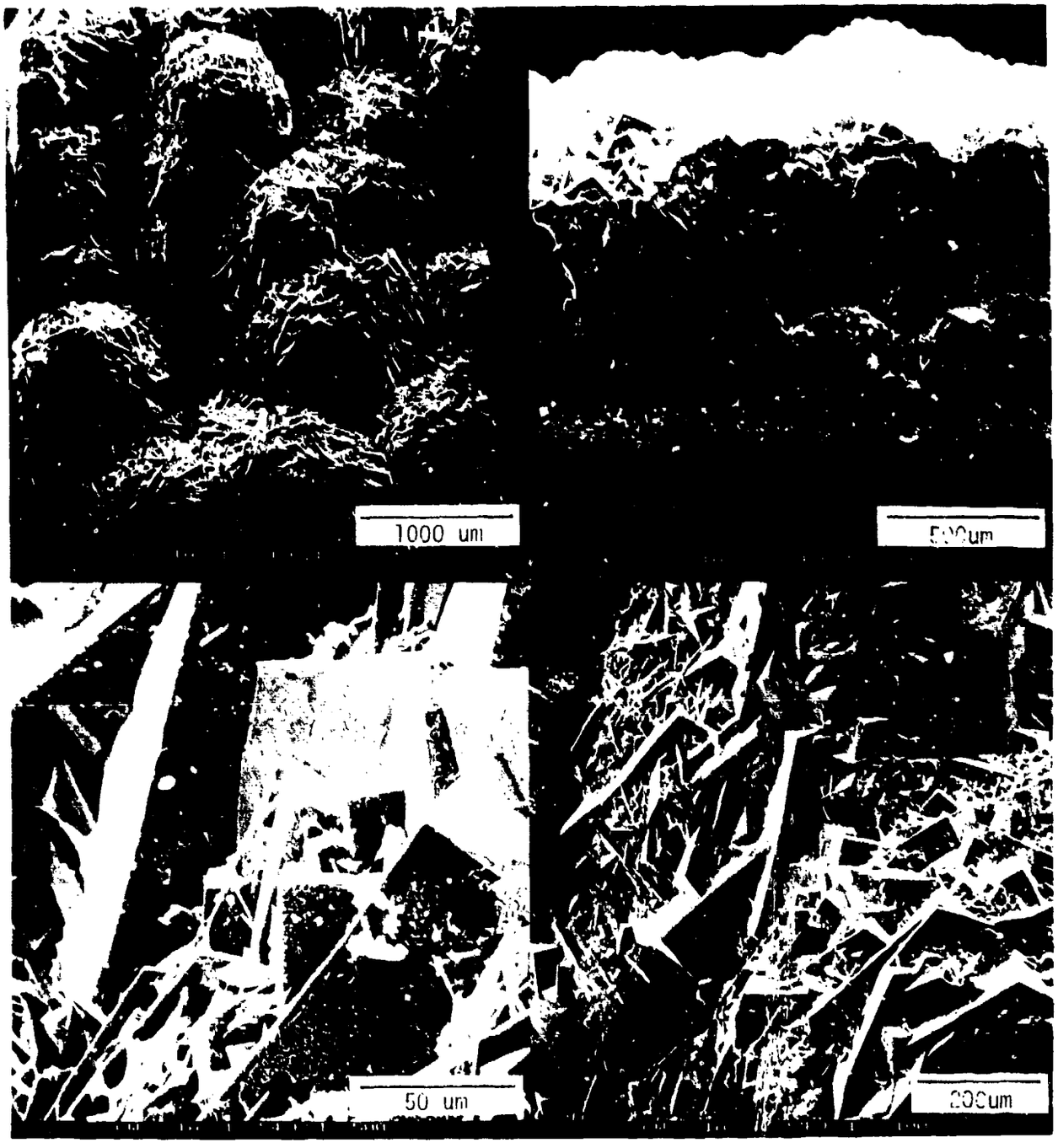

Figure A-1. SEM Photomicrographs of Last Deposited Surface (LDS) and Fractograph of Flexure Specimen (Upper Right) Showing Transgranular Cleavage Features. Evidence of Liquid Phase on LDS Shown in Lower Left Photomicrograph (Spec. No. CW-3-1A).

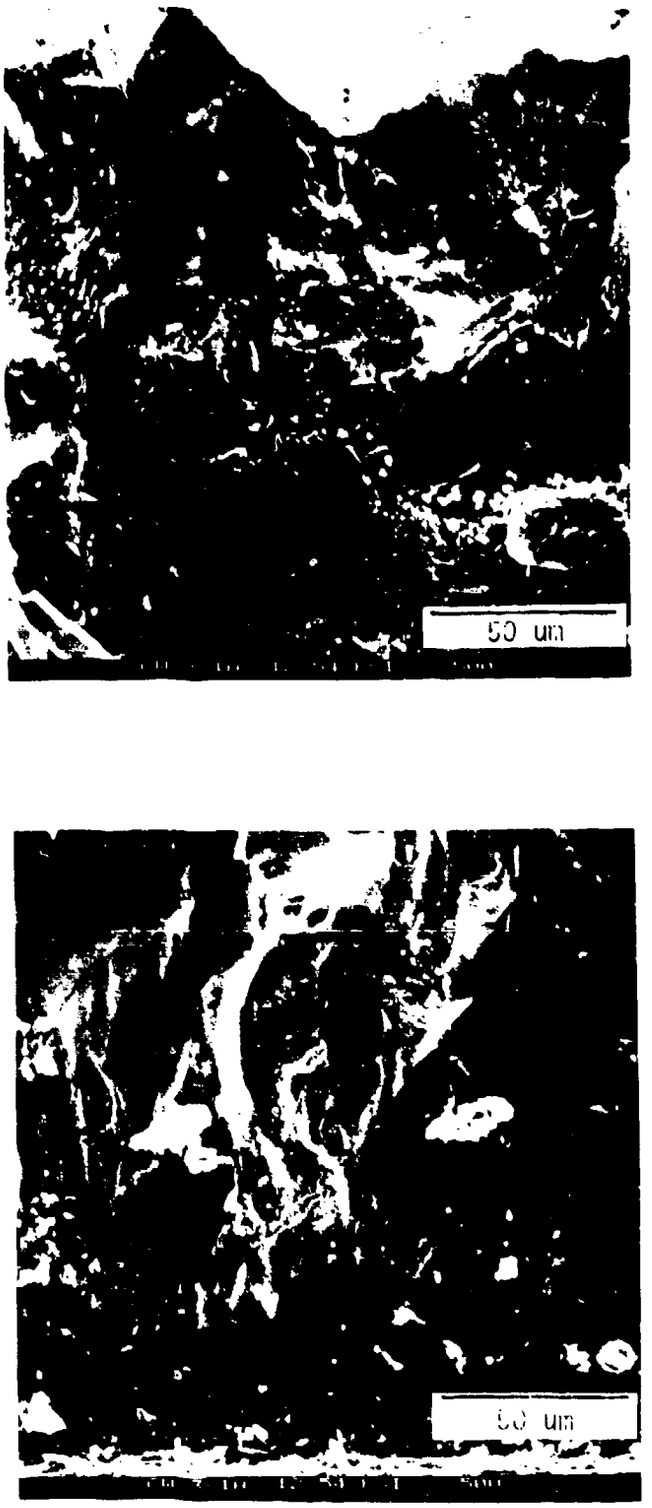

Figure A-2. SEM Fractographs of Flexure Specimen Showing Details of Transgranular Cleavage Features in Last (Upper) and First Deposited (Lower) Regions of Flexure Specimen (Spec. No. CW-3-1A).

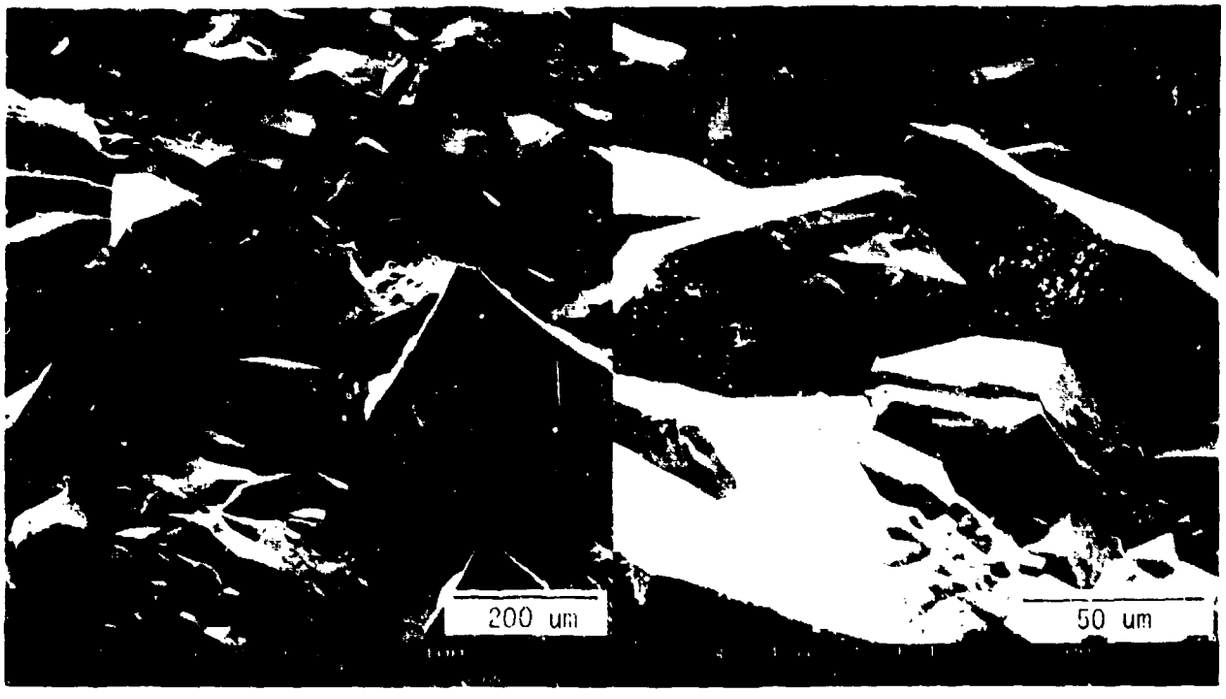

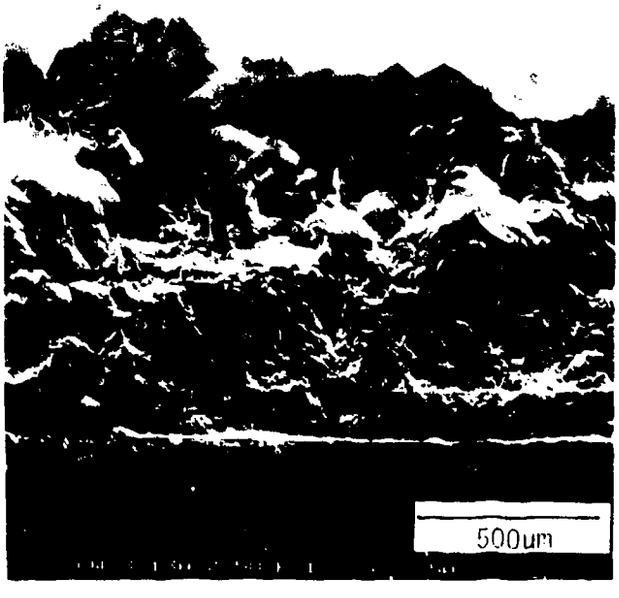

Figure A-3. SEM Photomicrographs of Last Deposited Surface (Upper) and Fractograph of Flexure Specimen (Lower) Showing Transgranular Cleavage Features (Spec. No. 3-13A).

Figure A-4. SEM Fractographs of Flexure Specimen Showing Additional Transgranular Cleavage Features (Spec. No. 3-13A).

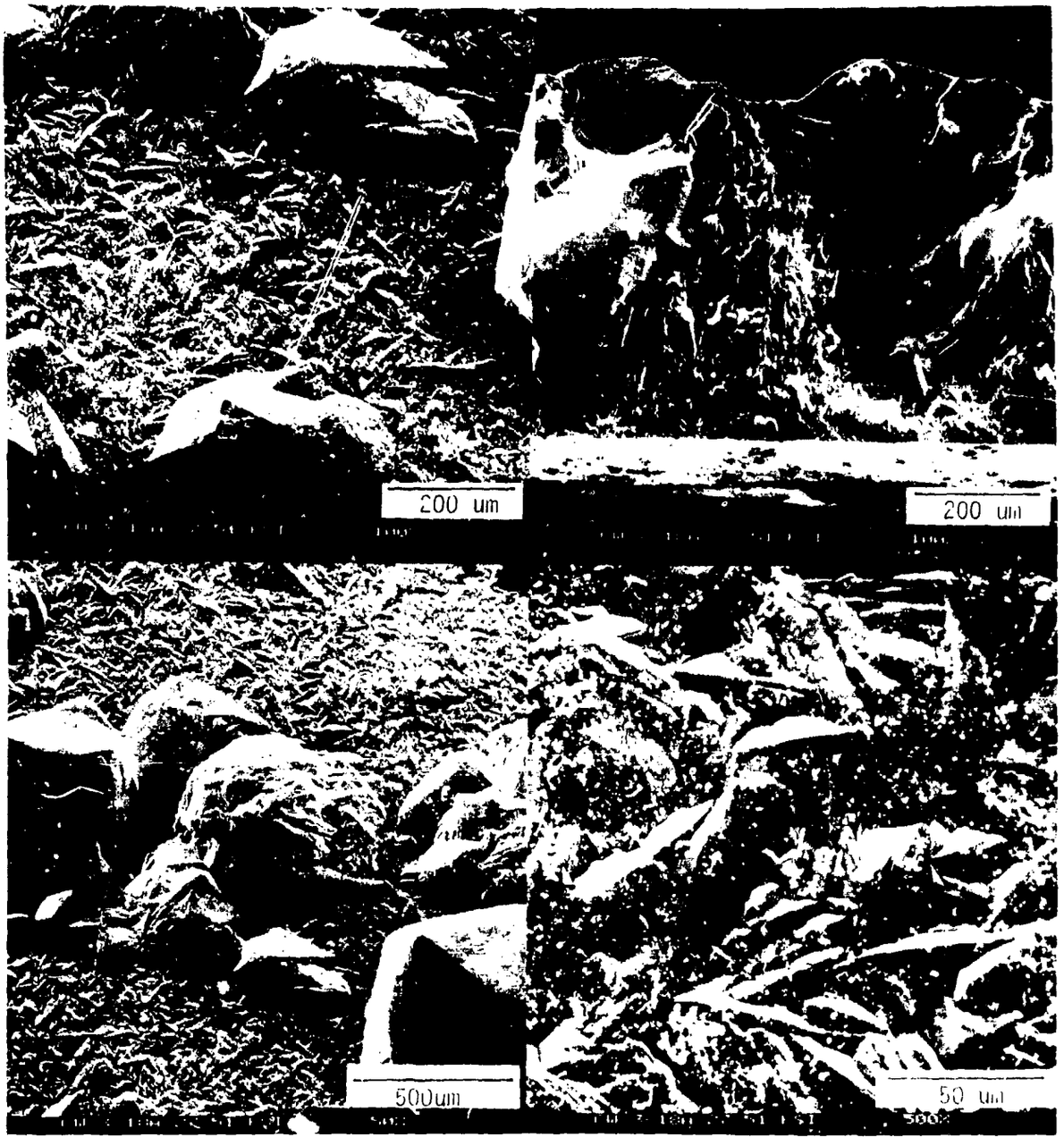

Figure A-5. SEM Photomicrographs of Last Deposited Surface (LDS) and Fractograph of Flexure Specimen (Upper Right). LDS Exhibits a Fine Grained Structure Together with Prominent Single Crystal Columnar Grains. Fracture Surface Shows Transgranular Cleavage Features Associated With Single Crystal Growth and a Finer-Scale Grain Structure (Spec. No. CW-3-18A).

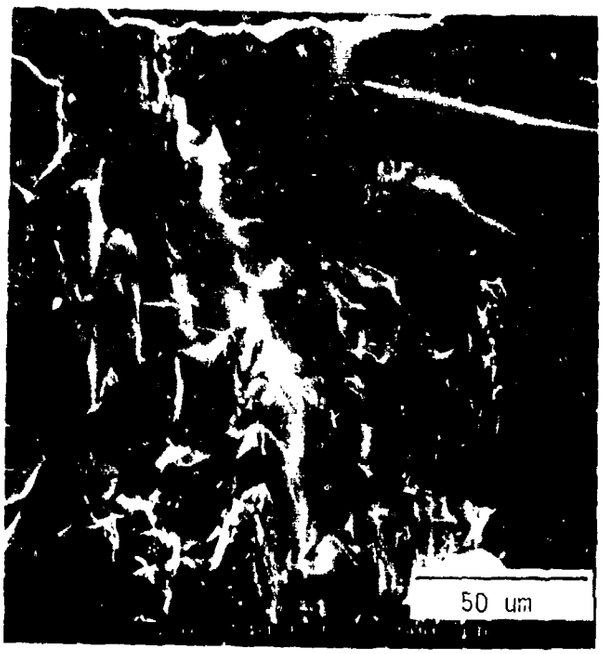

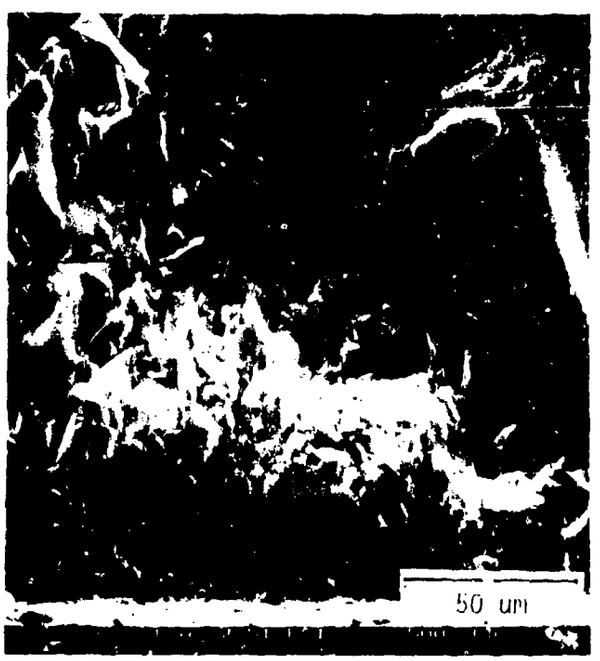

Figure A-6. SEM Fractographs of Flexure Specimen Showing Details of Transgranular Cleavage Features in Last (Upper) and First Deposited (Lower) Regions of Flexure Specimen (Spec. No. CW-3-18A).

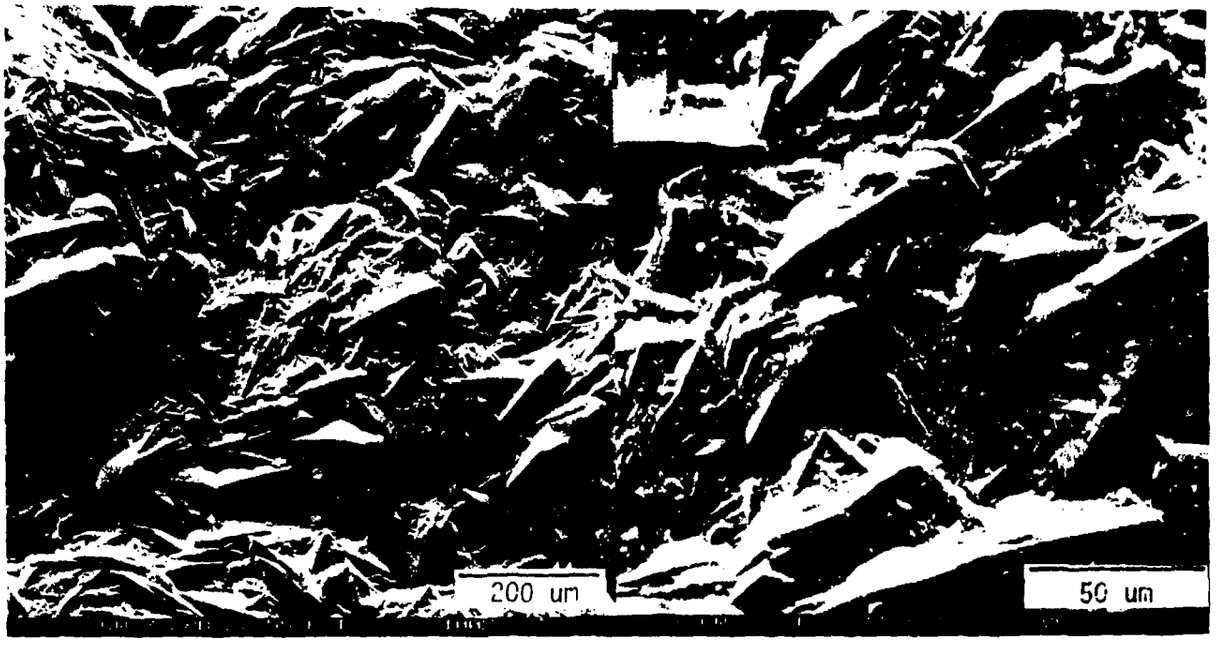

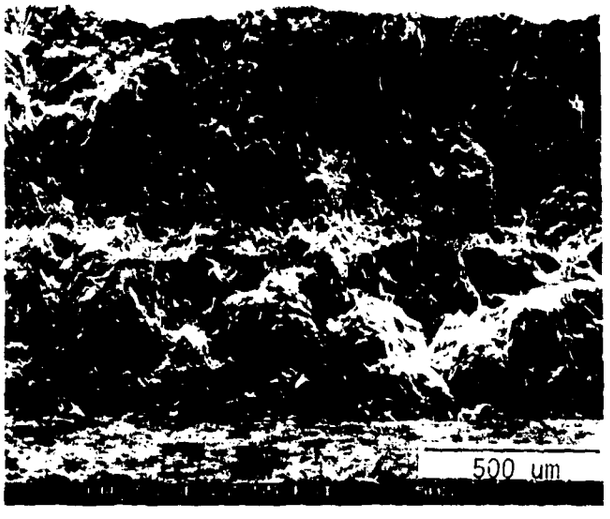

Figure A-7. SEM Photomicrographs of Last Deposited Surface (LDS) and Fractograph of Flexure Specimen Showing a Fine-Grained, Multifaceted Microstructure (See No. CW-3-28B).

Figure A-8. SEM Fractographs of Flexure Specimen Showing Details of Transgranular Cleavage Features in the Last (Upper) and First Deposited (Lower) Regions of Flexure Specimen (Spec. No. CW-3-283).

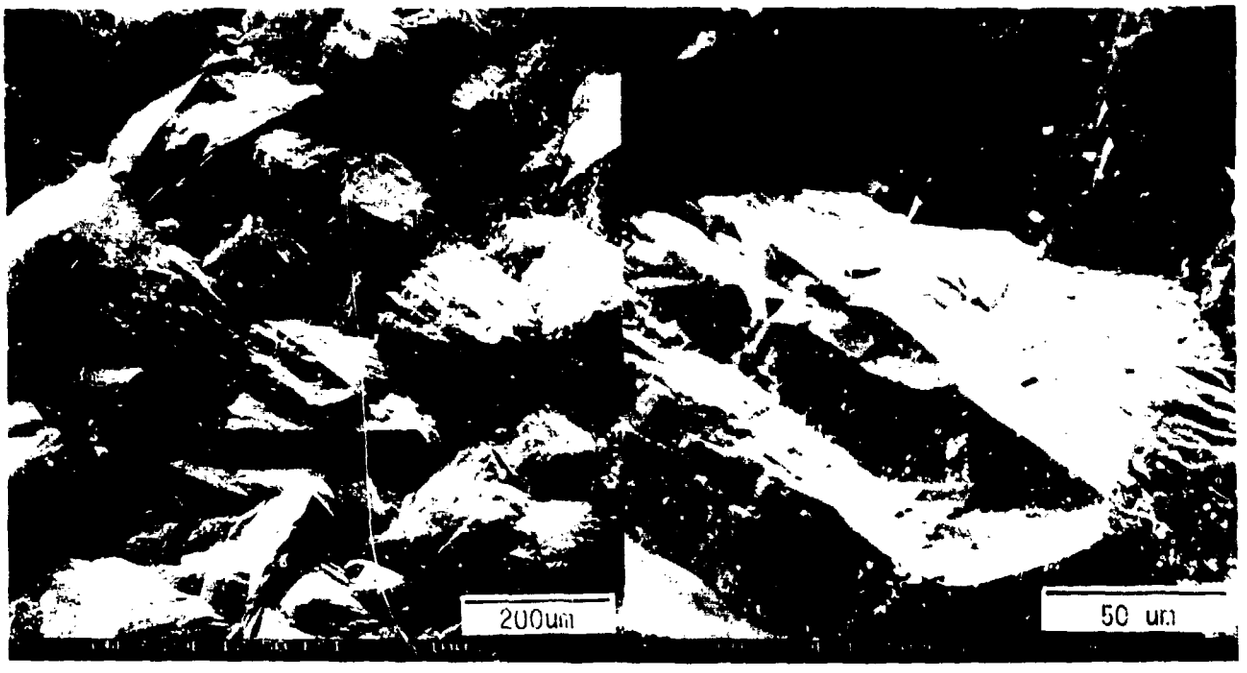

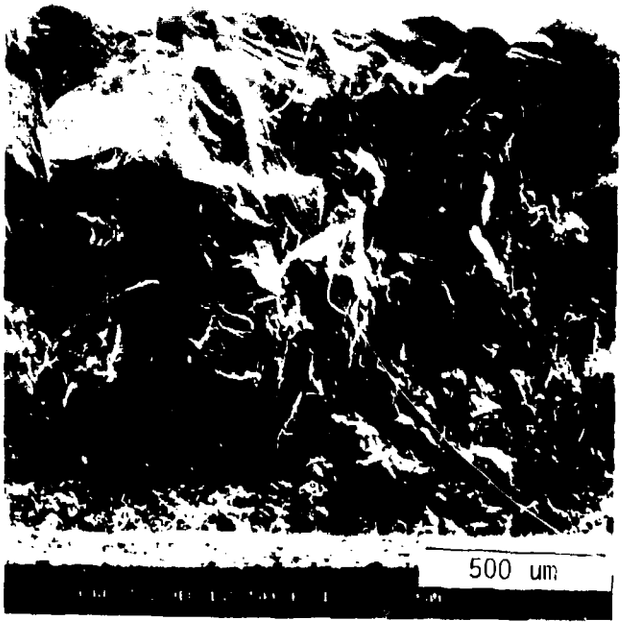

Figure A-9. SEM Photomicrographs of Last Deposited Surface (Upper) and Fractograph of Flexure Specimen (Lower) Showing Transgranular Cleavage Features (Spec. No. 3-29B).

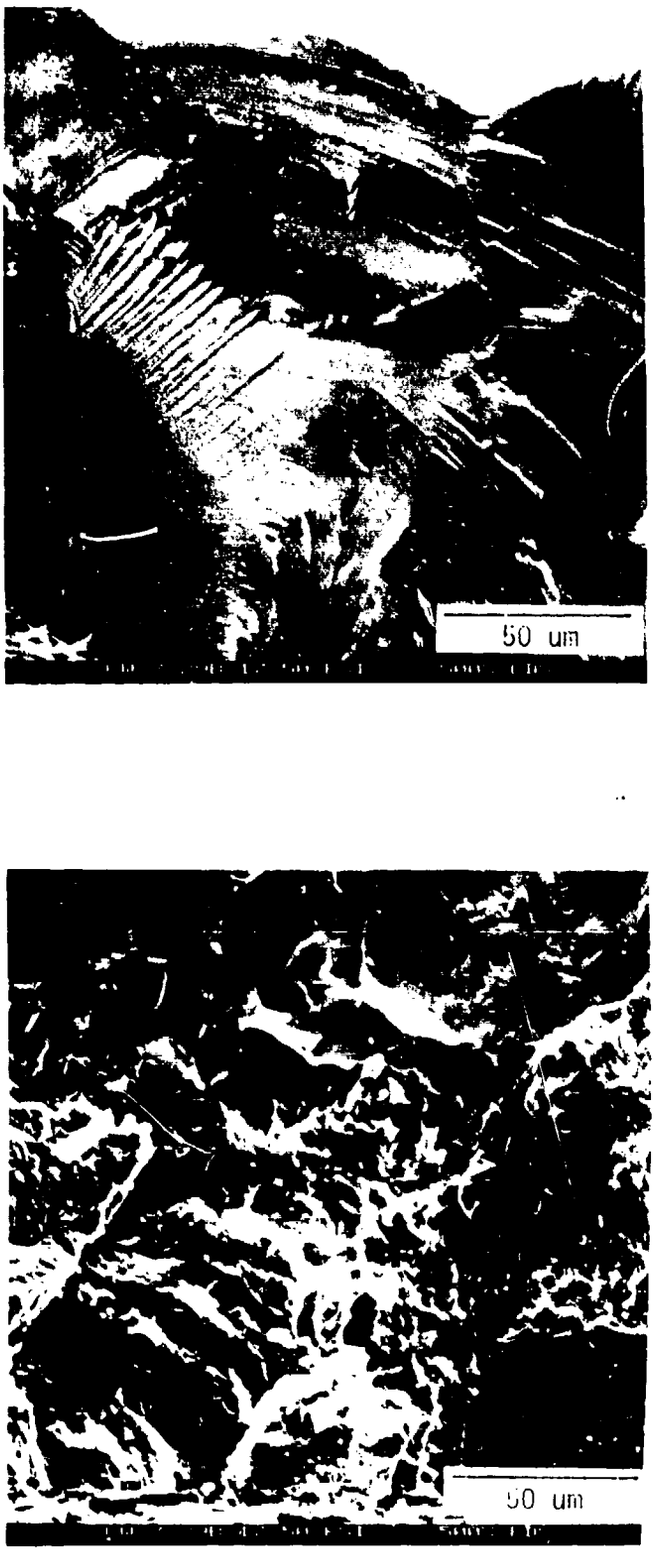

Figure A-10. SEM Fractographs of Flexure Specimen Showing Details of Transgranular Cleavage Features in Last (Upper) and First Deposited (Lower) Regions of Flexure Specimen (Spec. No. CW-3-298).

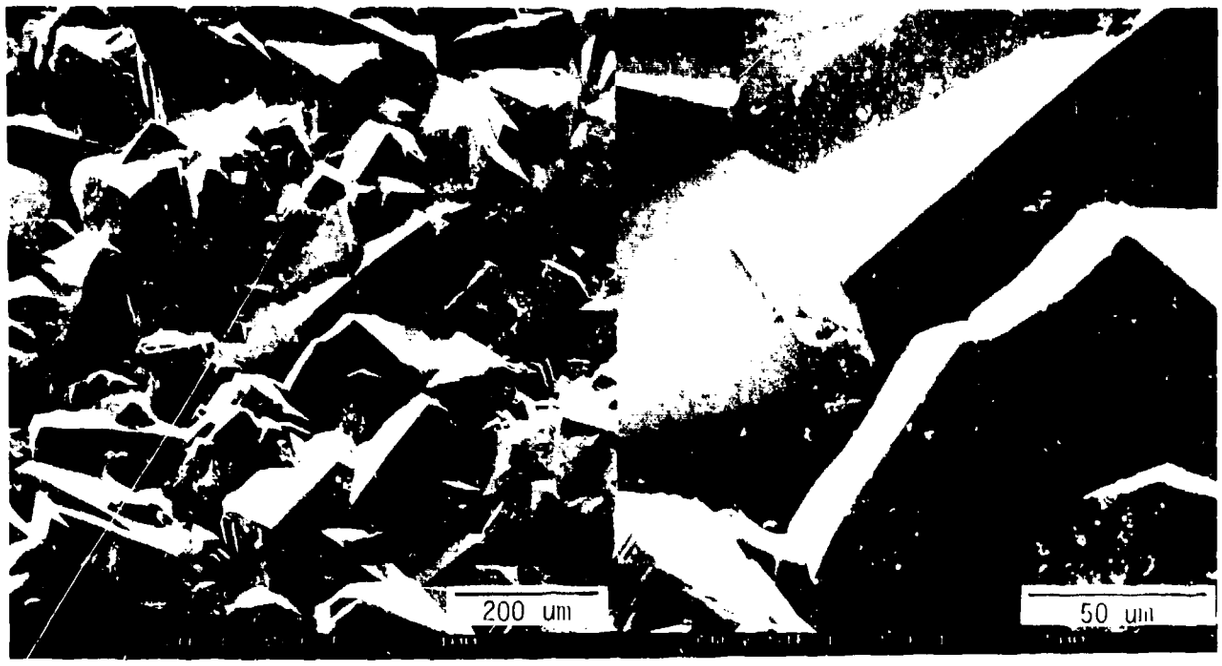

Figure A-11. SEM Photomicrographs of Last Deposited Surface (Upper) and Fractograph of Flexure Specimen (Lower) Showing Transgranular Cleavage Features (Spec. No. 3-51B)

Figure A-12. SEM Fractograph Showing Details of Transgranular Cleavage Features (Spec. No. 3-51B).

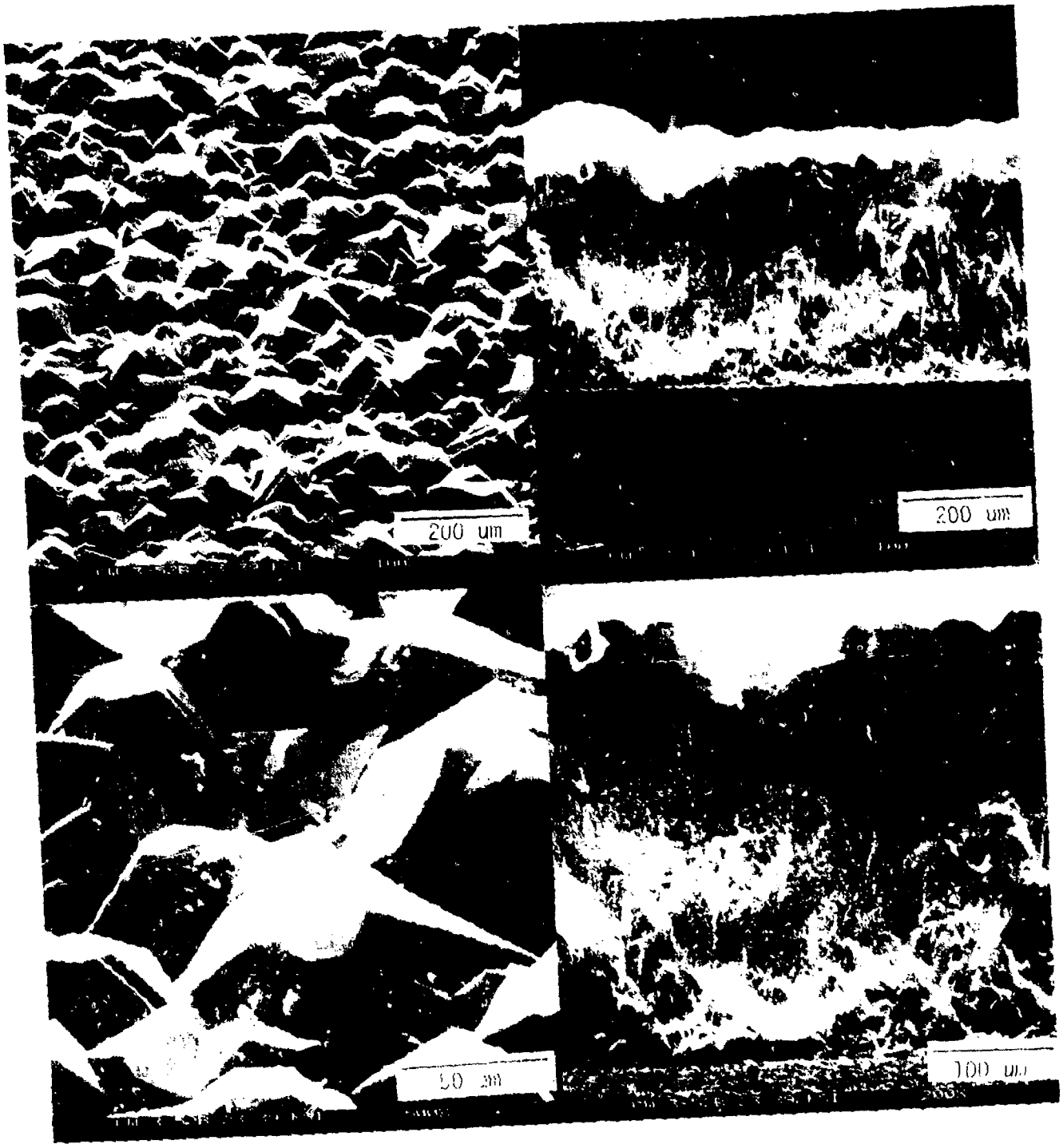

Figure A-13. SEM Photomicrographs of Last Deposited Surface (Left) and Fractograph of Flexure Specimen Showing Transgranular Cleavage Features (Spec. No. CW-3-52B).

Figure A-14. SEM Fractograph Showing Details of Transgranular Cleavage Features (Spec. No. 3-52B).

APPENDIX B
MORPHOLOGY AND FRACTOGRAPHY OF HOT WALL ONE INCH REACTOR DEPOSITS

APPENDIX B

MORPHOLOGY AND FRACTOGRAPHY OF HOT WALL ONE INCH REACTOR DEPOSITS

The following SEM photomicrographs are examples of the range of morphologies and fracture patterns developed in deposits from the hot wall reactor experiments. Each photomicrograph lists the deposition sequence, flexure strength, and magnification. The upper surface of each fractograph represents the last deposited surface (LDS) region which was under tensile loading. Specific deposition parameters are given in Table 2-5.

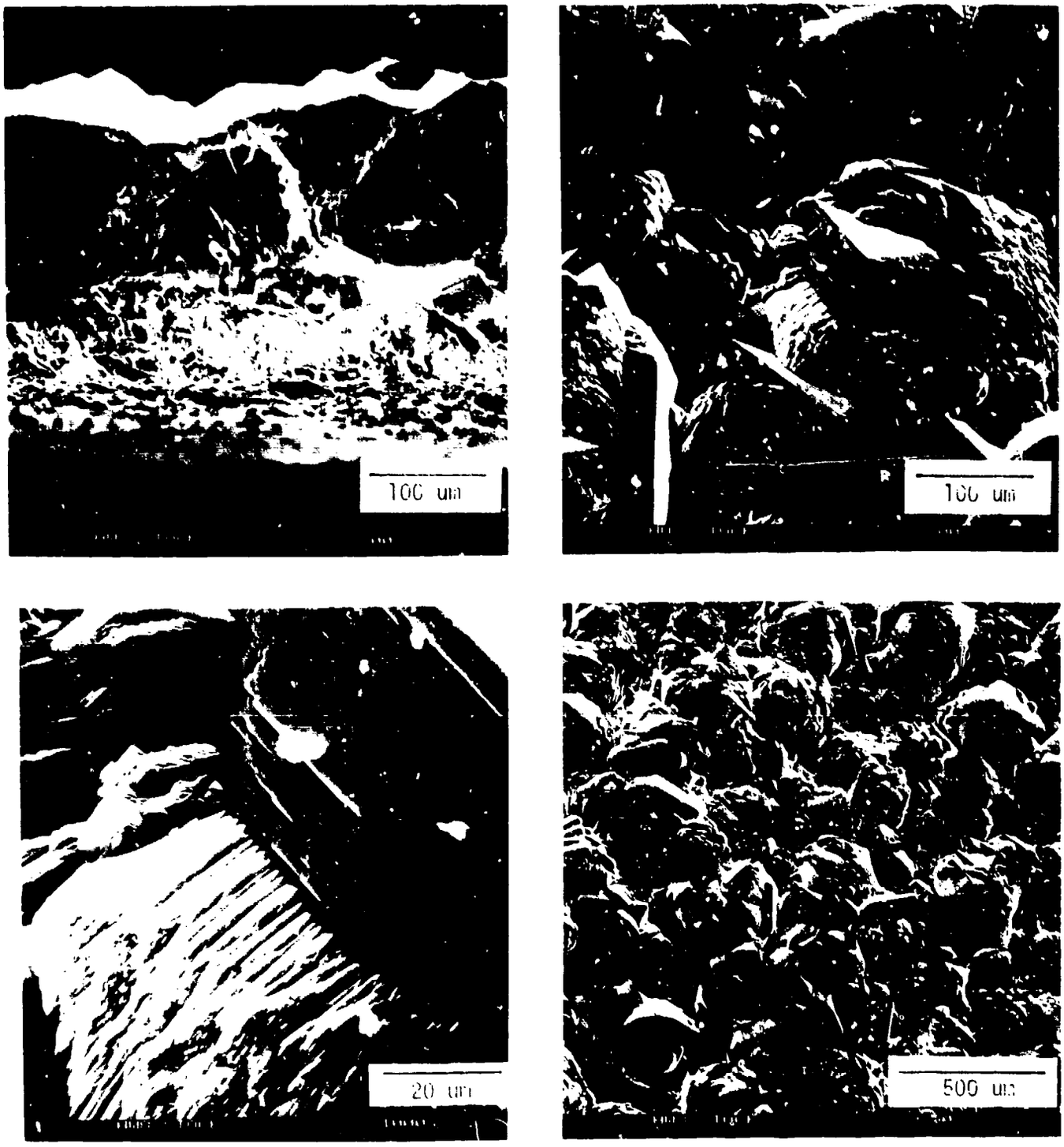

Figure B-1. SEM Photomicrographs of Last Deposited Surface and Fractograph Showing an Apparent Two Layer Deposit. Boron Dopant Appears to Promote Growth Normal to Usual Deposition Direction (Spec. No. HW-8).

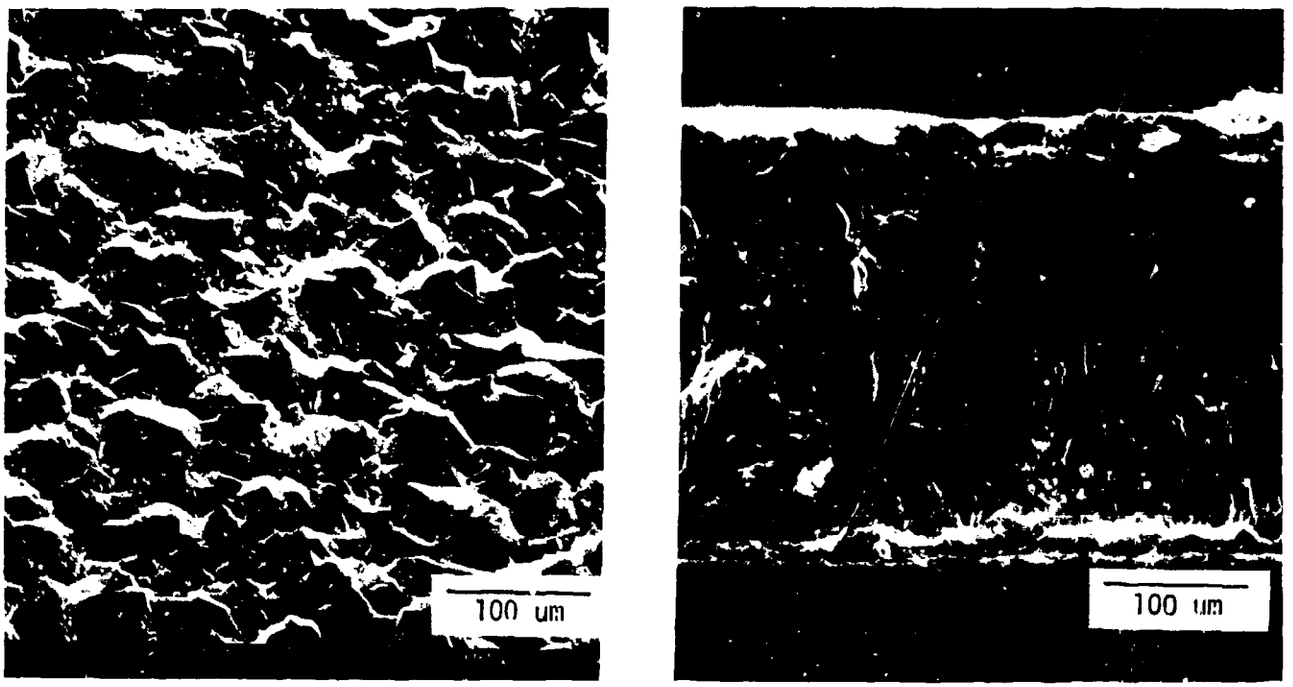

Figure B-2. SEM Photomicrographs of Last Deposited Surface (Left) and Fractograph of Flexure Specimen Showing Bimodal Fracture Markings (Transgranular and Grain Boundary Cleavage) (Spec No. 12-2).

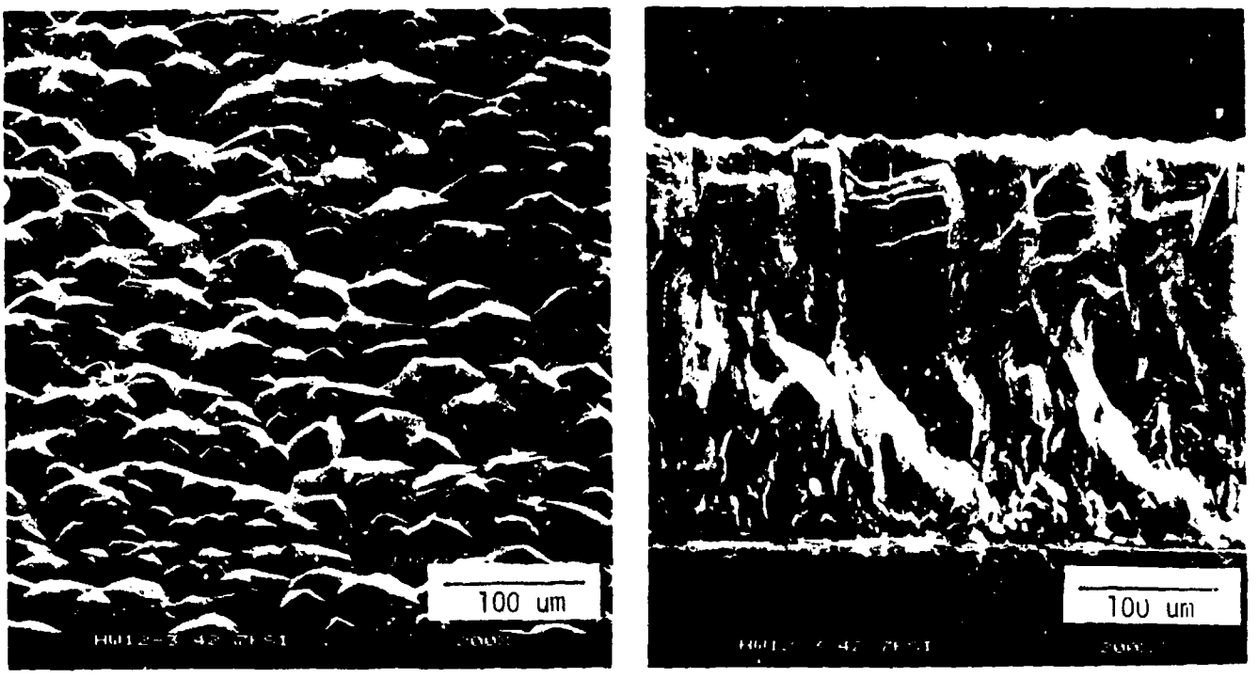

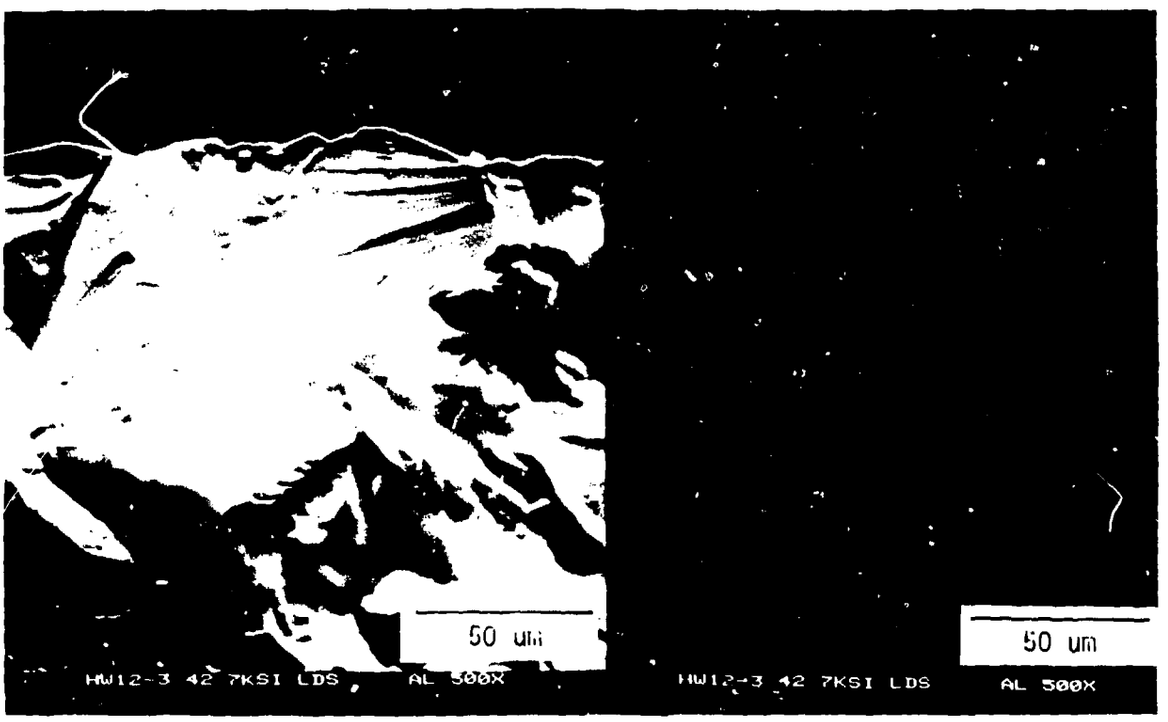

Figure B-3. SEM Photomicrographs of Last Deposited Surface (Upper Left) and Associated Fractograph (Upper Right) Showing Bimodal Fracture Features. Also shown is Reference Al Background Concentration Using SEM-XRD Mapping Mode (Spec. No. HW 12-3).

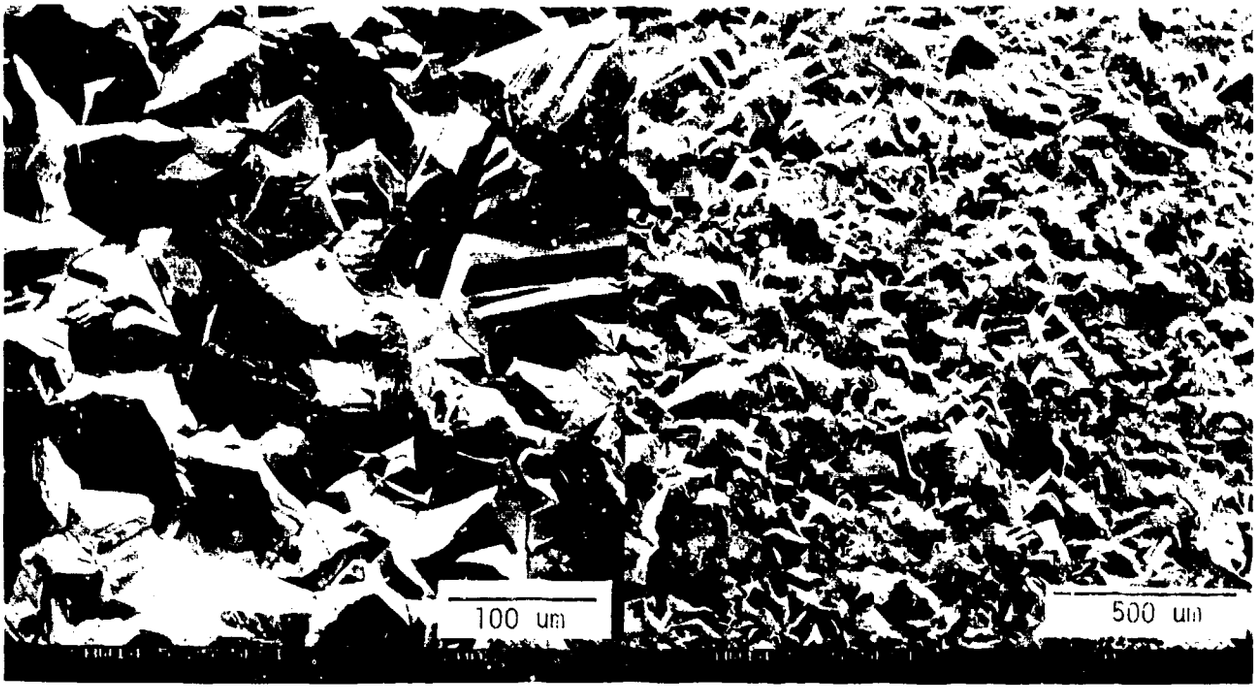

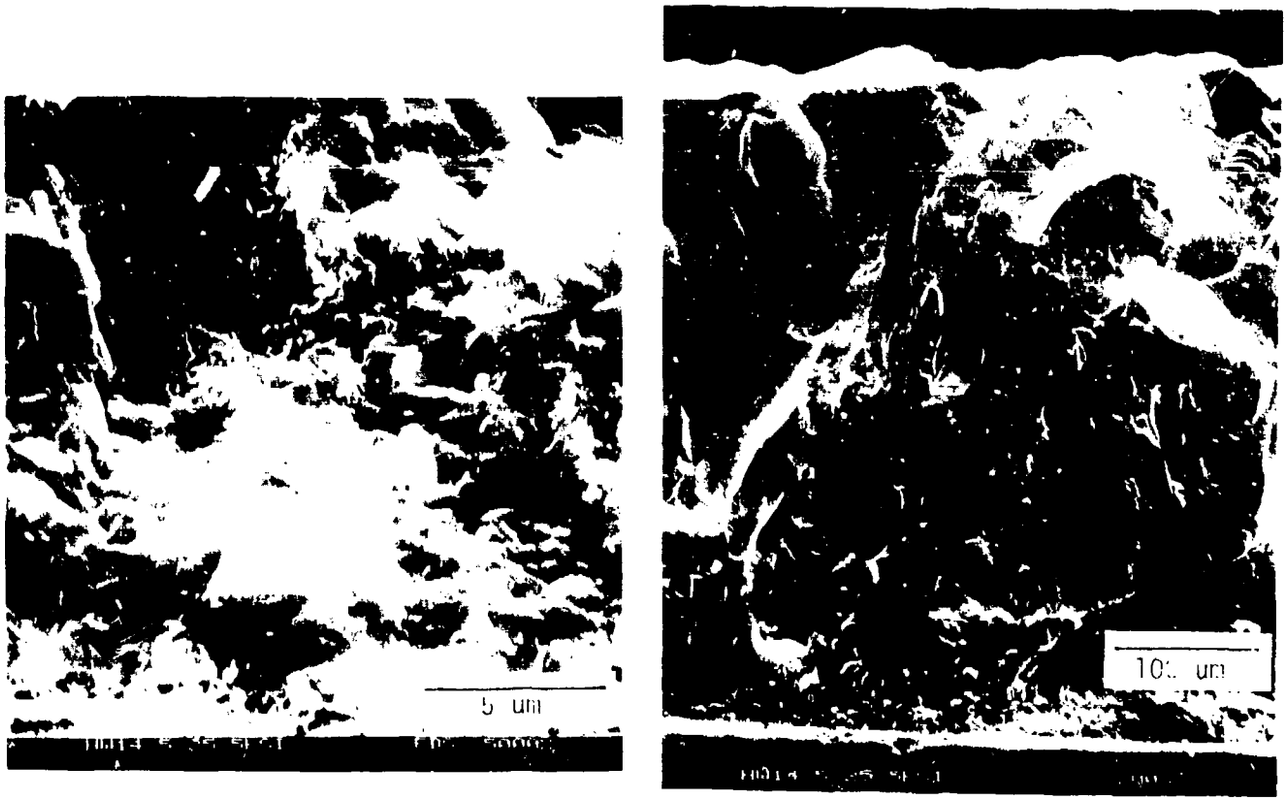

Figure B-4. SEM Photomicrographs of Last Deposited Surface (Upper) and Fractograph (Lower) Showing Transgranular Fracture Features and Porosity (Lower Left) in FDS Layer (Spec. No. 14-5).

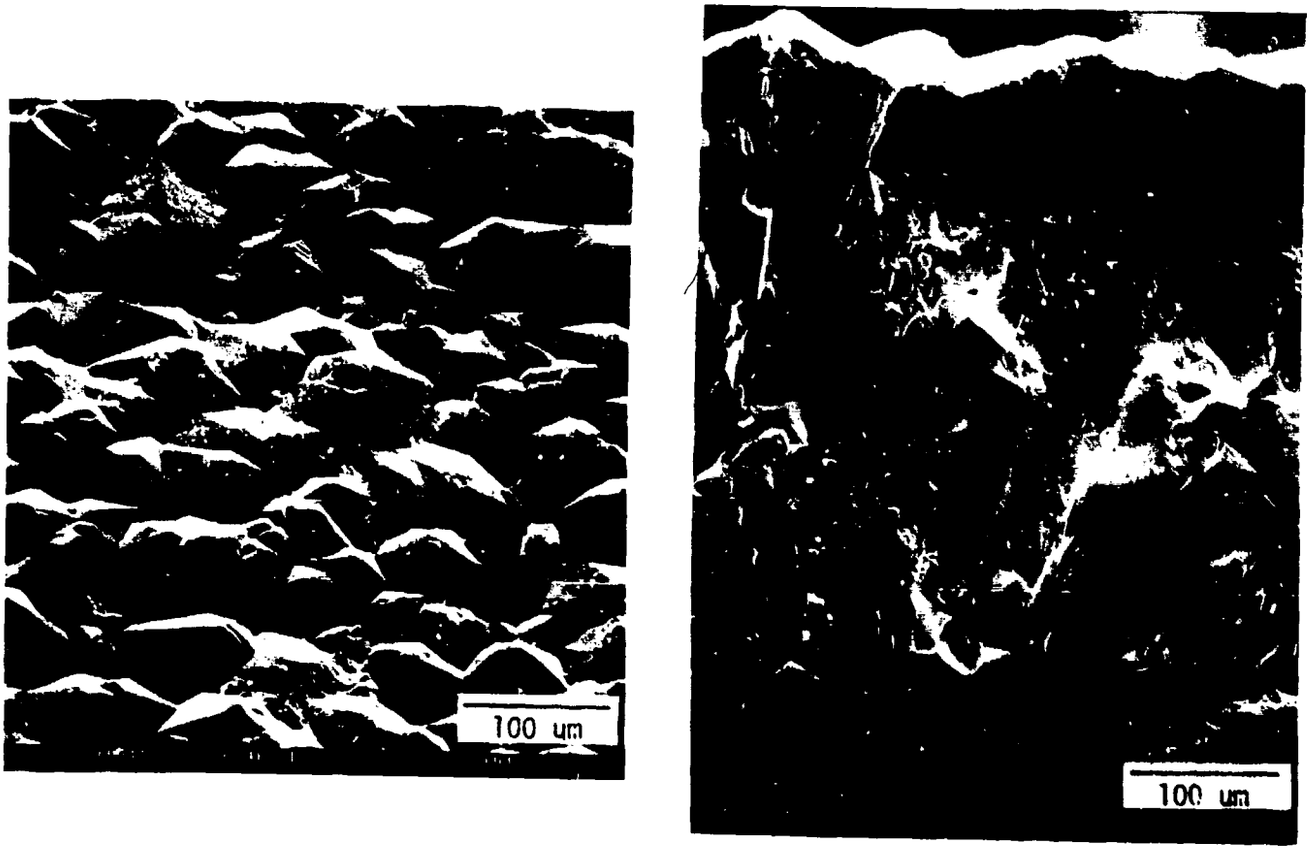

Figure B-5. SEM Photomicrographs of Last Deposited Surface (Left) and Fractograph (Right) Showing Bimodal Fracture Features.

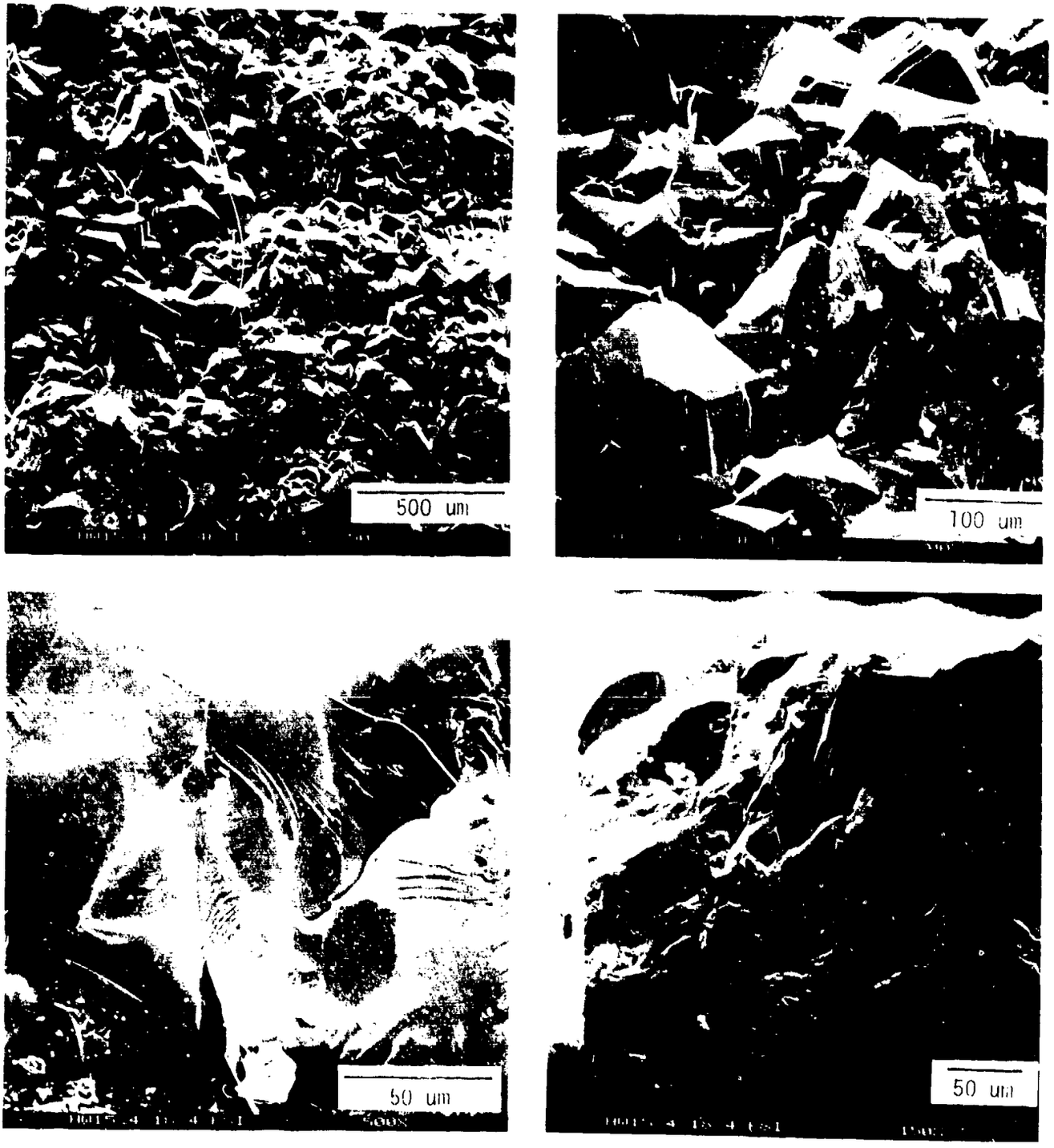

Figure B-6. SEM Photomicrographs of Last Deposited Surface (Upper) and Fractograph (Lower) Showing Transgranular Cleavage Fracture Features (Spec. No. HW 15-4).

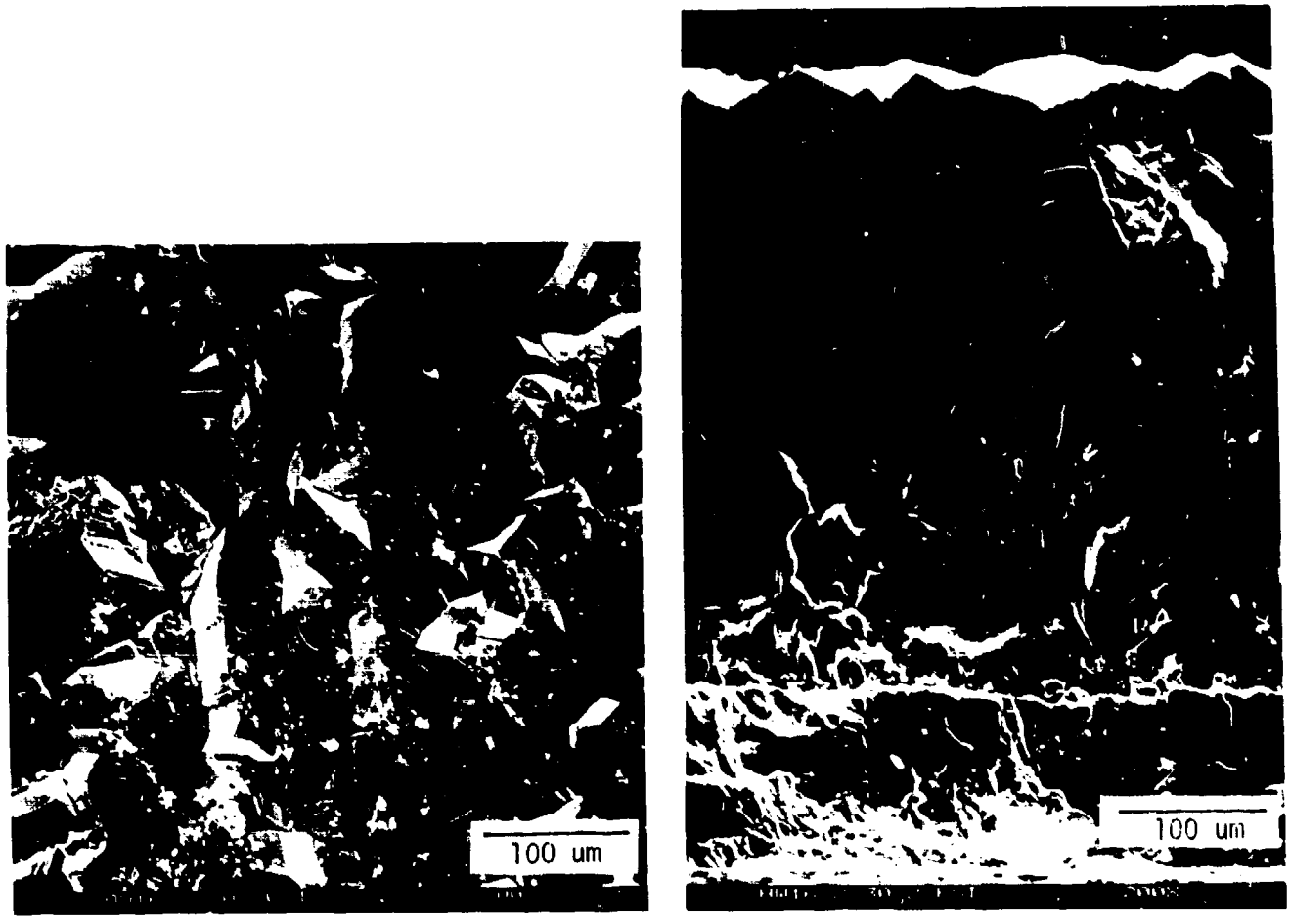

Figure B-7. SEM Photomicrographs of Last Deposited Surface (Left) and Fractograph (Right) Showing Bimodal Cleavage Fracture Features (Spec. No. HW 16-2).

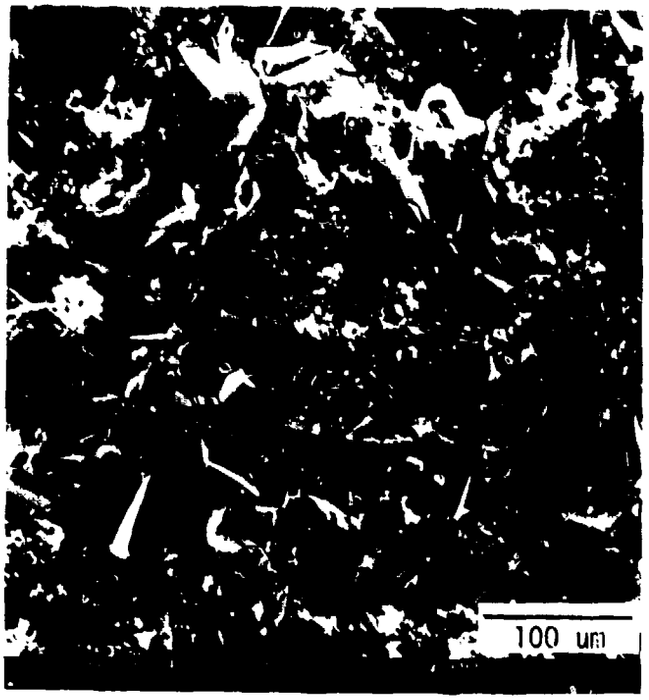

Figure B-8. SEM Photomicrographs of Last Deposited Surface (Upper Left) and Fractographs Showing Bimodal Cleavage Fracture Markings (Spec. No. 16-4).

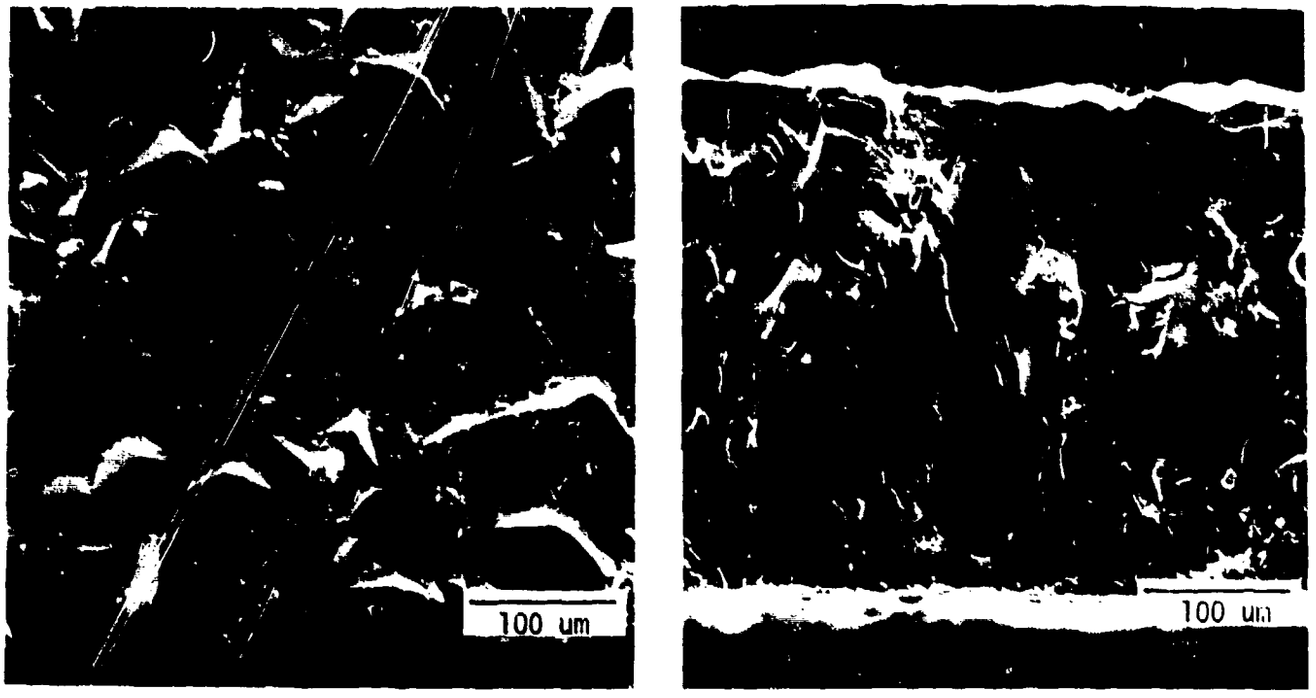

Figure B-9. SEM Photomicrographs of Last Deposited Surface (Left) and Fractographs Showing Transgranular Cleavage Markings (Spec. No. HW 17-1)

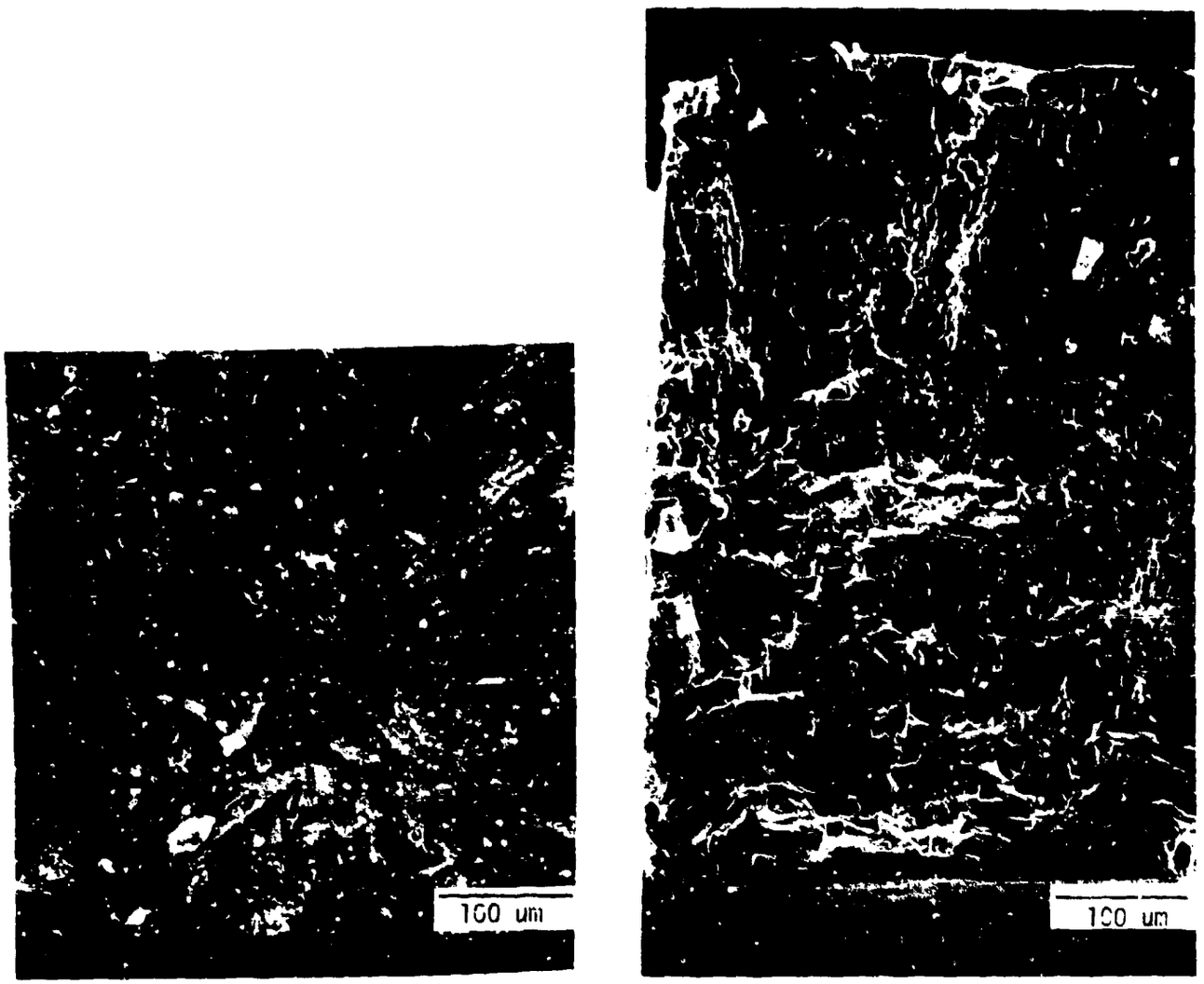

Figure B-10. SEM Photomicrograph of Last Deposited Surface (Left) and Fractograph Showing Evidence for Multiple Layer Growth (Spec. No. HW 18-1-L).

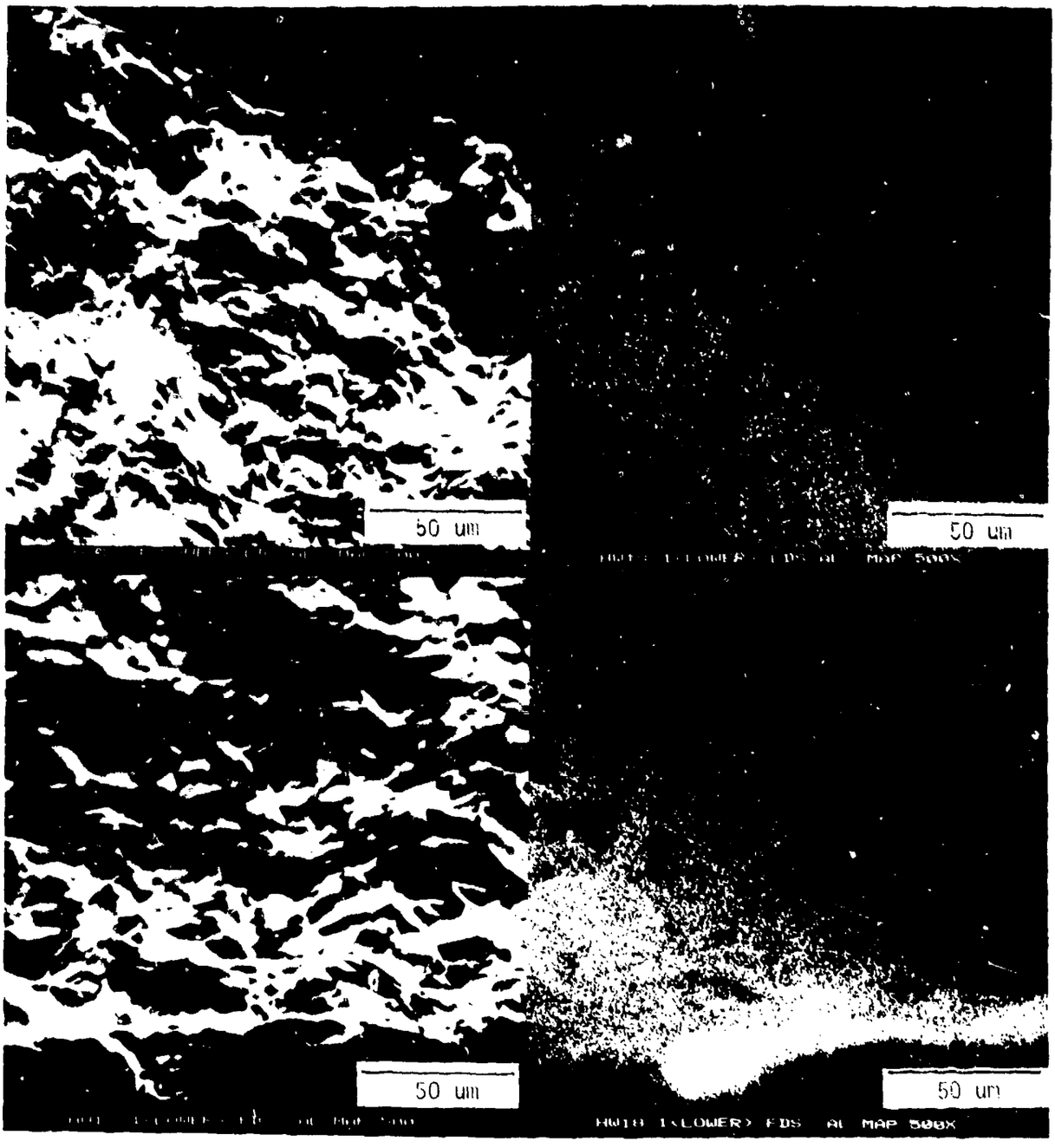

Figure B-11. SEM Fractographs of LDS and FDS Regions and Associated Al Concentration Maps Illustrating Significantly Higher Al Concentrations Compared to Background (See Figure B-3) (Spec No. HW 18-1-L).

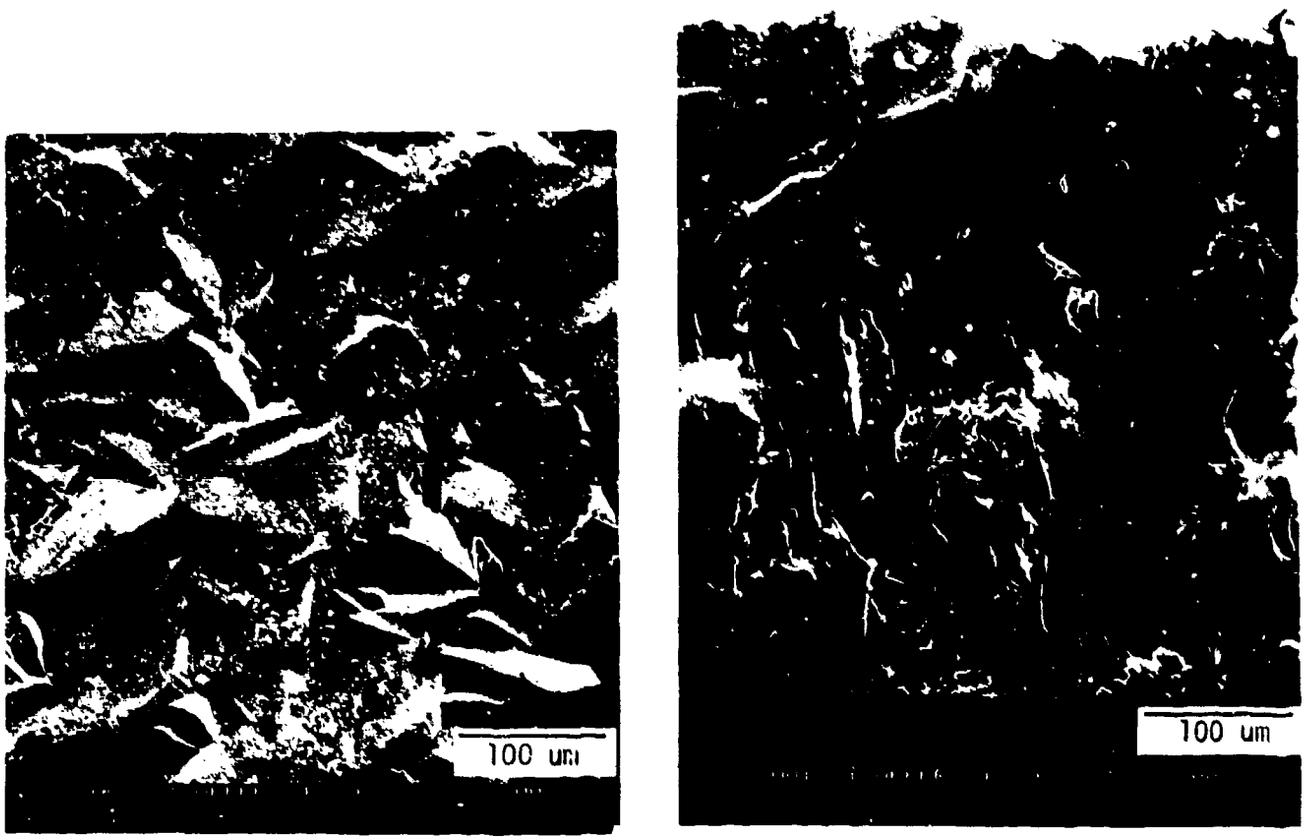

Figure B-12. SEM Photomicrographs of Last Deposited Surface (Left) and Fractograph Showing Transgranular Cleavage Markings (Spec. No. 18-1-U).

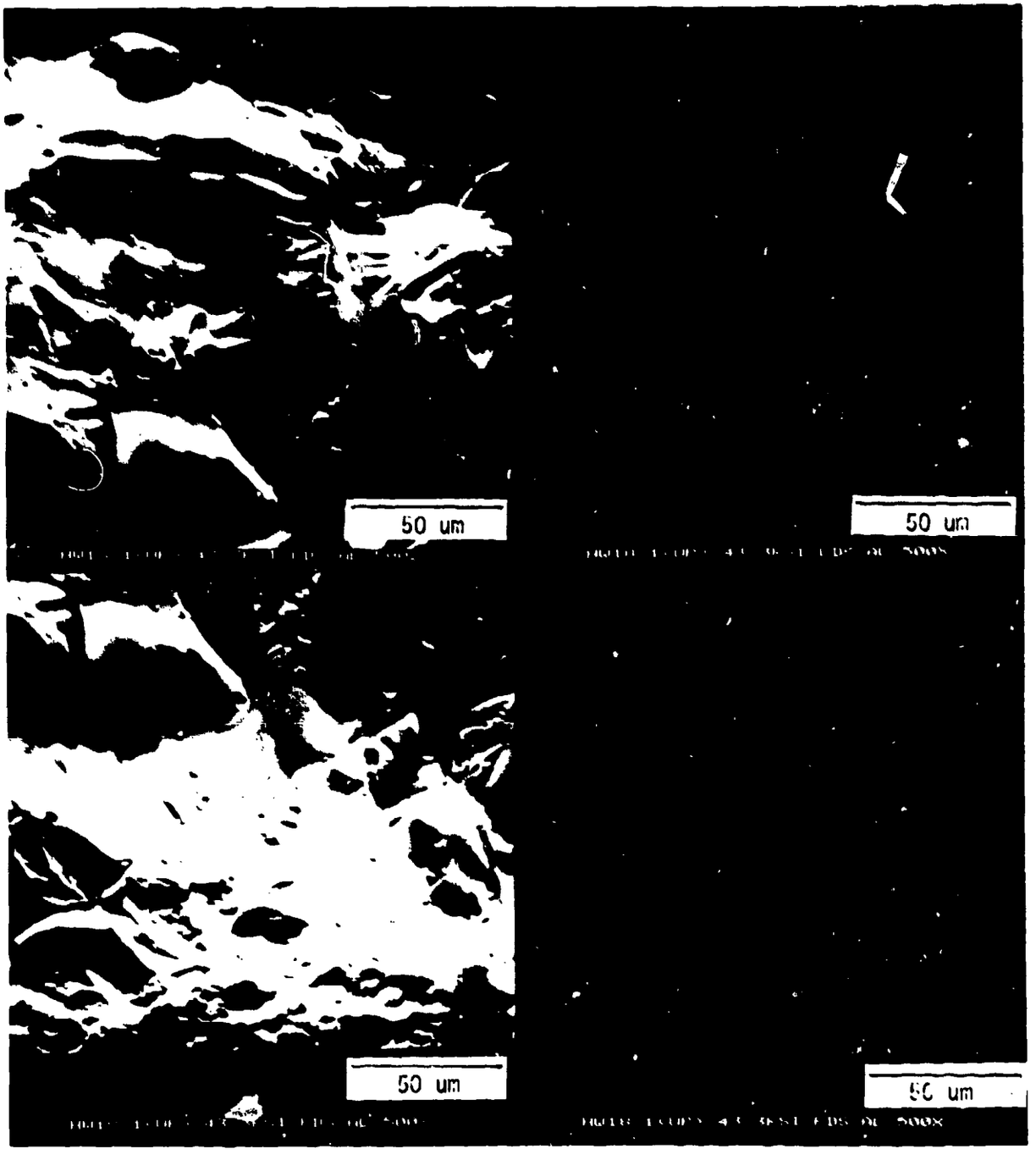

Figure B-13. SEM Fractographs of LDS and FDS Regions and Associated Al Concentration Maps Illustrating Decreased Al Concentration Compared to Deposit CLoser to Nozzle Inlet (Compare with Figure B-11) (Spec No. HW 18-1-U).

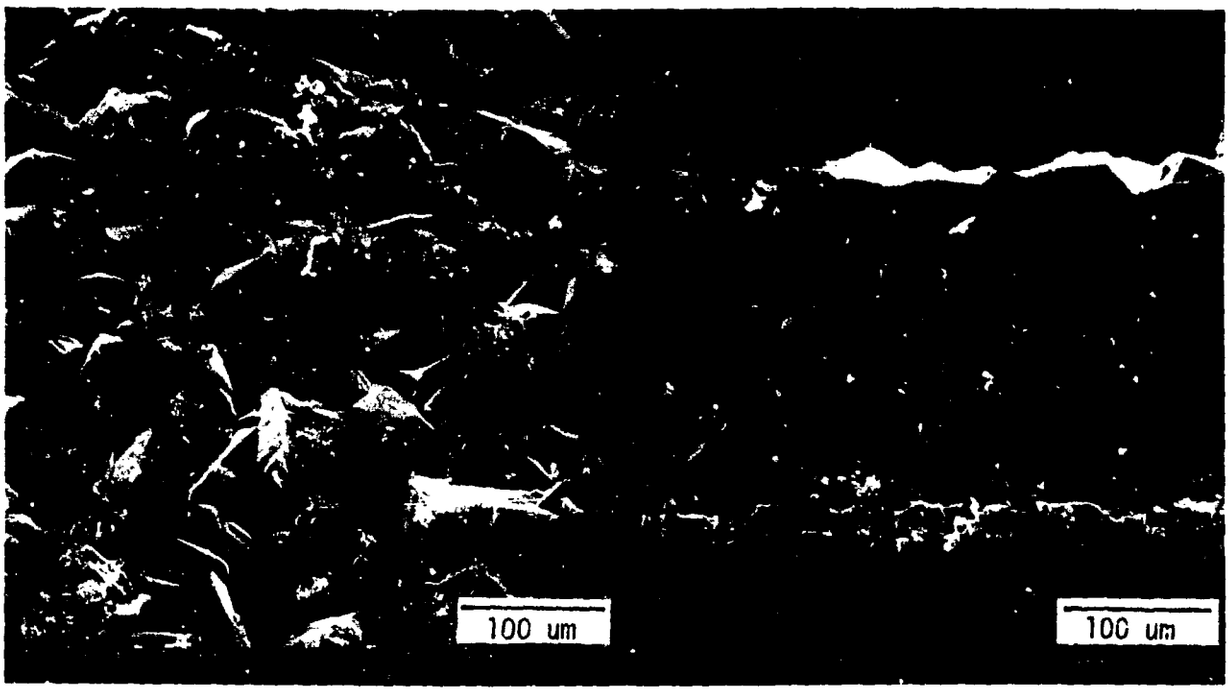

Figure B-14. SEM Photomicrographs of Last Deposited Surface (Left) and Fractograph Showing Transgranular Cleavage Markings (Spec. No. 18-3-U).

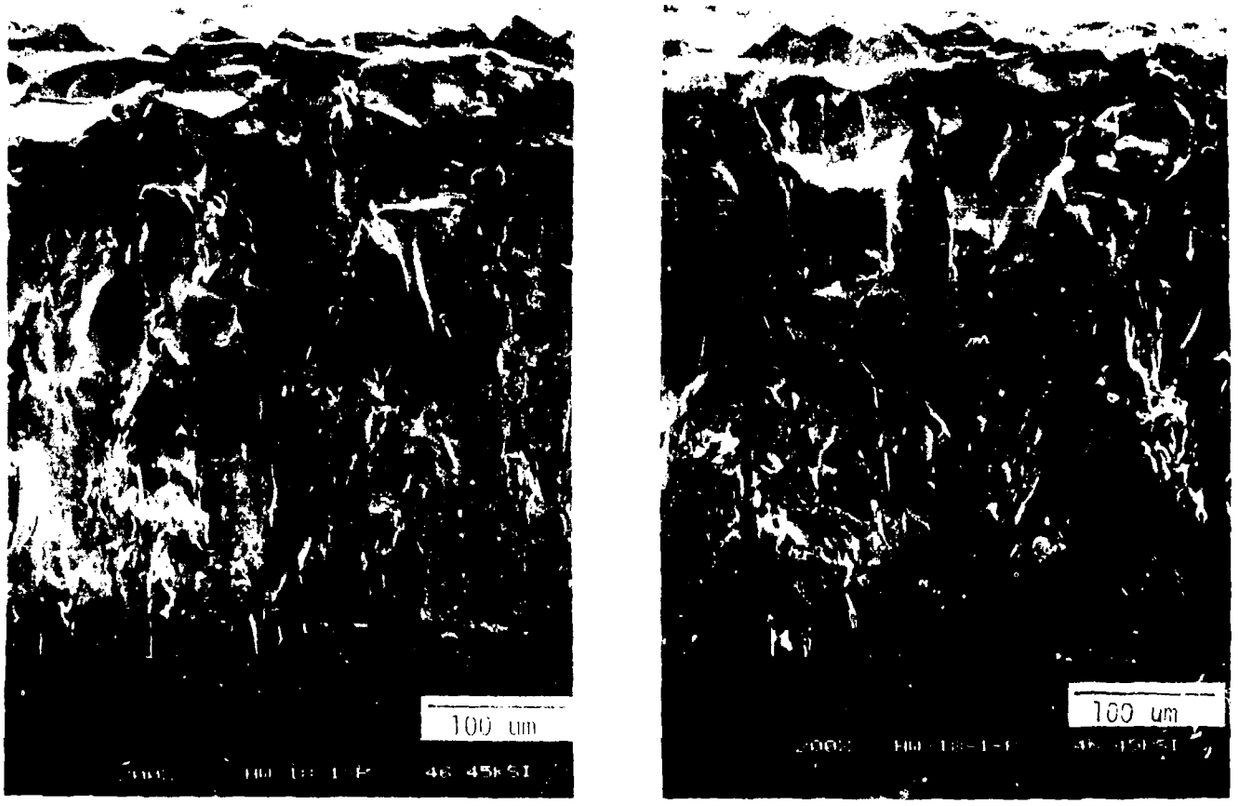

Figure B-15. SEM Photomicrographs of Last Deposited Surface (Upper) and Fractographs (Lower) Showing Transgranular Cleavage Markings (Spec. No. 18-1-P).

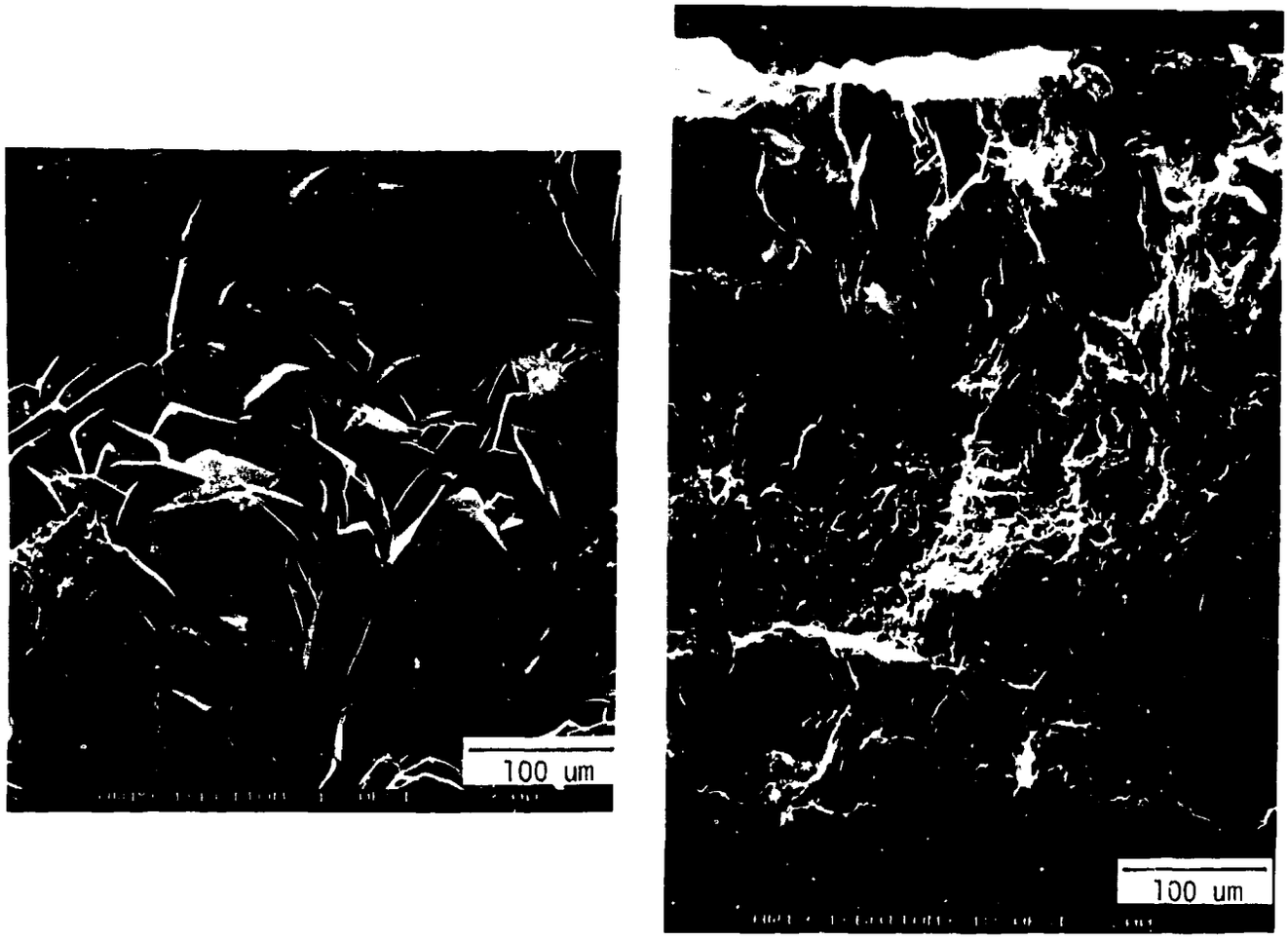

Figure B-16. SEM Photomicrograph of Last Deposited Surface (Left) and Fractograph Showing Transgranular Cleavage Features (Spec. No. HW 19-1).

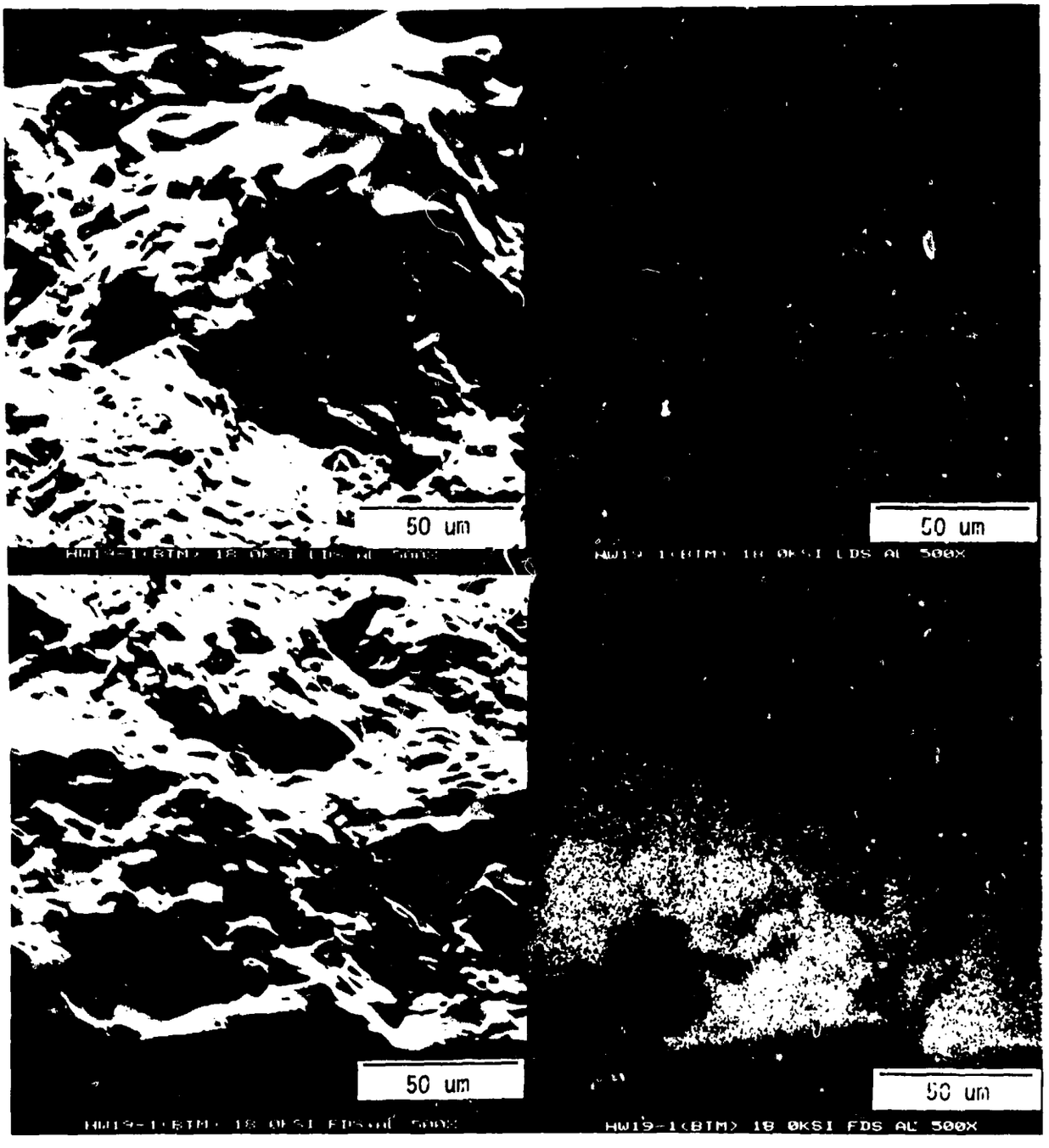

Figure B-17. SEM Fractographs of LDS and FDS (Left) Regions and Associated Al Concentration Maps. Specimen Located Near Nozzle Inlet (Spec. No. HW 19-1-B).

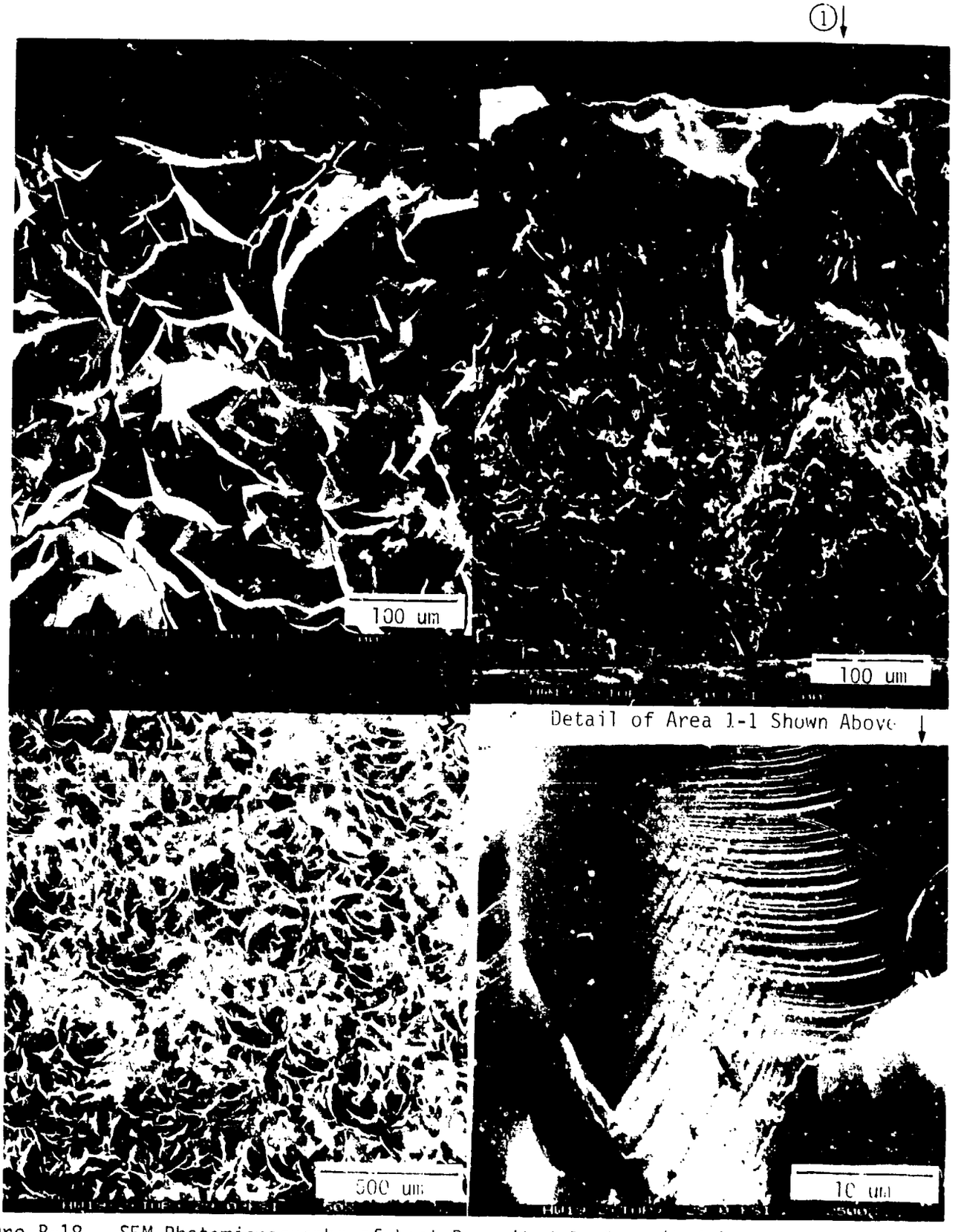

Figure B-18. SEM Photomicrographs of Last Deposited Surface (Left) and Fractographs (Right) Showing Transgranular Cleavage Markings (Spec. No. HW 19-2-T).

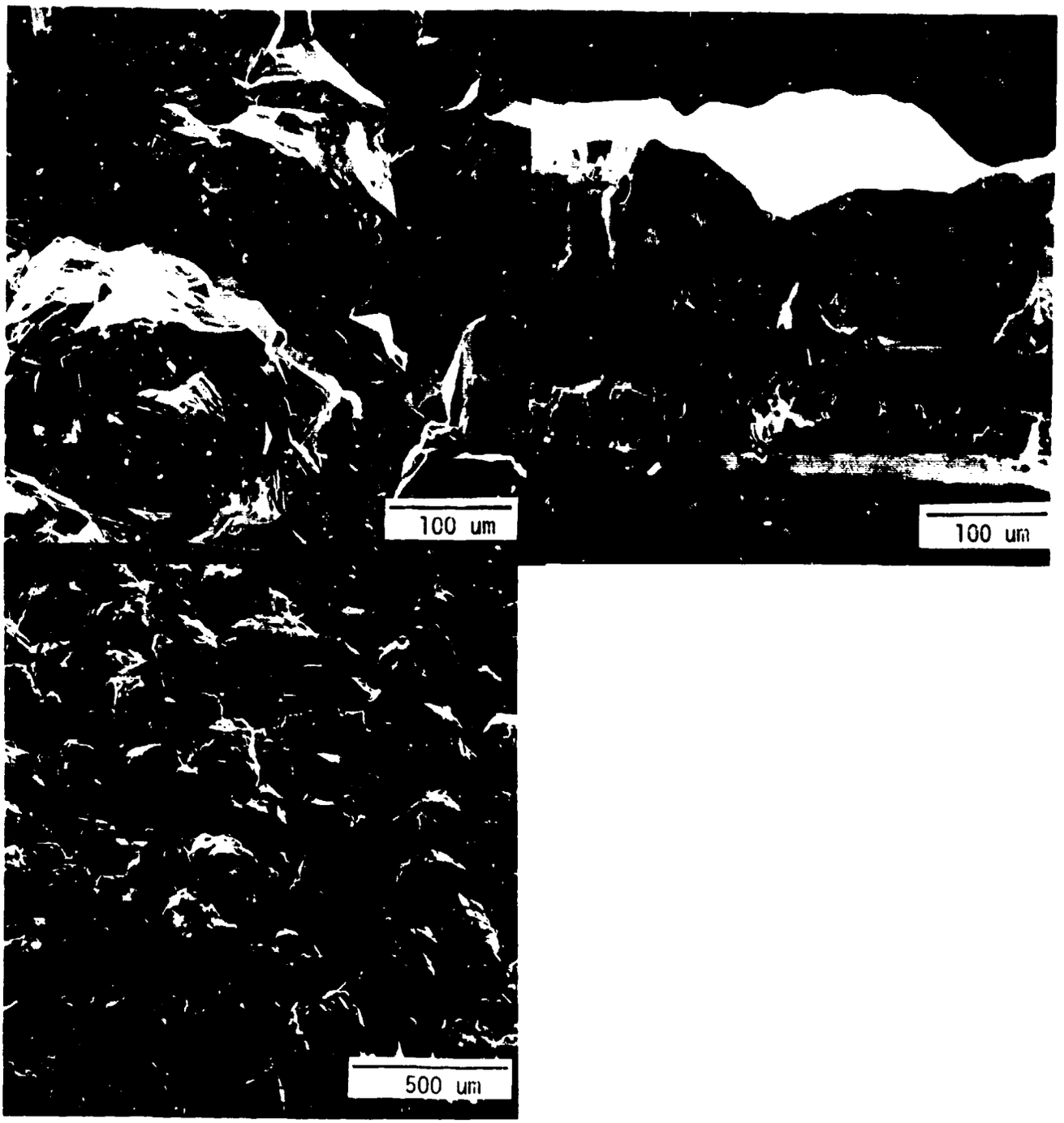

Figure B-19. SEM Photomicrographs of Last Deposited Surface (Left) and Fractograph (Right) Showing Transgranular Cleavage Markings (Spec. No. HW 19-4-T).

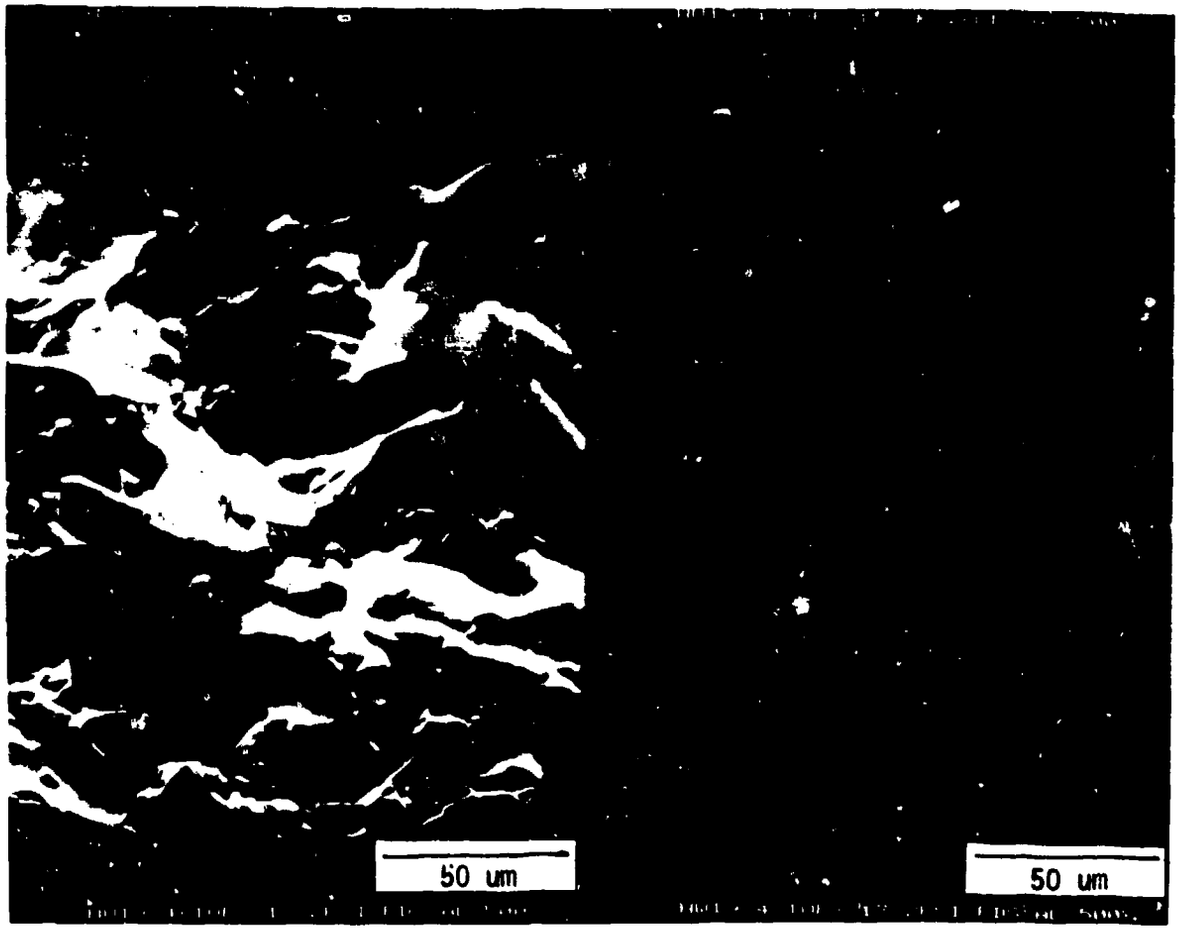

Figure B-20. SEM Fractograph of FDS Region and Associated Al Concentration Map (Spec. No. HW 19-4-T).

APPENDIX C
MORPHOLOGY AND FRACTOGRAPHY OF HOT WALL FOUR-INCH REACTOR DEPOSITS

APPENDIX C

MORPHOLOGY AND FRACTOGRAPHY OF HOT WALL FOUR-INCH REACTOR DEPOSITS

The following SEM photomicrographs are examples of the range of morphologies and fracture patterns developed in deposits from the hot wall reactor experiments. Each photomicrograph lists the deposition sequence, flexure strength, and magnification. The upper surface of each fractograph represents the region which was under tensile loading. Specific deposition parameters are listed in Table 2-7.

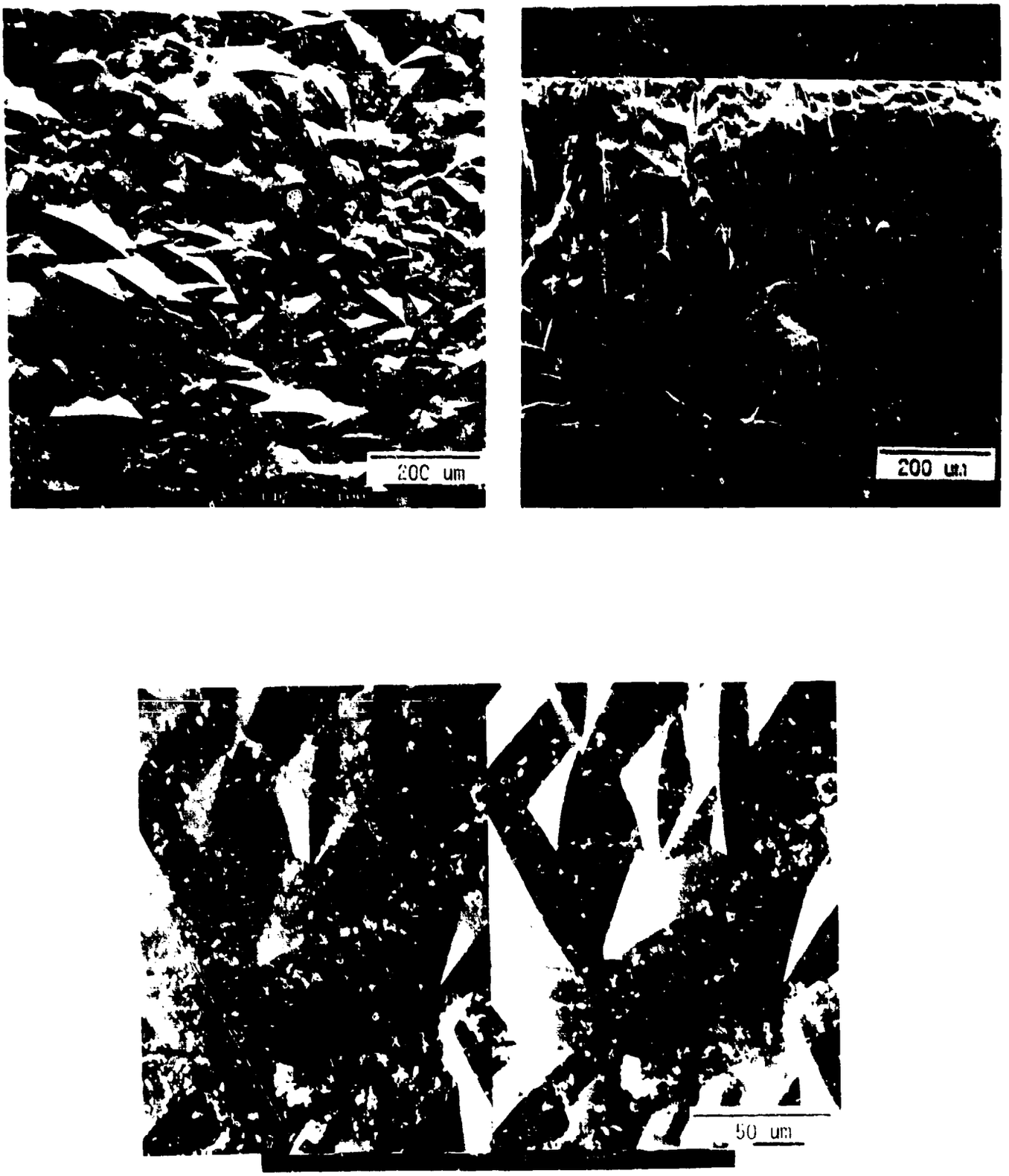

Figure C-1. SEM Photomicrographs of Last Deposited Surface (Left and Bottom) and Fractograph (Upper Right) Showing Bimodal Fracture Markings (Majority Intergranular Fracture) (Spec No. HW 4-328).

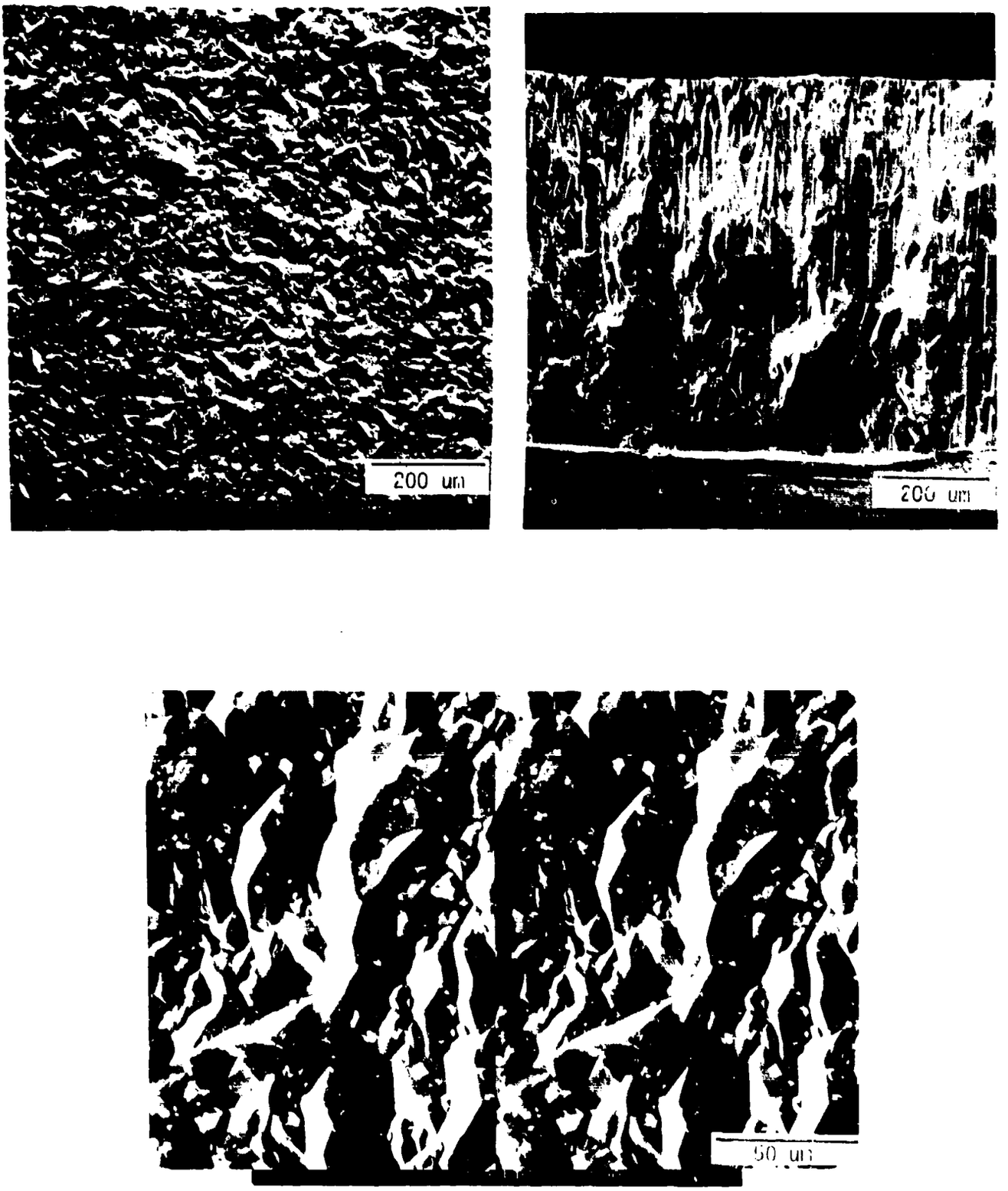

Figure C-2. SEM Photomicrographs of Last Deposited Surface (Left and Bottom) and Fractograph (Upper Right) Showing Intergranular Cleavage Details (Spec No. HW 4-329-2).

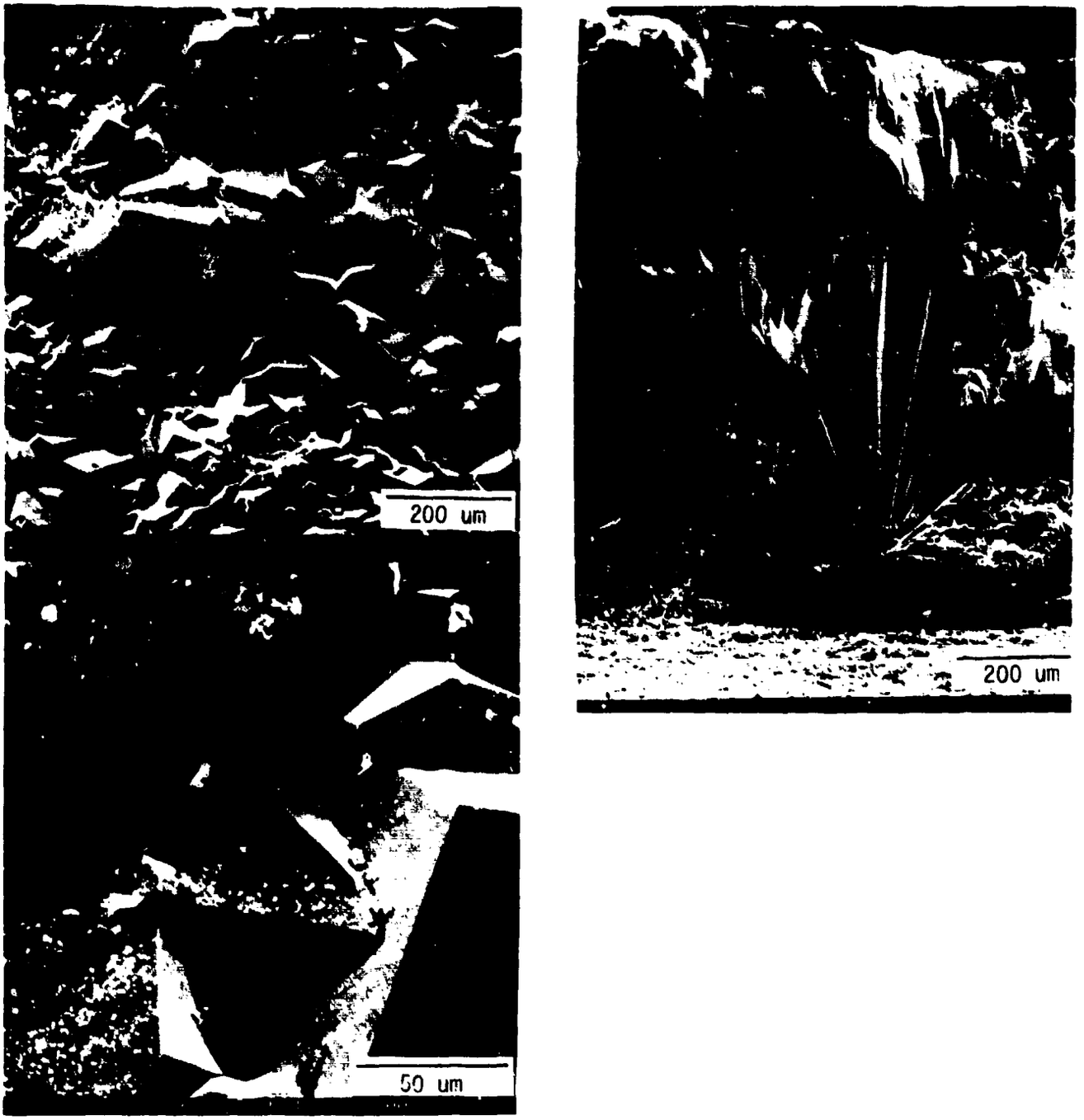

Figure C-3. SEM Photomicrographs of Last Deposited Surface (Left) and Fractograph (Right) Showing Bimodal Fracture Markings. (Spec No. HW 4-378).

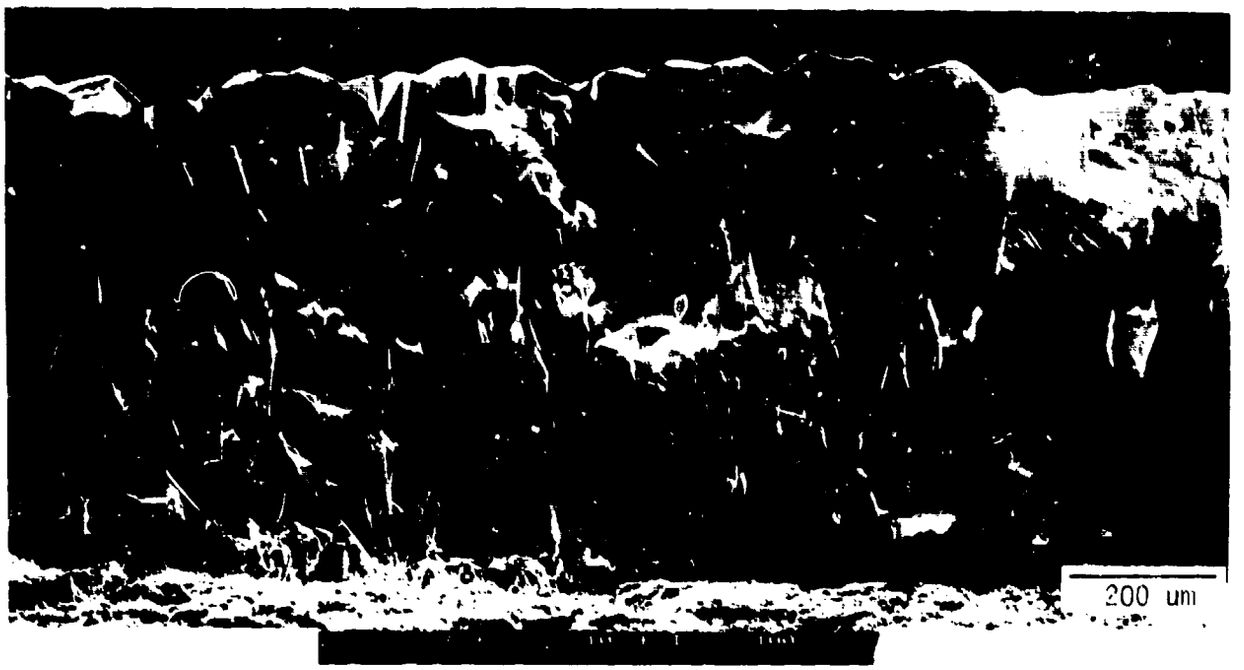

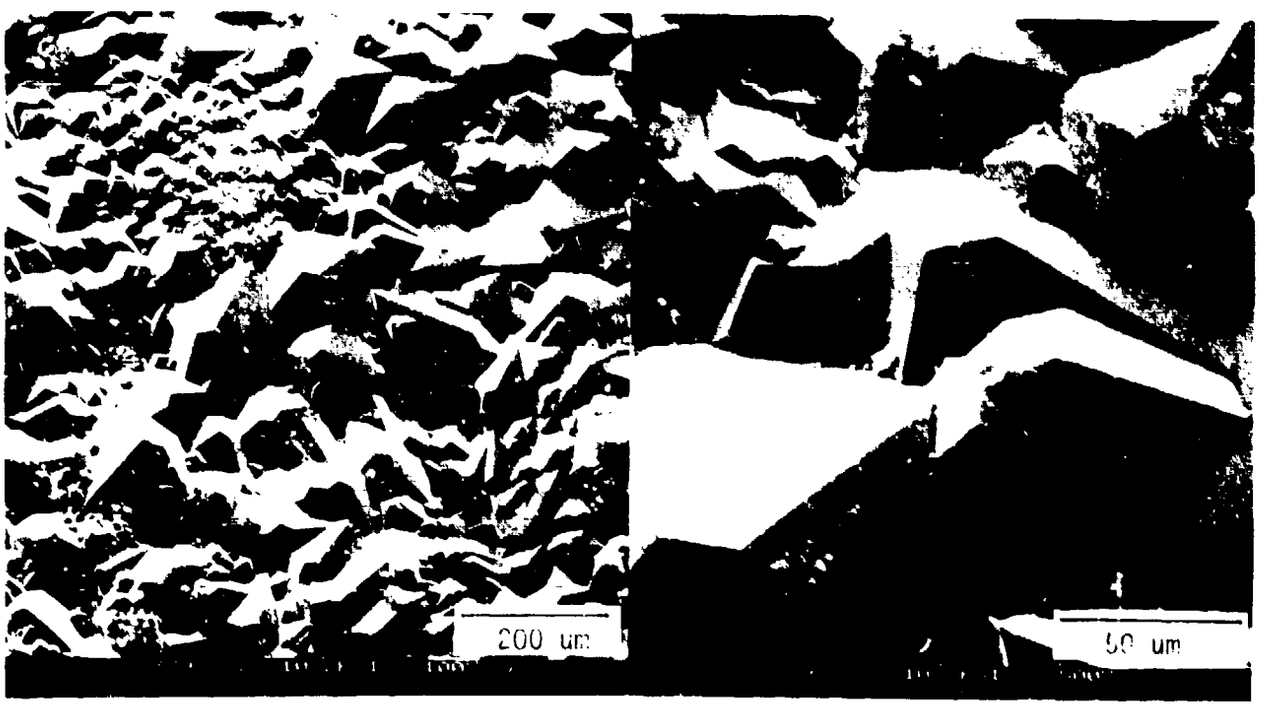

Figure C-4. SEM Photomicrographs of Last Deposited Surface (Bottom) and Fractograph (Top) Showing Bimodal Fracture Markings (Majority Intergranular Fracture) (Spec No. HW 4-379).

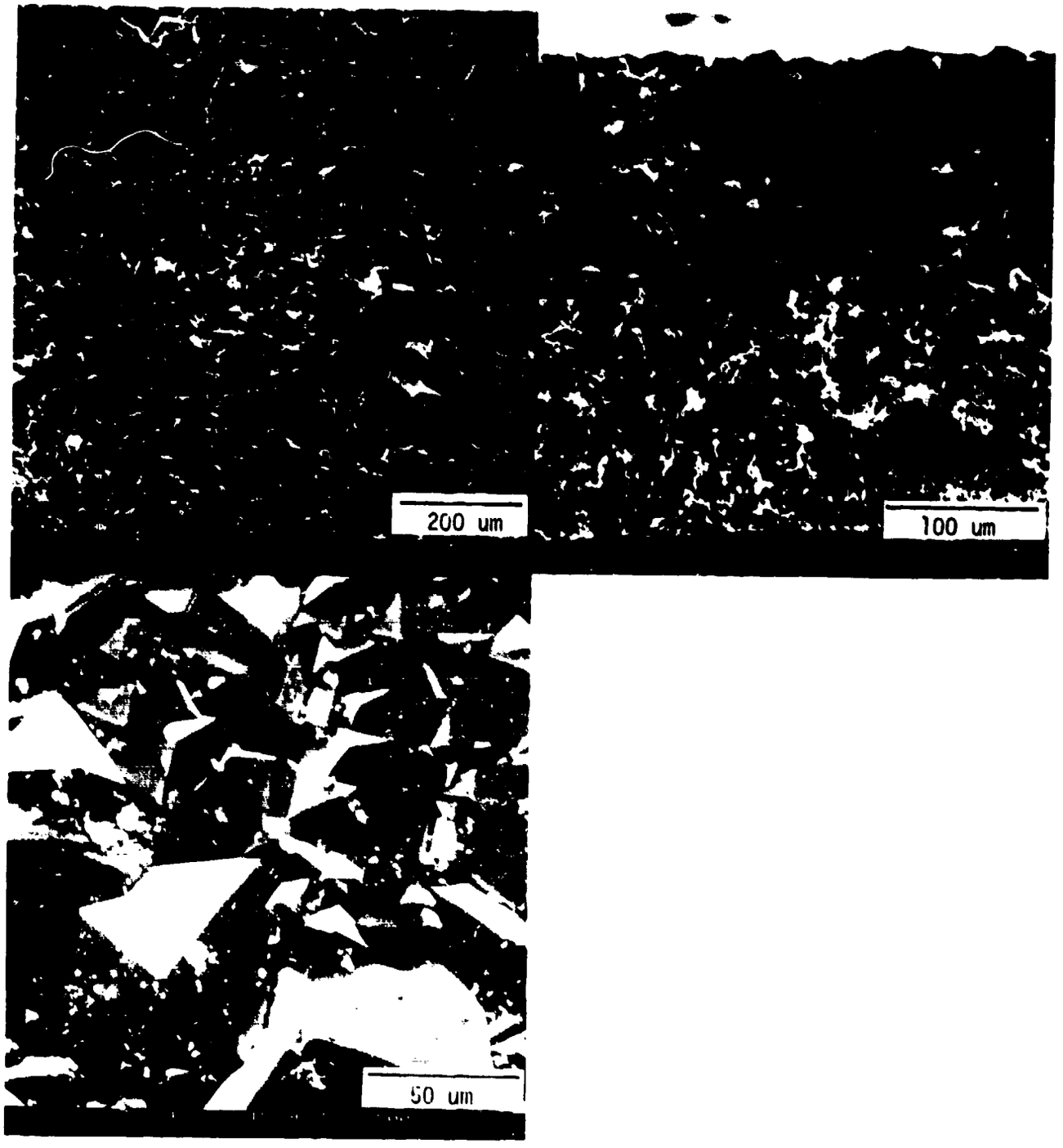

Figure C-5. SEM Photomicrographs of Last Deposited Surface (Left) and Fractograph (Right) Showing Transgranular Cleavage Details (Spec No. HW 4-382).

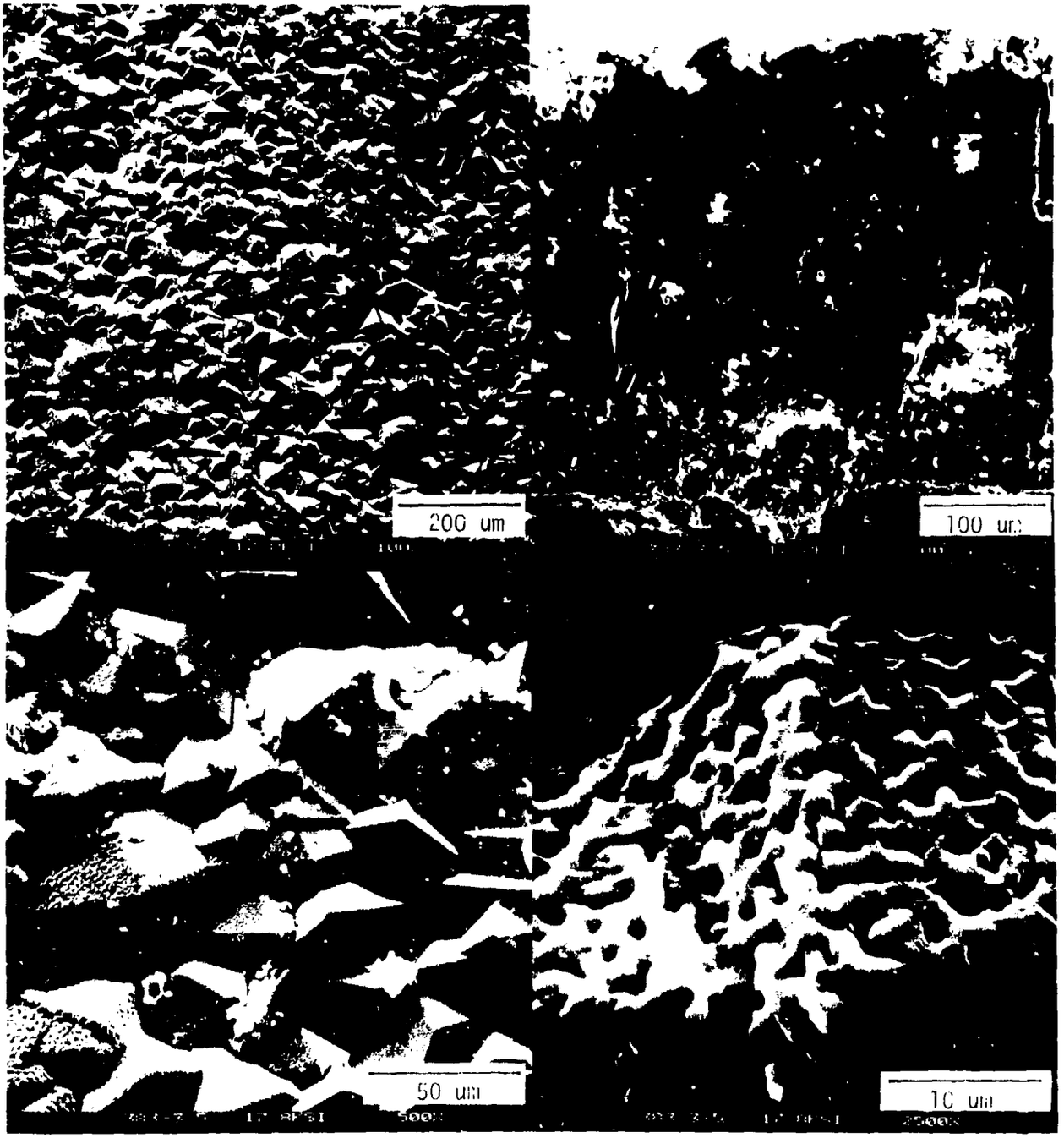

Figure C-6. SEM Photomicrographs of Last Deposited Surface (Left and Right Bottom) and Fractograph (Upper Right) Showing Transgranular Cleavage Details. Note Evidence of Transient Liquid Layer (Bottom). (Spec No. HW 4-383).

BASIC DISTRIBUTION LIST

Technical and Summary Reports November 1979

Organization	Copies
Defense Documentation Center Cameron Station Alexandria, VA 22314	12
Office of Naval Research Department of the Navy 800 N. Quincy Street Arlington, VA 22217	
ATTN: Code 471	1
Code 470	1
Commanding Officer Office of Naval Research Branch Office Building 114, Section D 666 Summer Street Boston, MA 02210	1
Commanding Officer Office of Naval Research Branch Office 536 South Clark Street Chicago, IL 60605	1
Office of Naval Research San Francisco Area Office One Hallidie Plaza Suite 601 San Francisco, CA 94102	1
Naval Research Laboratory Washington, DC 20375	
ATTN: Codes 6000	1
6100	1
6300	1
2627	1
Naval Air Development Center Code 606 Warminster, PA 18974	
ATTN: Mr. F. S. Williams	1
Naval Air Propulsion Test Center Trenton, NJ 08628	
ATTN: Library	1
Naval Construction Batallion Civil Engineering Laboratory Port Hueneme, CA 93043	
ATTN: Materials Division	1
Naval Electronics Laboratory San Diego, CA 92152	
ATTN: Electron Materials Sciences Division	1
Naval Missile Center Materials Consultant Code 3312-1 Point Mugu, CA 92041	1
Commanding Officer Naval Surface Weapons Center White Oak Laboratory Silver Spring, MD 20910	
ATTN: Library	1
Commander David W. Taylor Naval Ship Research and Development Center Bethesda, MD 20084	1
Naval Oceans Systems Center San Diego, CA 92132	
ATTN: Library	1
Naval Underwater System Center Newport, RI 02840	
ATTN: Library	1
Naval Postgraduate School Monterey, CA 93940	
ATTN: Mechanical Engineering Department	1
Naval Weapons Center China Lake, CA 93555	
ATTN: Library	1

BASIC DISTRIBUTION LIST (cont'd)

Organization	Copies
Naval Air Systems Command Washington, DC 20360 ATTN: Codes 52031	1
52032	1
Naval Sea System Command Washington, DC 20362 ATTN: Code 05R	1
Naval Facilities Engineering Command Alexandria, VA 22331 ATTN: Code 03	1
Scientific Advisor Commandant of the Marine Corps Washington, DC 20380 ATTN: Code AX	1
Army Research Office P. O. Box 12211 Triangle Park, NC 27709 ATTN: Metallurgy & Ceramics Program	1
Army Materials and Mechanics Research Center Watertown, MA 02172 ATTN: Research Programs Office	
Air Force Office of Scientific Research/NE Building 410 Bolling Air Force Base Washington, DC 20332 ATTN: Chemical Science Directorate	1
Electronics & Materials Sciences Directorate	1
Air Force Materials Laboratory Wright-Patterson AFB Dayton, OH 45433	1
Library Building 50, Room 134 Lawrence Radiation Laboratory Berkeley, CA	1
NASA Headquarters Washington, DC 20546 ATTN: Code RRM	1

Organization	Copies
NASA Lewis Research Center 21000 Brookpark Road Cleveland, OH 44135 ATTN: Library	1
National Bureau of Standards Washington, DC 20234 ATTN: Metals Science and Standards Division	1
Ceramics Glass and Solid State Science Division	1
Fracture and Deformation Division	1
Director Applied Physics Laboratory University of Washington 1013 Northeast Forthieth Street Seattle, WA 98105	1
Defense Metals and Ceramics Information Center Battelle Memorial Institute 505 King Avenue Columbus, OH 43201	1
Metals and Ceramics Division Oak Ridge National Laboratory P. O. Box X Oak Ridge, TN 37380	1
Los Alamos Scientific Laboratory P. O. Box 1663 Los Alamos, NM 87544 ATTN: Report Librarian	1
Argonne National Laboratory Metallurgy Division P. O. Box 229 Lemont, IL 60439	1
Brookhaven National Laboratory Technical Information Division Upton, Long Island New York 11973 ATTN: Research Library	1
Office of Naval Research Branch Office 1030 East Green Street Pasadena, CA 91106	1

SUPPLEMENTARY DISTRIBUTION LIST A
Electronic, Magnetic, and Optical Ceramics

032
June 1980

Advanced Research Projects Agency
Materials Science Director
1400 Wilson Boulevard
Arlington, VA 22209

Dr. Don Berlincourt
Channel Products
16722 Park Circle Drive W.
Chagrin Falls, OH 44022

Dr. J. V. Biggers
Pennsylvania State University
Materials Research Laboratory
University Park, PA 16802

Mr. George Boyer
Sensor Systems Program
Office of Naval Research
Code 222
Arlington, VA 22217

Professor R. Bradt
Ceramics Section
Materials Sciences Department
The Pennsylvania State University
University Park, PA 16802

Dr. Dean Buckner
Piezo Products Division
Gulton Industries
P. O. Box 4300
Fullerton, CA 92634

Dr. Robert Callahan
Channel Industries
839 Ward Drive
Box 3680
Santa Barbara, CA 93105

Professor L. E. Cross
The Pennsylvania State University
Materials Research Laboratory
University Park, PA 16802

Mr. N. Coda
Vice President for Engineering
Erie Technological Products
West College Avenue
State College, PA 16802

Dr. Gene Haertling
Motorola Corporation
3434 Vassar, NE
Albuquerque, NM 87107

Dr. W. B. Harrison
Honeywell Ceramics Center
1885 Douglas Drive
Golden Valley, MN 55422

Dr. C. M. Stickley, V. P.
The BDM Corporation
7915 Jones Branch Drive
McLean, VA 22102

Dr. L. L. Hench
Department of Metallurgy
University of Florida
Gainesville, FL 32603

Dr. B. F. Rider
Rockwell International
400 Collins Road NE
Cedar Rapids, IA 52406

Dr. F. Robert Hill
Marine Resources
755 Highway 17 &92
Fern Park, FL 32730

Dr. Bernard Jaffe
232 Forbes Road
Bedford, OH 44146

Dr. B. G. Koepke
Honeywell, Inc.
Corporate Research Center
10701 Lyndale Avenue South
Bloomington, MN 55420

Dr. R. Lapetina
Edo Western Corporation
2645 South 300 West
Salt Lake City, UT 84115

Mr. C. LeBlanc
Naval Underwater Systems Center
TD 121
Newport, RI 02840

Dr. N. Perrone
Code 474
Office of Naval Research
800 N. Quincy Street
Arlington, VA 22217

Dr. Frank Recny
General Electric Company
Court Street
Plant Building C
Box 1122
Syracuse, NY 13201

Dr. J. H. Rosolowski
General Electric Company
Research and Development Center
P. O. Box 8
Schenectady, NY 02301

Dr. P. L. Smith
Naval Research Laboratory
Code 6361
Washington, DC 20375

Dr. R. W. Timme
Naval Research Laboratory
Code 8275
Underwater Sound Reference Division
P. O. Box 8337
Orlando, FL 32806

Dr. Charles C. Walker
Naval Sea Systems Command
National Center #3
2531 Jefferson Davis Highway
Arlington, VA 20390

Dr. Paul D. Wilcox
Sandia Laboratories
Division 2521
Albuquerque, NM 87115

The State University of New York
at Alfred
Material Sciences Division
Alfred, NY

Dr. R. Rice
Naval Research Laboratory
Code 6360
Washington, DC 20375

Professor R. Roy
The Pennsylvania State University
Materials Research Laboratory
University Park, PA 16802

Dr. N. Tallan
AFML Wright-Patterson AFB
Dayton, OH 45433

Dr. H. E. Bennett
Naval Weapons Center
Code 3818
China Lake, CA 93555

Dr. Michael Bell
Inorganic Materials Division
National Bureau of Standards
Washington, DC 20234

Dr. R. Bratton
Westinghouse Research Laboratory
Pittsburgh, PA 15235

Dr. Joe Dougherty, Dir. Engr.
Gulton Industries
212 Durham Avenue
Metuchen, NJ 08840

Dr. James Pappis
Raytheon Co., Research Division
28 Seyon Street
Waltham, MA 02154

Dr. Perry A. Miles
Raytheon Co., Research Division
28 Seyon Street
Waltham, MA 02154

Dr. P. E. D. Morgan
Rockwell Science Center
1049 Camino Dos Rios
P. O. Box 1085
Thousand Oaks, CA 91360

Dr. G. Ewell
MS6-D163
Hughes Aircraft Company
Centinela & Teale Streets
Culver City, CA 90230

Dr. David C. Hill
Member Technical Staff
Texas Instruments, Inc.
Attleboro, MA 02703

Dr. S. K. Kurtz, V. P.
Clairol, Inc.
2 Blachley Road
Stamford, CT 06902

Dr. Herb Moss
RCA Laboratories
Princeton, NJ 08540

Dr. R. E. Newnham
Materials Research Laboratory
The Pennsylvania State University
University Park, PA 16802

Dr. Charles S. Sahagian, Chief
EM Technology Branch, SSS Division
HQ Rome Air Dev. Center (AFSC)
Deputy for Electronic Technology
Hanscom AFB, MA 01731

Dr. J. Smith
GTE Sylvania
100 Endicott Street
Danvers, MA 01923

Dr. Wallace A. Smith
North American Philips Laboratories
345 Scarborough Road
Briarcliff Manor, NY 10510

Mr. Raymond E. Sparks
Technology Library R220
Delco Electronics Division/GMC
P. O. Box 1104
Kokomo, IN 46901

Dr. Manfred Kahn
Senior Scientist, Prod. Dev.
AVX Ceramics, P. O. Box 867
Myrtle Beach, SC 29577

Mr. G. Goodman, Manager
Corporation of Applied Research Group
Globe-Union Inc.
5757 North Green Bay Avenue
Milwaukee, WI 53201

Dr. George W. Taylor
Princeton Resources, Inc.
P. O. Box 211
Princeton, NJ 08540

Mr. John J. Thiermann
Physics International
2700 Merced Street
San Leandro, CA 94577

Dr. D. Carson
Code 7122
Naval Ocean Systems Center
San Diego, CA 92152

Dr. C. Hicks
Code 631
Naval Ocean Systems Center
San Diego, CA 92152

Dr. R. Smith
Code 7122
Naval Ocean Systems Center
San Diego, CA 92152

Professor R. Buchanan
Department of Ceramic Engineering
University of Illinois
Urbana, Illinois 61801

Professor B. A. Auld
Stanford University
W. W. Hansen Laboratories of Physics
Stanford, CA 94306

Dr. S. Musikant
General Electric Co.
3188 Chestnut Street
Philadelphia, PA 19101

Dr. A. Gentile
Hughes Research Laboratories
3011 Malibu Canyon Road
Malibu, CA 90265

Dr. J. Harrington
Hughes Research Laboratories
3011 Malibu Canyon Road
Malibu, CA 90265

Professor G. Kino
Stanford University
Stanford, CA 94305

Dr. A. E. Clark
Naval Surface Weapons Center
White Oak Laboratory
Silver Spring, MD 20910

Dr. Gordon Martin
2627 Burgener
San Diego CA 92110

Eric Udd
McDonnell Douglas Astronautics Co.
5301 Bolsa Ave
Huntington Beach AC 92647